ELEMENTAL FRACTIONATION OF THE SOLAR WIND AS INDICATORS OF CORONAL SOURCE REGIONS AND PHYSICAL PROCESSES

by

Micah Weberg

A dissertation submitted in partial fulfillment
of the requirements for the degree of
Doctor of Philosophy
(Atmospheric, Oceanic and Space Sciences)
in the University of Michigan
2015

Doctoral Committee:

Professor Susan T. Lepri, Co-Chair
Professor Thomas H. Zurbuchen, Co-Chair
Professor Mark Kushner
Research Scientist Enrico Landi

For the two most important women in my life:
my wife, Joanna, and my mother, Carol.

ACKNOWLEDGEMENTS

Whenever one undertakes a task as arduous and audacious as a PhD dissertation, there are, inevitably, a large number of people who deserve recognition and credit for helping bring everything together. The following people have encouraged and supported me in at various points over the last five years. If you are among the ensuing list of individuals, please know that I am exceedingly thankful for your help, wisdom, advice, friendship, and assorted aid (or some other term that best describes our interactions). Due to the vagaries of memory I may have forgotten to mention some important people. If you have been unintentionally omitted, please understand that even though your name has slipped my mind at this time, I am nevertheless thankful for your contribution towards the completion of this thesis.

Firstly, I would like to thank my advisors, Thomas Zurbuchen and Susan Lepri, for their kind mentorship and great patience with me as I have slowly learned the inner workings of academic research. I am grateful to them for giving me the opportunity to come to Michigan and challenging me to grow as a scientist. I would also like to thank the other members of my dissertation committee: Enrico Landi for his quick and insightful feedback and Mark Kushner for his willingness to serve as the cognate member on the committee of a student he had never met in person. I am also quite grateful for my undergraduate advisor, Ramon Lopez, who introduced me to space physics and recommended that Thomas should take me on as a grad student.

Secondly, I am incredibly thankful for the love and support of my family. Most importantly I am deeply indebted to my wife, Joanna, who has supported me, patiently endured the long hours and late nights, and applied her MS Word wizardry to the formatting of this dissertation. I am also thankful for my mother – Carol Weberg – who always encouraged my interest in science, my siblings (Naomi, Anna, Ruth Ellen, & Aaron) for their great life advice, and my adorable nieces and nephews for making visits home fun and full of laughter.

Next I would like to thank my academic family in the AOSS department. In particular the members of the Solar and Heliospheric Research Group (SHRG) for their stellar insight and all of my officemates past and present (Liang Zhao, Dan Gershman, Jacob Gruesbeck, Gina DiBraccio, Aleida Higginson, Mark Stakhiv, Patrick Tracy, Gang Kai Poh, Robert Alexander, & Manan Kochler) for their friendship, hours of advice, scientific debates, and many entertaining digressions on a bountiful array of topics. I would also like to acknowledge the collaboration and academic commiseration of my old classmates; foremost amongst them are Willow Wan, Justin Perket, and Blake Johnson who have made my years in the department, both in class and without, more fun. Also within my extended scientific family are Kalman Kniznik, whom I consider an honorary officemate and SHRG member, and Joel Dalhlin, a fellow heliophysics student and friend I first met at SHINE in 2011. I look forward counting them as colleagues in our coming scientific careers.

Penultimately, I am very grateful for the friendship and blessings provided by my community at New Life Church. They have kept me sane and spiritually grounded throughout the ups and downs of grad school and made my time in Michigan a joyous adventure. While there is not space enough to name everyone, I would like to specifically thank the men of my discipleship group in its various iterations (namely Chris McCurry, Micah Seppanen, Adam Dumas, Dan Jahncke, Mike Cha, Rodney Noel, Keegan Behm, Ryan Hulett, Luke March, Nathan Donker, and recently Sam Ferber). They have been mighty lights in my life and dear friends who have continuously pushed me to “be a man” and grow in Christ-like character (Donker et al. 2015, private communication).

Lastly and most importantly, I would like to express my eternal gratitude for the wisdom, inspiration, and providence of God – without him none of this would be possible.

This work was supported, in part, by grants from the *ACE* mission (44A-1085637), the Living with a Star program (NNX10AQ61G), NASA contract NNX08AM64G, and a NASA Earth and Space Science Fellowship (NESSF). Additional funding for travel and summer conferences was provided by the Solar Heliospheric and INterplanetary Environment (SHINE) conference which is, in turn, sponsored by the National Science Foundation (NSF).

TABLE OF CONTENTS

LIST OF FIGURES

Figure

LIST OF TABLES

Table

LIST OF ACRONYMS

ACE	Advanced Composition Explorer
AU	Astronomical Unit
AWSoM	Alfven Wave Solar Model
CR	Carrington Rotation
CS	Current Sheet
DOY	Day of Year
DSCOVR	Deep Space Climate Observatory
EIT	Extreme ultraviolet Imaging Telescope
ESA	Electrostatic Analyzer
ESA	European Space Agency
EUV	Extreme Ultraviolet
FIP	First Ionization Potential
HCS	Heliospheric Current Sheet
ICME	Interplanetary Coronal Mass Ejection
IMF	Interplanetary Magnetic Field
LASCO	Large Ange and Spectrometric Coronagraph
MAD	Median Absolution Deviation
MDI	Michelson Doppler Imager
NASA	National Aeronautics and Space Administration
PA	Pitch Angle
SB	Sector Boundary
SEM	Standard Error of the Means
SEP	Solar Energetic Particles
SI	Stream Interface
SIR	Stream Interaction Region
SOHO	Solar and Heliospheric Observatory
STD	Standard Deviation
SWEPAM	Solar Wind Electron, Proton, and Alpha Monitor
SWICS	Solar Wind Ion Composition Spectrometer
SWMF	Space Weather Modeling Framework

SWOOPS	Solar Wind Observations Over the Poles of the Sun
SWPC	Space Weather Prediction Center
UTC	coordinated universal time
UVCS	Ultraviolet Coronagraph Spectrometer
VHM	Vector Helium Magnetometer

ABSTRACT

Heavy ions in the solar wind record the history of physical events occurring to a given parcel of plasma during its escape from the solar atmosphere. Heating, acceleration, and interactions with waves, particles, and magnetic fields all imprint their signatures in the elemental composition and ionic charge states of heavy ions which carry the information unchanged from a few solar radii all the way to the edge of the heliosphere. Therefore by studying heavy ions in the solar wind near-Earth, we are able to peer back into the corona and gain valuable insight concerning physical processes within a region currently inaccessible to direct satellite exploration.

Understanding how mass and energy is released from the Sun and transported into interplanetary space is of increasing importance to our modern society which depends on space-based technology for global navigation and communications. In this work we explore the source regions, release and acceleration mechanisms, and elemental fractionation of the slow solar wind. In particular we seek to answer the following questions: (1) “How much plasma, if any, do the largest coronal loops contribute to the solar wind?”, (2) “Where and how does closed filed plasma escape into the solar wind and become accelerated?”, and (3) “What are the physical conditions and time scales required for gravitational settling?”. Towards these ends, we delve into over 20 years of solar wind data from two nearly identical Solar Wind Ion Composition Spectrometer (SWICS) instruments which flew onboard the Ulysses (1990 – 2009) and Advanced Composition Explorer (ACE; 1998 - present) spacecraft. We utilize novel analysis methods and discover the existence of a new class of solar wind events which we call “heavy ion dropouts”. These dropouts have distinctive, mass-fractionated elemental composition indicative of specific coronal conditions and probable source regions. By analyzing the temporal and spatial variability of heavy ion dropouts and comparing our observations to basic

simulations of the solar corona, we are able to provide fresh insight which may be used to constrain, validate, and refine prevailing solar wind theories.

CHAPTER I

INTRODUCTION AND SCIENTIFIC BACKGROUND

The Sun has been a topic of great cultural and religious interest dating back to antiquity. It is then no surprise that some of the earliest astronomical discoveries were related to the Sun. For example, the oldest recorded solar eclipse dates back to 1223 BC (de Jong & van Soldt 1989) and it is known that by the eighth century BC Babylonian astronomers were keeping detailed records of eclipses. Later the invention of the telescope in 1608 AD allowed researchers such as Thomas Harriot and Galileo Galilei to study *sunspots*, dark regions on the surface of the Sun with intense magnetic fields and suppressed temperatures. However it was not until the 1960's and the advent of satellite based observations that the modern of subject of *Heliophysics* – the study of the Sun, the solar wind, and its influence on the region of space around it – was truly born.

A considerable body of research has been written in the last five decades; nevertheless, great mysteries still remain. Some of the puzzles include: "How does the Sun generate magnetic fields?", "What heats the solar atmosphere to more than 200 times hotter than the solar surface?", "What is the structure of the heliosphere?", and - perhaps most importantly - "how does solar variability impact humanity?" Within this present work we endeavor to answer, at least in part, the long standing question of "What is the source of the slow solar wind?" by investigating clues embedded in the heavy ion composition of the solar wind and comparing their abundance variations to physical processes in the corona. As a consequence, we establish new connections between in-situ measurements and potential source regions which, while aiding the development & testing of theories, ultimately contributes towards our understanding of how particles escape the Sun and influence near-Earth space. In this chapter we attempt to condense and summarize the most important discoveries relevant to our efforts.

Longer and more detailed summaries of space plasma physics and the history of ideas concerning the solar wind may be found in books by Gombosi (1998) and Meyer-Vernet (2007).

1.1 HELIOPHYSICS, SPACE WEATHER, AND THEIR SOCIETAL IMPACTS

Solar and heliophysics research is not a purely scientific endeavor. As the primary source of energy in the solar system, the Sun drives Earth's climate and shapes the space environment in which astronauts and satellites operate. Despite centuries of scientific observation, we do not yet understand the full extent of how variations in solar energy and mass output can affect the Earth and its heliospheric vicinity. Understanding how the Sun influences near-Earth space is of vital importance to our global society as it becomes increasingly dependent on space-based technology for financial transfers, telecommunications, and navigation.

Extreme conditions in the solar wind can have significant, sometimes severe, impacts on Earth orbiting satellites and astronauts. Streams of high speed or high density solar wind can compress the Earth's magnetic field, intensify electric currents in the upper atmosphere, and trigger what are called *geomagnetic storms* (Gonzalez et al. 1994). These storms, while heralded by especially bright and beautiful auroras, pose a hazard to people and infrastructure both in space and on the ground. Common effects include: (1) disruption of telecommunications and GPS navigation, (2) increased radiation over the poles which necessitates rerouting transpolar airline flights, (3) temporary or permanent incapacitation of satellites due to high energy particles and spacecraft charging, and even (4) damage to ground-based power grids (Carlowicz and Lopez 2002). These effects, along with their drivers, are the subject matter of *space weather*. A report published by the National Research Council estimates that a large geomagnetic storm, like the infamous 1859 "Carrington event" in which auroras were visible as far south as Cuba (Green et al. 2006), could cause over $1 trillion in damage – both direct and collateral (National Research Council 2009). Large eruptions on the Sun called *Coronal Mass Ejections* (CMEs) cause the biggest and most dangerous storms; however geomagnetic storms can also be triggered by shocks that regularly occur during normal solar wind conditions. Other transient solar events such as *solar flares* can also pose a

hazard to astronauts and satellites by accelerating electrons to almost the speed of light. These "killer electrons" can cause irreparable damage to both electronic and biological systems.

Active monitoring and accurate predictions of solar wind conditions will become invaluable in the future as humanity develops new satellite technologies and begins to send manned missions out into the solar system. Key components needed for predicating and then mitigating the effects of geomagnetic storms are knowing where on the Sun solar wind originates from, the density and velocity of a given solar wind stream, and what direction the interplanetary magnetic field will be when the stream reaches Earth. This thesis will address the first two points by attempting to identify source regions, release mechanisms, and acceleration processes of the solar wind – in particular slow type solar wind. By studying the origin and propagation of the solar wind, we construct a more detailed picture of how energy and mass are transferred from the Sun to near-Earth space.

1.2 Basic Properties and Structure of the Sun

The Sun is a G-type main sequence star approximately in the middle of its lifespan. By mass density the Sun is composed of 73.81% hydrogen (H), 24.85% helium (He), and the remaining 1.34% of other "heavy" elements (Asplund et al. 2009). A list of basic solar properties and constants is given in Table 1.1. Everything we know about the solar interior comes from models and helioseismology (Gough 1985; Boothroyd & Sackmann 2003). Despite the lack of

Table 1.1: Basic Solar Properties

Property	Standard Value	Units	Reference
Approximate age	4.57	Gy	Bonanno et al. 2002
Mass (M_S)	1.9884×10^{30}	kg	IAU constant (Luzum et al. 2011)
Radius (R_S)	6.9634×10^{8}	m	Emilio et al. 2012
Mean density	1.41×10^{3}	kg m^{-3}	Derived
Surface gravity (g)	274.234	m s^{-2}	Derived
Core temperature	~1.5×10^{7}	K	Clayton 1986
Effective surface temperature	5771.8	K	Derived
Range of coronal temperatures	1 - 20	MK	Ko et al. 1997; Aschwanden et al. 2015
Mean magnetic field on the surface	1.89 (min) 3.81 (max)	G	Vidotto et al. 2014
Astronomical Unit (AU) (mean Sun-Earth distance)	1.496×10^{11}	m	Pitjeva & Standish 2009
Total Solar Irradiance (at 1 AU)	1360.8	W m^{-2}	Kopp & Lean 2011

direct measurements, we are fairly certain of some facts. The central core (< 0.25 R_S) of the Sun has an extremely high density and temperature (> 15 MK) and contains roughly half of the total mass. It is here that a series of thermonuclear reactions take place which fuse H into He. During this process 0.726% of the mass involved is converted into energy that sustains the fusion reaction and is, eventually, emitted as light (Collins 1989). Only a small portion of the total energy produced in the Sun is actually emitted as visible light. Outside the core there are the *radiative* (0.25 – 0.71 R_S) and *convection* (0.71 – 1.0 R_S) zones which are named after the dominant form of heat transfer within the given region. It is believed that sub-surface flows within the convection zone generate the Sun's large scale magnetic field (Charbonneau 2014).

The solar magnetic field flips polarity approximately every 11 years. This process is called the "solar cycle" and is accompanied by periodic variations in the total number of sunspots. At solar minimum there are considerably fewer sunspots than at solar maximum and they are located closer to the solar equator. During solar maximum, the occurrence rate of CMEs is 10 times greater than at solar minimum. Similarly, solar flares are 50 times more common at solar maximum (McIntosh et al. 2015). The total solar irradiance (TSI) received by Earth increases by ~0.1% at solar maximum (Kopp & Lean 2011). While small, this change in energy output has measurable effects on terrestrial climate and corresponds to a ~0.1^{o} C increase in global temperatures.

The temperature and density of solar plasmas decrease steadily from the core to the surface. The visible surface of the Sun is called the *photosphere* and it has an average temperature of 5771.8 K and density of ~10^{23} particles per m^3. Above the photosphere lies the *chromosphere,* a ~2100 km thick layer in which the temperature increases to about 10,000 K and many important spectral lines originate (hence the layer is named after the Greek word "chroma" which means "color"). Next is the very thin *transition region* where the temperature sharply jumps by a factor of over 100, from ~10,000 K to a few MK (1 x 10^6 K or more). Very little is known about the transition region and the exact nature of the heating mechanism, although theories abound (Hammer 1982; Parker 1988; Priest et al. 2000). The sharp rise in temperature is demonstrated in Figure 1.1 which shows an example profile of temperature and density above the solar surface. The last and thickest layer of the solar atmosphere is the

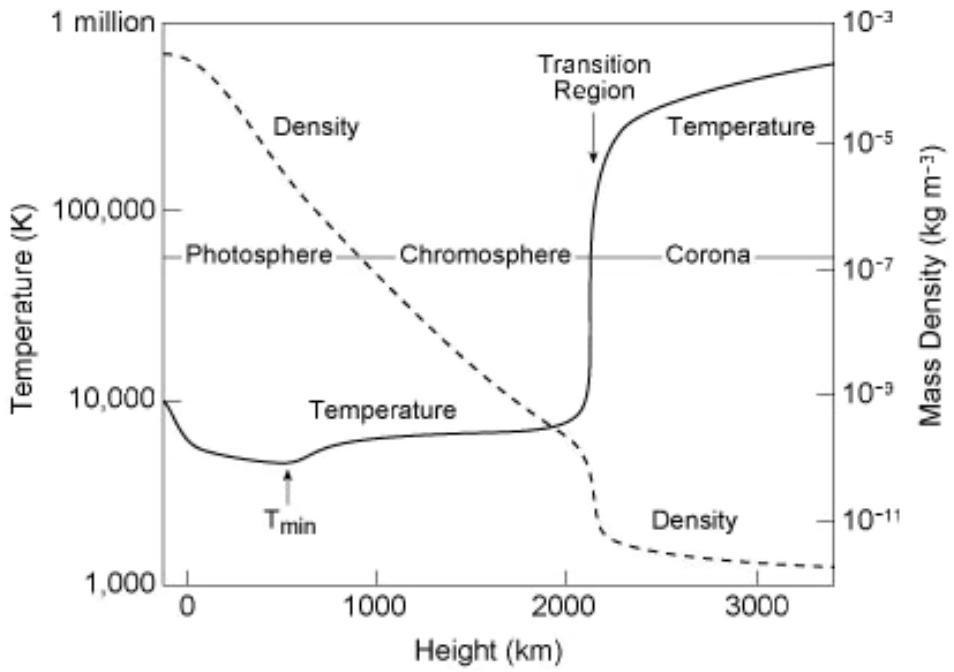

Figure 1.1: Temperature (log scale; left y-axis) and mass density (right y-axis) of plasma in the solar atmosphere. Distances are approximate and span from slightly below 1 R_S to 1.005 R_S from the center of the Sun. Adapted from Lang (2006). The Temperature decreases in the photosphere (0 – 500 km) from ~5772 K to a minimum of ~4200 K. It then rises in the chromosphere (500 – 2100 km) to nearly 10,000 K and then jumps inside the narrow transition region to the coronal value of 1 MK. Adapted from Lang (2006).

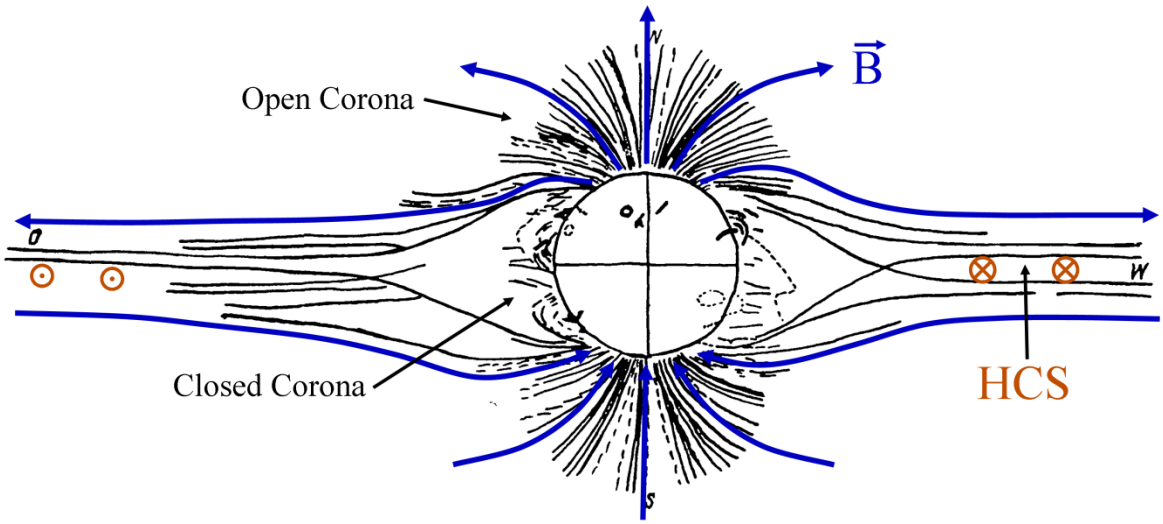

Figure 1.2: Structure of the corona at solar minimum drawn from photographs obtained during a solar eclipse. Open magnetic field lines emanate from the polar coronal holes while a band of closed magnetic loops straddles the equator. Arrows have been added showing the magnetic polarity (blue) and location of the heliospheric current sheet (red). Modified from Vsekhsvjatsky (1963).

corona which extends from the top of the transition region out to a few solar radii. The corona can be divided into open magnetic field regions called *coronal holes* where the field lines extend out to the edge of the heliosphere, and closed field regions comprised of magnetic loops of varying sizes (typically with a maximum height of less than 300 Mm). Figure 1.2 illustrates the two coronal regions. Particularly large coronal loops are also called *coronal streamers* and are often located below the *heliospheric current sheet* (HCS) which separates sectors of opposite magnetic polarity. As we shall show in the following sections, the corona is home to a number of interesting physical processes which heat, accelerate, and release solar plasmas into space where it becomes known as the *solar wind*.

1.3 The Solar Wind and Space Weather

1.3.1 Brief History of the Solar Wind

The solar wind is a stream of plasma that flows radially out from the Sun at all times. Its existence was first postulated at end of the 19th century when scientists noticed curious correlations between features on the Sun and perturbations in the Earth's magnetic field and brightening of the auroras (for example: Carrington 1859 and Birkeland 1905). The idea was strongly opposed at the time and the concept fell into obscurity until Ludwig Biermann (1951) conclusively proved that the solar wind *must* exist because comets had two distinct tails, one from solar radiation and a second from interaction with charged particles streaming away from the Sun. A number of theories quickly followed which tried to predict the characteristics of the solar wind. Sydney Chapman (1957) favored the idea of a stationary solar corona extending far into space. On the other end of the spectrum, Eugene Parker (1958) predicted that the solar wind was not only mobile but was accelerated to supersonic speed. All that remained was to observe the in-situ solar wind and determine who was right. Both the Russian Luna satellites in 1959 (Gringauz et al. 1960) as well as the US Explorer 10 mission in 1961 (Bonetti et al. 1963) all measured solar wind plasmas, however their results were inconclusive. Finally in 1962 Mariner 2 provided compelling and unambiguous observations in agreement with Parker's supersonic solar wind theory (Neugebauer & Snyder 1962). Thus began the modern era of heliophysics and solar wind research.

1.3.2 Heavy Ion Measurements

The solar wind is composed primarily of H^+ (~95-98%) and He^{++} (~2-5%) ions with a number of free electrons such that the solar wind, as a whole, has zero net charge (that is to say, $n_{e^-} = n_{H^+} + 2 * n_{He^{++}}$). The bulk dynamics of the solar wind therefore is almost entirely dominated by the density and velocity of H^+. Continuous observations of the bulk solar wind parameter have been made since 1963 beginning with the *Interplanetary Monitoring Platform* (*IMP*) series of spacecraft (Bridge et al. 1965) and continuing today with the *Advanced Composition Explorer* (*ACE*; Stone et al. 1998) and Deep Space Climate Observatory (*DSCOVR*; Szabo et al. 2010). The bulk solar wind plasma, however, retains very little evidence concerning its origin and acceleration in the corona.

The study of heavy ions (elements heavier than He; also called "metals" by astronomers) in the solar wind has been an active research topic since the first observations of O^{5+}, O^{6+}, & O^{7+} by the twin Vela 3 satellites in 1965 (Bame et al. 1968). Heavy ions comprise less than 1% of the total mass in the solar wind. Nevertheless, the large range of masses and charge states exhibited by heavy ions provide a wealth of information unattainable from studies of H^+ and He^{++} in the bulk solar wind plasma. The relative elemental abundances and charge states of heavy ions are determined by physical conditions – temperature, electron density, wave interactions etc. – within the lower corona (Owocki et al. 1983) and propagate relatively unchanged from a distance of a few solar radii all the way out to the edge of the heliosphere (Hundhausen 1972). The location at which the charge state ratios become set is called the *freeze-in point*. The freeze in point marks the height at which collisional ionization and recombination with free electrons is almost non-existent due to low electron densities. Due to differences in ionization and recombination rates, each element and ion will become "frozen in" at a different height in the corona (Geiss et al. 1995b; Landi et al. 2012). Therefore the history and profile of solar wind acceleration and heating is directly imprinted in the compositional signatures of heavy ions. By studying heavy ions in the solar wind near Earth, we are able to peer back into the corona and gain valuable insight concerning the physical processes within.

1.4 CLASSIFICATION AND SOURCES OF THE SOLAR WIND

1.4.1 The Canonical Two Types of Solar Wind

One of the most striking features of the solar wind is large variations in the bulk velocity. This is most clearly seen around solar minimum when there are a number of high-speed streams that come and go at regular intervals over many solar rotations. Figure 1.3 shows one such time period observed by *ACE* during day of year (DOY) 121 – 151 of 2007 (i.e. May 2007). The subplots are, from top to bottom: (a) bulk solar wind speed (V_{sw}), (b) H^+ number density, (c) magnitude and (d) ecliptic plane angle, λ, of the magnetic field (where 0^o points radially away from the Sun and positive angles proceed counterclockwise in the same direction as Earth's orbit), (e) the total density and pitch angle (the angle of a given particle's velocity relative to the magnetic field) of 272 eV suprathermal electrons, (f) the O^{7+}/O^{6+} charge state ratio, and finally (g) the iron to oxygen elemental ratio (Fe/O). Suprathermal electrons (energies > 70 eV) always flow away from the Sun along local magnetic field lines. Therefore their pitch angles indicate whether a field line is pointed away from (for parallel streaming around 0^o PA) or towards (antiparallel around 180^o) the Sun. Taken together, (c), (d), and (e) tell us about the absolute direction and connectivity of the magnetic field and can also indicate when the spacecraft crosses a current sheet (signified by a flip in both λ and e^- streaming accompanied by a spike in $|\mathbf{B}|$). The O^{7+}/O^{6+} ratio (f) is used as a proxy for the electron temperature in the source region of the given parcel of plasma. As we can see in Figure 1.3, there is a repeating pattern of high-speed, low density streams followed by slower, denser streams.

Sounding rocket observations in 1973 suggested that high-speed solar wind streams originate from the open field regions of coronal holes (Krieger 1973). This hypothesis has been confirmed (Nolte et al. 1976; Bame et al. 1993) and it is now generally accepted as fact. The source of the slow wind streams, on the other hand, is still a topic of considerable debate. Initially researchers believed that slow wind streams also originated from coronal holes and that the speed difference was the result of highly diverging magnetic field lines (for example, see Pneuman 1976). Heavy ion measurements, in particular those from *Ulysses*, challenged this idea. Geiss et al. (1995a) provided compelling evidence that fast and slow speed streams had very different ionic and elemental composition. In particular they noted that slow wind streams

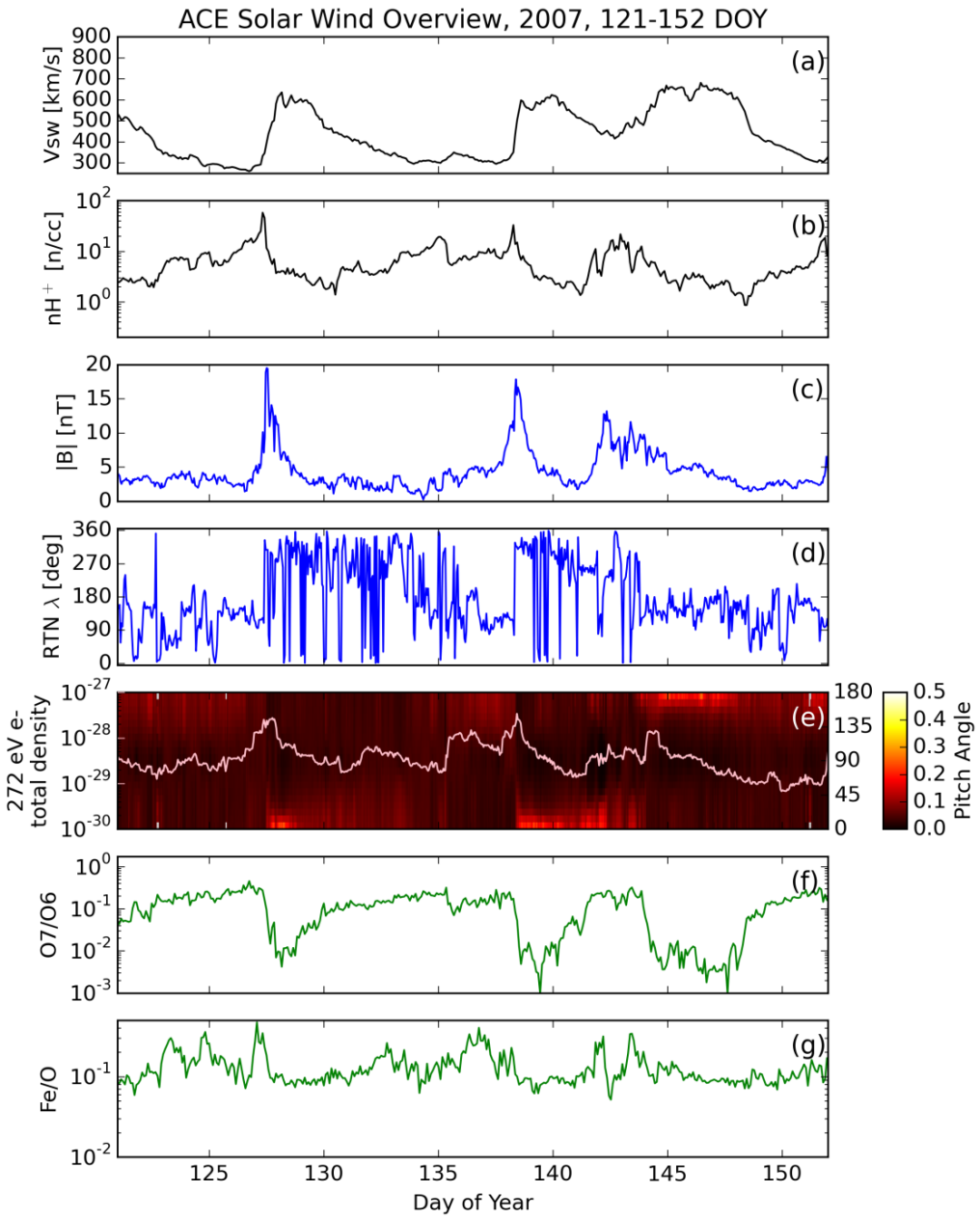

Figure 1.3: Overview of solar wind parameters as observed by *ACE* between 121 – 152 DOY (May) of 2007. The subplots are, from top to bottom: (a) bulk solar wind speed (V_{SW}), (b) H^+ number density (nH^+), (c) magnitude and (d) ecliptic plane angle, λ, of the magnetic field, (e) the total density and pitch angle (direction of streaming relative to the magnetic field) of 272 eV suprathermal electrons, (f) the O^{7+}/O^{6+} charge state ratio, and finally (g) the Fe/O ratio. (a), (b), (f), & (g) are from the *ACE* / SWICS instrument (Gloeckler et al. 1998), (c) & (d) are from the MAG instrument (Smith et al. 1998), and finally panel (f) contains data from the SWEPAM-E sensor (McComas et al. 1998).

came from hotter source regions, as evidenced by higher O^{7+}/O^{6+} ratios, which had enhancements of the recently discovered "First Ionization Potential effect" as indicated by high Mg/O (note: we explain the FIP effect in more detail in section 1.3.2 below). An example of these variations can be clearly seen in Figure 1.4 where the high-speed streams are clearly anticorrelated with O^{7+}/O^{6+} (which is a proxy for T_e in the source region of the corona) and Fe/O (which has similar trends as the Mg/O used by Geiss et al.). Another key consideration came when analyzing the latitudinal distribution of solar wind. Figure 1.5 is a pair of polar plots showing the solar wind velocity during the first two *Ulysses* orbits. At solar minimum (left hand side of Figure 1.5) fast (~700 km/s) and steady wind dominates the polar regions while slow (300 – 500 km/s) and highly variable wind is confined to a band ~30° wide around the solar equator. These correspond well to the open-field coronal holes and the closed-field coronal streamer regions as illustrated by the background solar images. At solar maximum (right hand side of Figure 1.5) the picture is much more complicated with both slow and fast speed wind

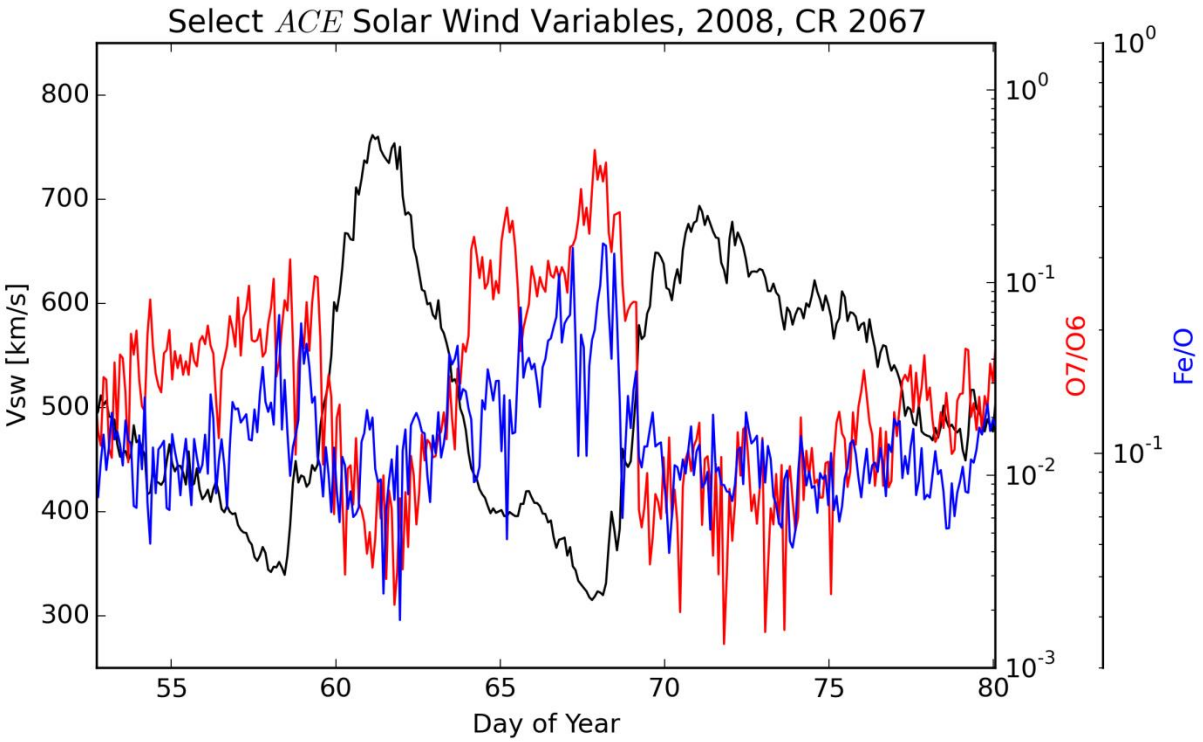

Figure 1.4: Select solar wind variables observed by *ACE* during Carrington Rotation 2067 (2008 DOY 52.7327 – 80.0557). The bulk solar wind velocity is sharply anticorrelated with coronal source region temperature (represented by O^{7+}/O^{6+}) and the Fe/O elemental ratio (indicating a strong FIP bias; see section 1.41 for more details).

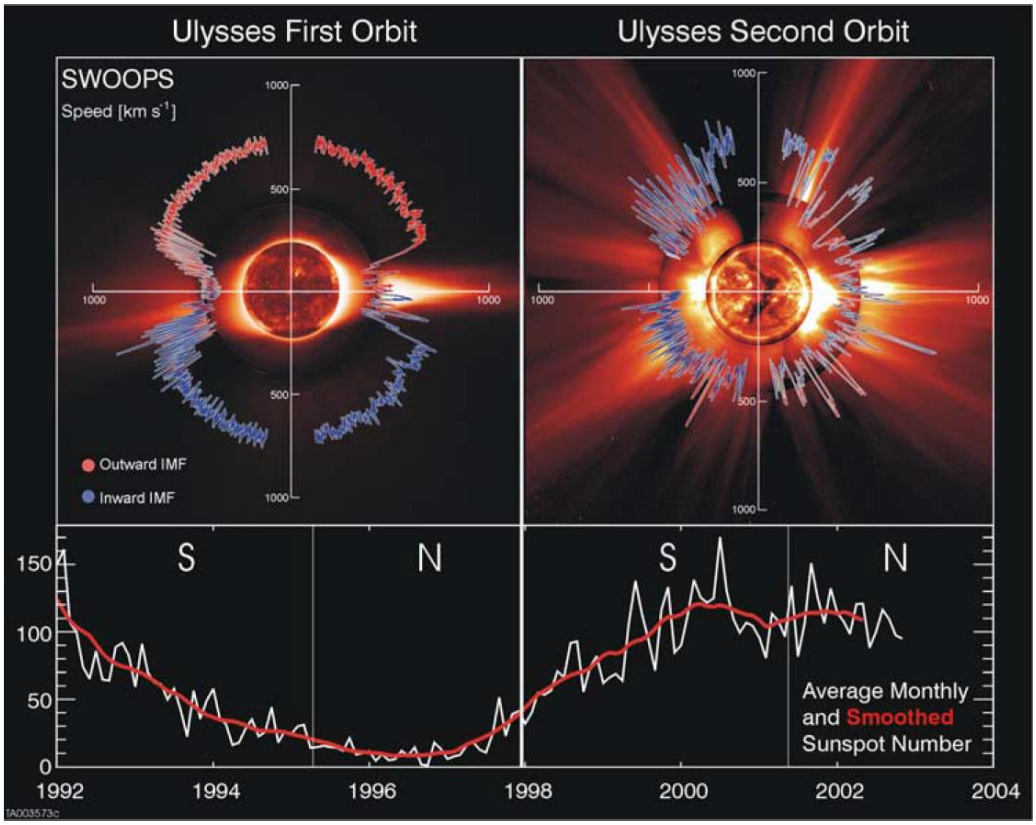

Figure 1.5: Polar plots of bulk solar wind speed observed by *Ulysses* during its first (1992 – 1997) and second (1998 – 2003) orbits. In both sides, time begins on the left (negative X-axis) and proceeds counterclockwise. Behind the plots are representative solar images from 8-17-1996 (left) and 12-7-2000 (right). The images are composites of SOHO EIT at 195 Å, the Mauna Loa K-coronameter, and SOHO LASCO. The average sunspot number is plotted along the bottom. Adapted from McComas et al. (2003).

observed interspersed at nearly all latitudes consistently with a much more complex configuration of the solar corona than at solar minimum.

From the observations it became quickly clear that slow-speed streams of solar wind were distinctly different from high-speed streams. Since the early attempts to separate the two types of solar wind were based on speed, the classifications of “fast” and “slow” were adopted. These names have stuck despite the efforts of each new theory to suggest their own nomenclature. Zhao et al. (2009) suggested the theory-neutral labels of “coronal hole wind” and “non-coronal hole wind”. However these titles have yet to be fully adopted by the heliophysics community. In an effort in minimize confusion, we shall defer to the older naming convention. Table 1.2 summarizes some of the primary dissimilarities between fast and slow wind. Beyond the velocity and density differences, the most significant disparity between fast

Table 1.2: Fast vs Slow Solar Wind Properties

	Speed [km s^{-1}]	Density [# cm^{-3}]	Variability of Parameters	Temperature of Source Region	Composition	Origin
Fast	≥ 500	2.5 – 5	Fairly constant	≤ 1 MK	Photospheric	Coronal Holes
Slow	< 500	7 - 10	Highly variable	1 – 3 MK	Coronal	Heavily debated

and slow wind is their elemental composition. Fast solar wind has photospheric abundances, as would be expected of plasma which left the solar surface and expanded relatively unchanged into interplanetary space. In contrast, slow wind has abundances similar to remote observations of closed coronal loops (von Steiger et al. 2000) where a veritable host of physical processes have the opportunity to alter the elemental fractionation of magnetically trapped plasmas.

1.4.2 The First Ionization Potential Effect

When researchers first began to make abundance measurements of the solar wind and the corona – the latter inferred from solar energetic particle (SEP) abundances and later confirmed by spectroscopy – they noticed an unusual fractionation when compared to the corresponding photospheric values (Pottasch 1963; Hovestadt 1974; Meyer 1981). The element to oxygen ratios (X/O) of elements with low first ionization potential (FIP < 10 eV) were observed to be enhanced in the corona and slow wind relative to the photosphere. Furthermore, the high FIP elements of Ne and He, which have FIPs of 21.56 eV and 24.59 eV respectively, were observed to be depleted relative to the photosphere. This ordering by FIP – the amount of energy required to remove the first electron from a neutrally charged atom – came to be called the "FIP effect". Figure 1.6 is a colorized version of Figure 9 from von Steiger et al. (1997). The X-axis shows elements ordered by FIP and the Y-axis gives the element to oxygen (X/O) abundance ratios normalized by the corresponding photospheric values. In the Figure we can clearly see that the low FIP elements of Mg, Fe, & Si have X/O ratios enhanced by factors of 3 – 5 in the slow solar wind (red markers labeled "Solar Wind (Interstream"). Similar enhancements are also seen in the SEP abundances (green error bars). By comparison, the fast solar wind (blue lines) exhibits relatively small enhancements. The most significant deviations from this trend are Xe and Kr. However noble elements are notoriously difficult to measure

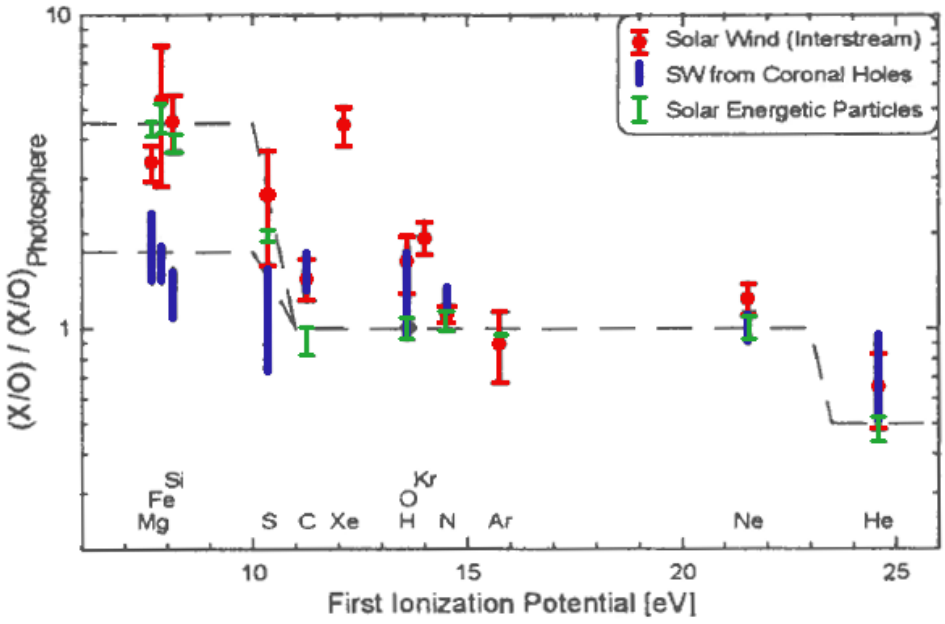

Figure 1.6: X/O ratios in the solar wind normalized by their photospheric counterparts and ordered by FIP. Elements with low FIP (< 10 eV) have X/O ratios enhanced by factors of 3 – 5 in the slow solar wind (red). Weaker enhancements can be seen in the fast wind (blue). The high FIP element of He is depleted relative to the photosphere. Modified from von Steiger et al. (1997).

in-situ and their nonconformity may be due to instrumental uncertainties. Later studies by von Steiger et al. (2000) found slightly lower FIP enhancements of around 2 – 3 in the slow solar wind. For comparison, Feldman (1992) determined that the upper corona had an average FIP enhancement of ~4 during quiet conditions.

The FIP effect was, and continues to be, one of the most puzzling features of the corona and solar wind. An array of different mechanisms have been proposed including simple separation of ions and neutrals during ionization (Vauclair & Meyer 1985), trapping of highly ionized plasmas in the corona (von Steiger & Geiss 1989), interaction with waves in the chromosphere or lower corona (Tagger et al. 1995; Laming 2012). Additionally, there has been some debate as to whether the abundances of high-FIP elements, including O, are actually depleted (Veck & Parkinson 1981; Meyer 1991) in the FIP effect instead of the low-FIP elements being enriched (Sylwester et al. 1984; Lemen et al. 1986). Many absolute abundance measurements seem to support the enhancement interpretation (Sterling et al. 1993) however there are other studies which appear to support the depletion of high-FIP elements and

emphasizes the importance of systematic variations in the total oxygen abundance (Schmelz et al. 2012). Whatever the cause, FIP fractionation is nearly ubiquitous in the solar wind, slow wind in particular, and any attempts to explain the origin of the solar wind must take this into account.

1.4.3 Slow Solar Wind Origin Theories

Both the compositional and latitudinal evidence point to a connection between slow solar wind and either the open field boundary or the closed corona itself. Many theories have been put forth to explain this correlation. We shall quickly summarize here the four prevailing ideas.

(1) "The Expansion Factor model" (Wang & Sheeley 1991; Cranmer et al. 2007) claims that slow wind originates from open field regions near the boundary of coronal holes. In this theory flux tubes containing slow wind expand more rapidly with height than in the fast wind which results in a decrease of the final velocity. This is a very simple theory which is in many ways a revamped version of the early diverging field lines idea. Most modern expansion factor models assert that the solar wind is accelerated by pressure gradients caused by waves in the corona. Different heating profiles and assorted plasma waves are invoked to explain the charge state signatures of slow wind; however none of the models can account for the elemental abundance differences between fast and slow wind. Since, in this scheme, *all* solar wind originates in open field regions and quickly escapes into the heliosphere, there is no time for the “slow” wind to become fractionated relative to the photosphere. Nevertheless, work on this theory continues and some recent observational and modeling efforts seem to imply that the expansion factor model could be used to identify subtypes within the fast wind (Stakhiv et al. 2015; Oran et al. 2015).

(2) The “Interchange Reconnection model” (Fisk et al. 1998; Fisk 2003) suggests that solar wind comes from closed coronal loops which reconnect with adjacent open field lines. This process, called “interchange reconnection”, results in one leg of the previously closed loop becoming connected to an open magnetic field line and releasing the otherwise trapped plasma into the heliosphere. This reconnection process is illustrated in Figure 1.7. The boxes on the left

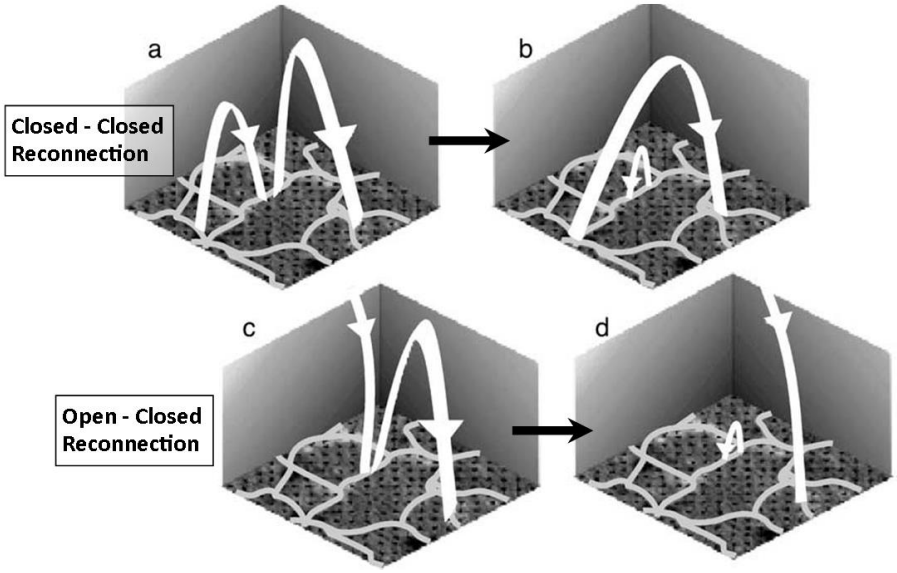

Figure 1.7: Illustration of interchange reconnection between two closed coronal loops (a → b) and an open field line and a closed loop (c → d). The latter scenario results in the release of plasma from one leg of the previously closed loop. In both cases the foot points of the fields are assumed to be rooted in the lanes between convective cells on the solar surface (light grey lines). Reconnection occurs when- and wherever surface flows move oppositely directed magnetic field lines into close proximity. Adapted from Fisk (2003).

show the initial states of two different scenarios: interchange reconnection between (a) two closed loops and (c) a closed loop and an open field line. After reconnection (right boxes) the field lines have swapped foot points and formed a small secondary loop and either (b) one large loop or (d) an open magnetic field line along which plasma from the previously closed loop may escape. In both situations the smaller loop is free to either grow in size until it reconnects again or subduct back into the photosphere. The interchange reconnection model is highly dynamic and predicts nearly continuous reconnection. The ensuing release of coronal plasma at the open-closed field boundary would be able to explain both the elemental composition and latitudinal variability of the slow solar wind. However it requires a large amount of open flux diffusing into closed field regions which has been challenged by some researchers (Antiochos et al. 2007).

(3) The "Streamer Top model" (Suess et al. 1996; Endeve et al. 2004) posits that the boundaries of coronal streamers are inherently unstable and continuously dynamic. As a consequence, closed flux tubes at the boundary expand outward and become open through reconnection (including interchange type) or "evaporation" in which heating cause the inflation

opening of field lines (Suess et al. 1999). In one version of the streamer top model suggested by Wang et al. (2000), the slow solar wind is divided into two components: a narrow band of wind, dubbed "slow II", confined within ~3^{o} of the HCS which is in turn enveloped by a wider (~15^{o}) region of "slow I" wind flowing from open field lines rooted in coronal holes. Note, the slow I wind is nearly identical to that predicted by the expansion factor model. The slow II component is identified as the result of either interchange reconnection in the underlying coronal streamer or a pinching off of the streamer top. The latter process has been observed remotely (Sheeley et al. 1997) and is the source of what are colloquially called "LASCO blobs". In many respects, the streamer top model is a combination of the first two theories. The only significantly new idea is the inclusion of plasmiods from the tops of streamers. Additionally, despite its efforts to combine theories, this model has difficulty explaining the ~30^{o} angular width of FIP-fractionated slow wind observed during solar minimum (as seen in Figure 1.5).

(4) The final scheme we will describe is the "S-Web model" (Antiochos et al. 2007; 2011) which is a close cousin to the interchange reconnection model and uses rigorous topology constrains for its conclusions. According to the conjectures of this theory, low latitude coronal holes are connected to polar coronal holes via extremely thin open field "corridors". These corridors form a network of "quasi-separatrix layers" (discontinuities in the magnetic field) around the HCS where magnetic reconnection with closed field regions freely occurs. The subsequent escape of coronal loop plasma then forms the slow solar wind. The S-Web model is thus able to account for both the composition and angular width of the slow wind without the need for large scale diffusion of magnetic flux. However the open field corridors on which the theory rests are also its biggest weakness. The sizes predicted for these corridors are smaller than the resolution of even the best solar imaging. This makes it nearly impossible to confirm or deny the model using observational data.

Determining the source of the slow solar wind has been a fundamental mystery in heliophysics for the greater part of the past four decades. None of the theories so far have been conclusively proven, either true or false, with strong observational evidence. One of the limiting factors is the challenge of identifying the source regions of in-situ plasmas. Such a mapping, if performed with sufficient resolution and accuracy, would clearly validate or reject

most model predictions. However tracking the solar wind back it its solar origins is very difficult. Close to the Sun, the solar magnetic field has significant non-radial components which can transport plasma from higher latitudes down to the ecliptic plane and vice versa. Additionally, interactions between solar wind streams in interplanetary space can change the velocity of a given parcel of plasma and further complicate back-tracking efforts.

1.5 Dissertation Objectives and Motivating Science

1.5.1 Focus of this Study

Heavy ion composition provides an alternative method of locating the source of the solar wind. As previously discussed in section 1.2.3, the ionic and elemental composition of the solar wind contains information about the physical conditions and processes within the corona. Therefore any solar wind with unusual or atypical composition must, by logical extension, originate from a source region that either has properties distinctly different from the rest of the corona or is subject to particular processes not found in other regions. The observation of unusually fractionated plasma in the solar wind thereby places specific requirements on the physics occurring in the corona, which narrows down the list of possible source regions and also imposes hard constraints on slow wind theories.

The primary objective of this dissertation is to use solar wind composition to constrain, validate, and refine the prevailing solar wind theories and provide a fresh set of observations and events that must be accounted for in current or future models. Towards these ends we compare unusually fractionated solar wind with remote observations of the corona and attempt to build strong connections between the two and identify specific source regions of slow solar wind. Any theory which is unable to explain the existence and inevitable release of solar wind from the structures and source regions ascertained by our study cannot be a singular or definitive explanation and must in some way be amended or combined with other theories.

In this study we classify and categorize a new type of solar wind plasma events which we call “heavy ion dropouts”. These dropouts have distinctive, mass-fractionated elemental composition similar to unique fractionation patterns that have been observed remotely but, prior to our study, had never been observed in-situ. In our study of heavy ion dropouts we are

able to determine their approximate source regions and learn something new about the balance between elemental fractionation processes that produce the end composition of the solar wind.

1.5.2 Gravitational Settling

Remote observations of coronal streamers in the late 1990's noticed distinctive abundance patterns which point to a fractionation process in direct competition with the FIP effect. Raymond et al. (1997a) analyzed the ultraviolet spectral lines of 13 elements inside a large coronal streamer. They found severe depletions of all elements inside the core of the streamer relative to photospheric values. They attributed this depletion to a process called "gravitational settling" in which heavier elements are preferentially held back by gravity due to their shorter scale heights. The result is a mass stratified solar atmosphere in which the densities of the heavier elements fall off faster with height than the lighter elements. A study by Feldman et al. (1999) also found evidence for gravitational setting. Figure 1.8 is a reproduction of one of their key plots showing the line intensities of various spectral lines (Y-

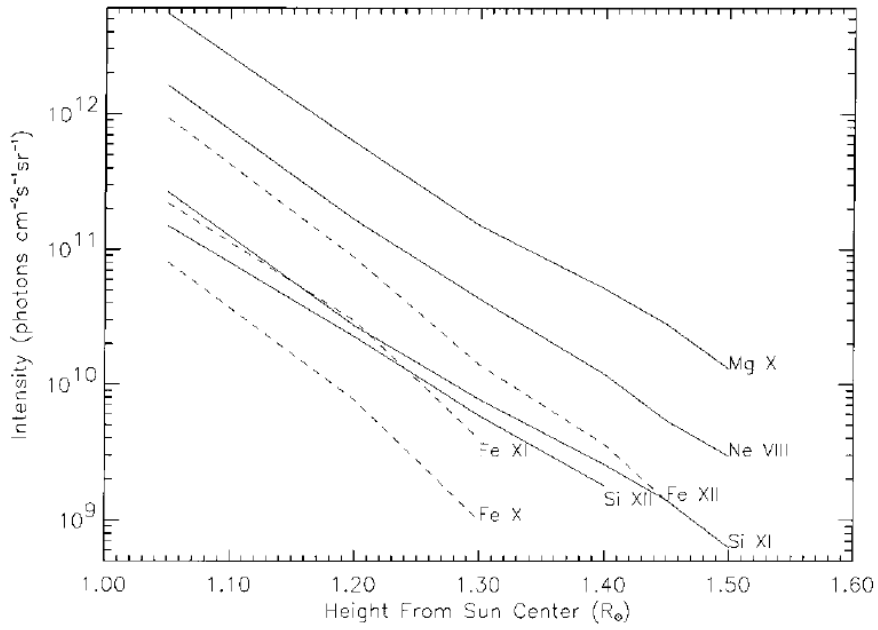

Figure 1.8: Intensities of representative spectral lines as a function of radial distance above the west limb of an equatorial streamer. Adapted from Feldman et al. (1999).

axis) as a function of height (X-axis) within an equatorial streamer. Feldman et al. noted that the line intensities of Fe (dashed lines) decreased faster with height than the intensities of the lighter elements of Ne, Mg, and Si (solid lines). Since the particular streamer they observed was well represented by an isothermal temperature profile (with T = 1.3 MK), the decrease in intensity was assumed to be directly proportional to depletions in elemental abundances. As noted above, this sort of behavior is the signature predicted by gravitational settling.

The observation of gravitationally settled plasmas in the corona was a somewhat surprising result for some researchers. In order to acquire noticeable settling, a given coronal structure would have to remain closed and relatively undisturbed by waves, heating, or flows on time scale of more than a day. In a follow-on paper to their initial observations, Raymond et al. (1997b) calculated that a streamer would require a settling time on the order ~83 hours. After the time period of a few days, the predicted abundances became more depleted than those observed which would then require a small amount of mixing to maintain agreement with the remote measurements. However, Schwadron et al. (1999) calculated that flow velocities as slow as 10 – 100 m s^{-1} along the streamer loop would be sufficient to erase the mass-dependent fractionation of gravitational settling. An alternative explanation provided by Noci et al. (1997) suggested that the apparent depletion of elements could be the result of an enhancement in neutral hydrogen. However this would require continual outflows from the streamer core region which would contradict the observations of Strachan et al. (2002). Nevertheless, despite these predictions, elementally depleted streamers continued to be observed (Marocchi et al. 2001; Uzzo et al. 2003, 2004) and modelers were moderately successful in reproducing the same qualitative behavior (Ofman 2000). Furthermore, the heavy ion abundances observed within these coronal streamers are distinctly different from the typical solar wind, making them prime candidate sources in our initial search for unusually fractionated wind.

1.6 GUIDING SCIENCE QUESTIONS

While we now have a wealth of information concerning plasmas in the corona as well as detailed, in-situ measurements of the solar wind, considerable work remains to unify the two

disparate observational regimes. Researchers are now developing more holistic models that span from the solar surface to the outer heliosphere but these models not yet include the full range of compositional signatures observed. Our primary objective addresses the fundamental question of "what is the source of the slow solar wind?" This general question is further reduced to three specific science questions that consider the origin, release and acceleration mechanisms, and elemental fractionation of the slow solar wind.

1.6.1 How much plasma, if any, do the largest coronal loops contribute to the solar wind?

Coronal streamers consist of the largest magnetic loops in the corona and, since they straddle two regions of opposite polarity, are found below the heliospheric current sheet. Streamers are by nature steady on the time scale of multiple solar rotations and, according to the interchange reconnection and streamer top models, contribute plasma to the slow solar wind via reconnection near the streamer legs and plasmoids ejected from the cusp. While much research has gone into studying the plasma coming from typical streamers (Suess et al. 2009; Wang et al. 2012 and references therein), it remained to be seen whether the quietest loops, such as those observed by Raymond et al. (1997a) and Feldman et al. (1999), also contributed plasma to the solar wind and if so, how much. This is a critical test of the interchange reconnection model since there is no physical reason why large loops would not contribute plasma while smaller loops did.

1.6.2 Where and how does closed field plasma escape into the solar wind and become accelerated?

With the exception of the expansion factor model, all of the solar wind models predict that plasma trapped on closed magnetic field lines is being released into the solar wind. However the location, rates, and mechanisms invoked are different and sometimes directly contradictory. The spatial and temporal variability of heavy ions should allow us to determine their approximate source latitudes, locations, and probable release mechanisms. The results may then be used differentiate between the solar wind theories. Furthermore, the current models have posited two different acceleration processes for the solar wind – pressure

gradients driven by waves in the lower corona and direct energization during interchange reconnection. The identification of solar wind escaping from high up in a closed, coronal streamer strongly indicates acceleration via interchange reconnection since the plasma will have originated from above the height at which most wave acceleration is thought to occur.

1.6.3 What are the physical conditions and time scales required for gravitational settling?

As demonstrated by Schwadron et al. (1999), gravitational settling requires a very narrow range of conditions in order to occur. Any turbulent mixing, large scale flow, or wave heating within a coronal loop will prevent or erase mass-fractionation. Nevertheless, gravitationally settled plasmas *have* been observed remotely and our heavy ion dropouts are evidence that some of that plasma escapes into the solar wind (we will explore and demonstrate this fact over the following chapters). The particular compositional signatures, both elemental abundances and ionic ratios, of our dropout events should yield evidence concerning the physical properties of their source regions. This task is complicated by the FIP effect which competes with gravitational settling and may occur in tandem. Additionally, we will need to demonstrate not only that gravitational settling is able to occur in certain coronal loops but also determine why *all* coronal loops do not exhibit mass-fractionation.

1.7 OBSERVATION METHODS

Our primary tool for addressing these questions will be in-situ measurements of heavy ions. Where applicable, we will also make comparisons to remote observations to aid us in interpretation and independently test our key results. In this section we provide a general overview of the various observational methods used in solar physics today.

1.7.1 Remote Observations

The oldest method of studying the Sun is via optical measurements. Figure 1.9 is a composite image showing examples some of the different types of modern remote observations. The data are from the Solar and Heliospheric Observatory (*SOHO*) and were taken between 19:00 – 20:48 coordinated universal time (UTC) on May 4th, 2007. “White light”

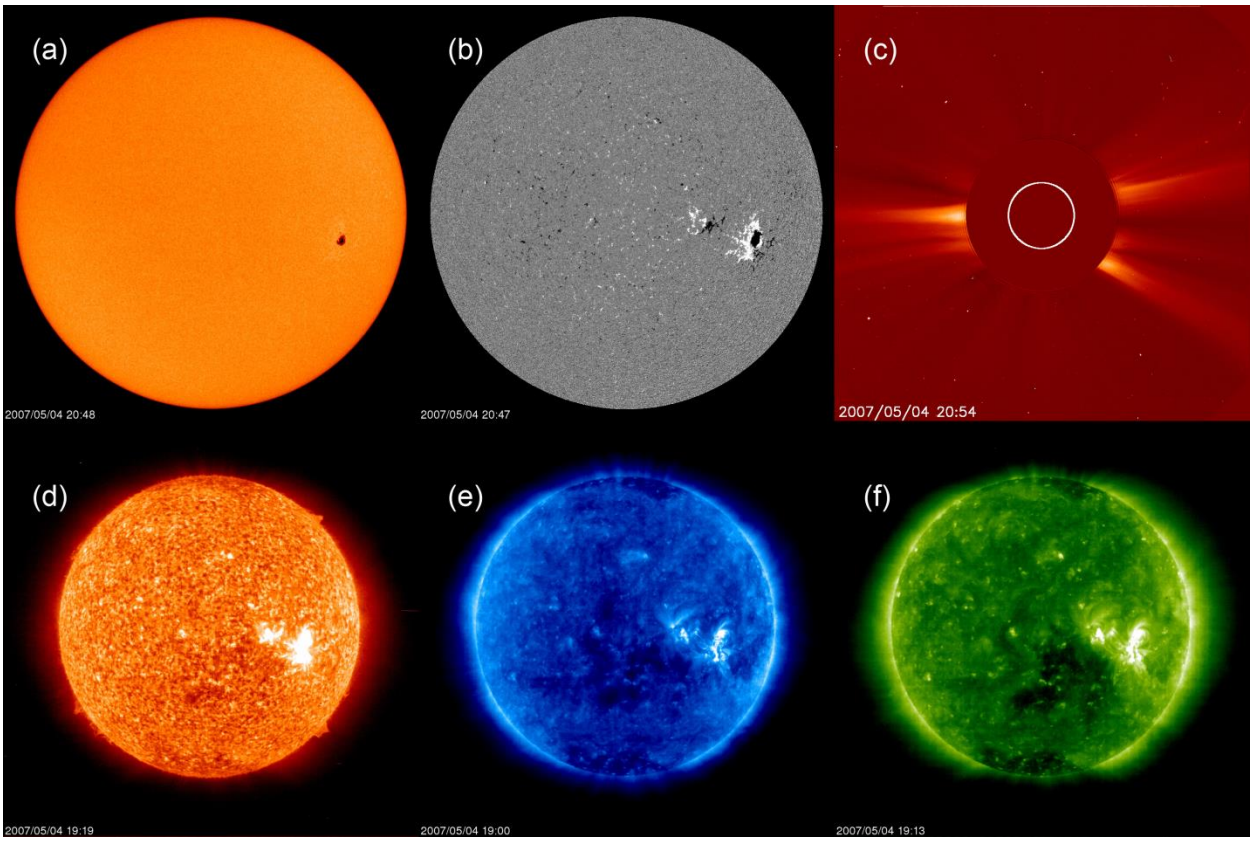

Figure 1.9: A collage of remote solar imaging from the *SOHO* satellite. (a) MDI continuum image taken around 6767.8 Å (676.78 nm) which can be used to identify sunspots. (b) Magnetograph showing inward (black) and outward (white) directed magnetic fields. (c) Coronagraph image which can be used to study coronal structures on the limb of the Sun. (d), (e), and (f) EUV images taken at 304, 171, and 195 Å which correspond, respectively, to temperatures of (d) 50,000 K, 1 MK, and 1.25 MK. (a) and (b) are from the Michelson Doppler Imager (MDI; Scherrer et al. 1995), (c) comes from the Large Angle and Spectrometric Coronagraph (LASCO; Brueckner et al. 1995), and finally (d) – (f) were taken by the Extreme ultraviolet Imaging Telescope (EIT; Delaboudinière et al. 1995).

imaging (a) in the visible part of the spectrum can be used to identify sunspots. Additionally, when polarization and the Zeeman effect (the process in which spectral lines split into multiple components in the presence of a magnetic field) are taken into account, white light imaging is capable of mapping the longitudinal component of magnetic fields on the solar surface. This is shown in subplot (b) of Figure 1.9 where black and white patches indicate, respectively, inward and outward directed magnetic fields. During a total solar eclipse the Moon covers up the disk of the sun and it is possible to see the corona which, although much hotter than the solar surface, is considerably fainter in absolute brightness in the visible range. Coronagraph imagers are special telescopes which have opaque disks that create an artificial eclipse for continuous

observations of the corona. Coronal streamers appear in coronagraph images as bright, spindly features such as those seen in Figure 1.9 (c). Spectral lines in the extreme ultraviolet (EUV), (d) – (f), are produced at certain characteristic temperatures. Within a given image, bright (dark) regions denote plasma that is hotter (cooler) than the characteristic temperature. The images in Figure 1.9 correspond to temperatures of (d) 50,000 K, (e) 1 MK, and (f) 1.25 MK. Multiple EUV images can be studied in parallel to identify specific coronal structures and obtain an approximate temperature profile as different temperature plasmas exist at different heights. The final type of remote observation we shall mention here is single-slit spectroscopy. By measuring the line intensities of specific elemental emission and absorption lines and comparing them to catalogs of atomic spectra such as the CHIANTI database (Dere et al. 1997; Landi et al. 2013), spectroscopic methods (see Phillips et al. 2008) can be used to determine the physical properties of the emitting plasmas.

Remote observations yield tremendous information about plasmas near the Sun; however they are not without limitations. The most advanced methods require considerable processing to produce the final image. These calculations often include certain assumptions – such as electron density profiles, ionization rates, or thermal equilibrium – which may not hold true for all situations and introduce small shifts and observational biases to the data. Scattered light, Doppler shifts, and line broadening must also be taken into account. Additionally some techniques, particularly observations of the solar limb, are challenged by line-of-sight issues which make it difficult to isolate a given feature from the light originating in front of or behind the area of interest. All of these difficulties can, of course, be adjusted for, yet no amount of careful planning can overcome the most fundamental limitation of remote observations: they are confined to a few solar radii, at most, and thus tell us little about the fate of the solar wind once it leaves the Sun and expands into interplanetary space.

1.7.2 In-situ Measurements

The other primary means of studying the Sun is by sampling the particles and plasmas it ejects. In-situ measurements of the interplanetary magnetic field (IMF), bulk solar wind (H^+ and He^{++}) velocity, density, and energetic particles are relatively straightforward to obtain and

provide information concerning the dynamics of the solar wind as it expands into the heliosphere and interacts with planetary bodies. Since the advent of rockets and the exploration of space using satellites, in-situ measurements have been obtained at a variety of distances from the Sun (from as close as 0.29 AU to the very edge of the heliosphere), high heliographic latitudes, and in orbit around the 6 out of the 8 planets in the solar system (with flybys and orbits of many smaller bodies such asteroids, comets, and dwarf planets).The biggest limitation of in-situ measurements is the single point nature of the observations which makes it difficult to separate spatial and temporal effects. This can be partially mitigated by flying multiple satellites in formation; however this greatly increases the cost and complicates the orbital dynamic calculations needed. Furthermore the number of spacecraft available for scientific research is severely limited by funding and many missions never make it past the planning stages. Additionally, while remote observations cannot tell where a parcel of plasma is going, in-situ measurements have difficulty identifying where on the Sun a given stream of plasma originated. The elemental composition of the solar wind can help bridge the gap between the two paradigms.

1.7.3 The SWICS instrument

In our study we make extensive use of heavy ion measurements from the Solar Wind Ion Composition Spectrometer (SWICS) instrument which flew on both the *Ulysses* and *Advanced Composition Explorer (ACE)* satellites (Gloeckler et al. 1992; 1998). SWICS is a time-of-flight mass spectrometer capable of measuring the densities, velocities, and thermal velocities of over 40 charge states between the elements of He, C, N, O, Ne, Mg, Si, S, and Fe. The energy range of SWICS runs from 0.11 keV/q to about 100 keV/q. A schematic of the SWICS measurement technique is shown in Figure 1.10. The electrostatic analyzer (ESA) is a pair of curved metal plates. An electric potential is established across the ESA which bends the trajectory of incoming particles. At a given potential, only ions with a specific energy per charge (E/q) will make it through the entire ESA. Therefore by stepping the ESA through different potentials, the instrument can filter for ions with different E/q. Next an ion is accelerated by 23 keV and passes through a thin carbon foil which kicks off a few secondary electrons that trigger

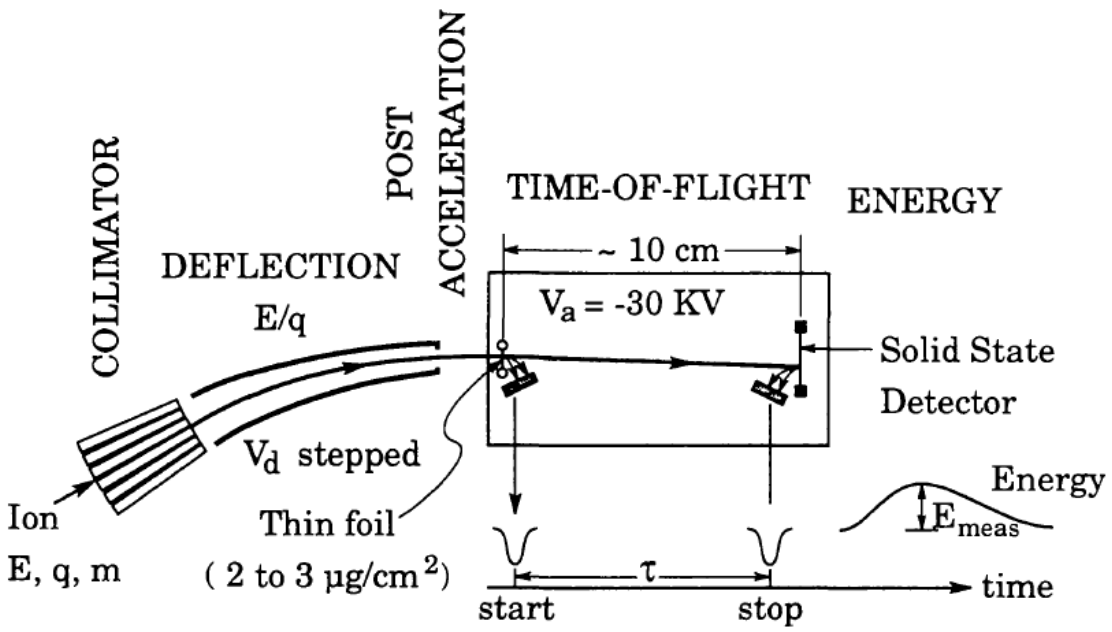

Figure 1.10: Schematic illustrating the SWICS measurement method. Adapted from Gloeckler et al. (1992)

a start timer. The ion then traverses the time-of-flight section and hits a solid state detector which measures the particle's total energy. This also sets off a cascade of secondary electrons which finally trigger a stop signal. At this point SWICS has measured an ion's E/q, total energy, and velocity (time it takes to cross a known distance). With these quantities in hand it is then possible to derive the mass, velocity, and charge state of each incident particle.

The two spacecraft SWICS flew on are important and unique for different reasons. *Ulysses* was a joint ESA / NASA mission launched in October 1990 that had a highly elliptical (1 – 5 AU), polar orbit (80.2^o inclination) around the Sun. It provided the first, and so far only, measurements made from outside the ecliptic plane. Ulysses completed three full orbits, twice at solar minimum and once at solar maximum, before ceasing operations in 2009. *ACE* was launched in February of 1998 and currently resides near the First Lagrangian (L1) point; the location where the gravity of Earth and the Sun partially cancel each other and result in a heliocentric orbit with the same period as Earth. *ACE* serves as an upstream solar wind monitor and provides early warning of conditions potentially hazardous to astronauts and satellites near Earth. To these ends, *ACE* carries a complete suite of plasma instruments optimized for a range

of masses and energies and also makes high resolution magnetic field measurements. Taken together the SWICS observations of *Ulysses* and *ACE* span nearly 24 years and cover a large range of heliospheric latitudes and distances.

1.8 CHAPTER OVERVIEWS

In chapter II of this dissertation, we describe the first in-situ observations of heavy ion dropouts using *ACE* / SWICS data. Many of these dropouts exhibit mass fractionation similar to the gravitationally settled streamers of Raymond et al (1997a) and Feldman et al. (1999). We further analyze the temporal and spatial distribution of dropout events in Chapter III and perform some basic calculations to determine their approximate source latitudes. Chapter IV describes supporting work we performed to validate and independently confirm our *ACE* observations with in-situ data from *Ulysses* and remote images from *SOHO*. We then attempt to build a theoretical framework for interpreting heavy ion dropout observations in Chapter V with the goal of identifying the physical process responsible for mass fractionation in the corona and solar wind. Finally, in chapter VI we summarize our findings, revisit the guiding science questions, and comment on possible future work.

CHAPTER II

ACE/SWICS OBSERVATIONS OF HEAVY ION DROPOUTS WITHIN THE SOLAR WIND

The text in this chapter was published in: Weberg, M. J., Zurbuchen, T. H., & Lepri, S. T. (2012), *The Astrophys. J.*, **760**, 30. The abstract and introductory sections have been combined and edited for inclusion in this dissertation.

2.1 INTRODUCTION

We present the first in situ observations of heavy ion dropouts within the slow solar wind, identified for select elements ranging from helium to iron. For iron, these dropouts manifest themselves as depletions of the Fe/H ratio by factors up to ∼25. The events often exhibit mass-dependent fractionation and are contained in slow, unsteady wind found within a few days from known stream interfaces. We propose that such dropouts are evidence of gravitational settling within large coronal loops, which later undergo interchange reconnection and become source regions of slow, unsteady wind.

Spectroscopic studies by Raymond et al. in 1997 (and later Feldman et al. in 1999) yielded strong evidence for gravitational settling within large coronal loops in the equatorial streamer belt region. Due to the often large geometric size of these coronal structures, one might expect that the gravitationally settled plasma should be observed in situ if the large, closed loops reconnect with the open field corona as has been theorized (see Antiochos 2011; Fisk 2003). However, the expected in situ signature of plasma with heavy elements fractionated by mass had not been observed prior to this study.

The primary question we wish to address here is: *if gravitational settling has been remotely observed in closed coronal loops and these loops are undergoing magnetic reconnection and releasing their plasma into the solar wind, do we observe mass-fractionated*

plasma in situ? Obviously, the preponderance of FIP-fractionated plasmas in the slow wind, observed in the average over many years (von Steiger & Zurbuchen 2011), suggests that mass-fractionation processes cannot dominate the end solar wind abundances very often, else we would have already observed such plasmas using long-term averages and our above question would be superfluous. Thus, it is assumed then that any mass-fractionated plasma that might exist within our data sets must be moderately short and hidden so as not to have been readily apparent. We must therefore first determine an appropriate indicator to aid us in searching for such events.

Based on its large mass and the expected fractionation patterns, it is clear that Fe is a very good indicator of gravitational settling, especially when contrasted with FIP fractionation. It is known that in FIP-fractionated plasmas Fe/O increases by factors of 2–4 (von Steiger et al. 2000). Conversely, in gravitationally settled plasmas we should see a substantial decrease of Fe, even when compared to lighter elements that may be depleted themselves. That is, Fe/O would be expected to decrease when compared to either slow or fast wind abundances and, additionally, should have the greatest relative depletion of all the elements.

2.2 METHODOLOGY

2.2.1 Data Description

We used 2 hr averaged data from the Solar Wind Ion Composition Spectrometer (SWICS) on board the *ACE* satellite (Gloeckler et al. 1998). SWICS is a highly capable mass spectrometer with a time-of-flight telescope that has also flown on the *Ulysses* and *Wind* spacecraft (Gloeckler et al. 1992). SWICS is capable of measuring the speeds and densities of almost 40 different ions across the elements of H, He, C, N, O, Ne, Mg, Si, S, and Fe. The accuracy of these measurements is generally within 20% or better, with some exceptions due to the limitations of counting statistics or the finite resolution of mass and charge which can lead to overlapping peaks of certain detected ions (see Appendix of von Steiger & Zurbuchen 2010). For these reasons, N and Ne are not as well resolved as the other elements. In an effort to be as complete as possible while still maintaining proper quality and rigor, we have chosen to retain N within our analysis but will largely ignore Ne. Our analysis compares the heavy

elements relative to H, taking advantage of an extensive effort to cross-calibrate the H and He measurements of the two plasma sensors on ACE: SWICS and SWEPAM (McComas et al. 1998). The cross-calibrated data are also available from ACE level 3 data at http:// www.srl.caltech.edu/ACE/.

2.2.2 Selection Criteria

We began by surveying the ratios of each SWICS-measured heavy element relative to hydrogen and searching for periods of time where the heavier elements, Fe in particular, seemed to drop significantly compared to the density variations of the rest of the solar wind. Specifically, we took the $\log_{10}$ of the Fe/H ratio and computed its average and standard deviation within a given Carrington rotation (CR), the 27.2753 day period corresponding to one rotation of the Sun about its axis. We then identified all periods of time where the Fe/H ratio dropped below one standard deviation from the CR average. We then required an event to have the following characteristics in order for us to consider it a possible heavy ion "dropout":

1. Duration 4 hr. This is mainly a result of the 2 hr time resolution of our data set. While this limitation on length certainly prevents us from observing shorter events, which may still be relevant to our study, it should also filter out any possible short, unrelated transient events while leaving the longer, more interesting events intact. As we will discuss later in Section 4, most of the dropout events we have found are on the order of 15 hr long or more and are thereby unaffected by the 4 hr duration criterion. Furthermore, using the 2 hr SWICS data allows for longer accumulation times which yields better differentiation between elemental species and insures that the data within our dropouts are of sufficient quality to run meaningful statistics.
2. One or more particularly low data points at least two standard deviations below the CR average. This criterion is, to a certain extent, arbitrary. However, we empirically determined that this was the simplest and most consistent test for picking out the cleaner, more significant events outside the normal variability of Fe/H.

2.2.3 Event Filtering

Using the method described above, we obtained a list of 315 possible dropout events within the time period of 2001–2009. This initial list was first filtered by rejecting 14 cases which had significant (>33%) data gaps and then further refined by disregarding 15 events where the X/H ratios changed primarily due to a rise in the hydrogen density while the elemental densities remained the same. We made this last determination by comparing the correlation coefficients between variations in n_H & Fe/H and n_{Fe} & Fe/H. Those events where the drop in Fe/H is due to a rise in hydrogen density will have a negative Fe/H to n_H correlation coefficient of greater magnitude than the corresponding Fe/H to n_{Fe} coefficient. Such "dropouts" do not represent actual depletions of heavy ions and are not the focus of our current analysis.

Additionally, special care was taken to exclude from calculations and consideration any data that occur within interplanetary coronal mass ejections (ICMEs). ICMEs are transient events with their own set of compositional characteristics (Zurbuchen & Richardson 2006) and we currently have no reason to associate them with processes such as gravitational settling which require a less chaotic environment. Richardson & Cane (2010) have produced a fairly exhaustive list of ICMEs in the near-Earth environment using, in part, data from ACE. For our purposes, we simply exclude the time periods of the Richardson and Cane ICMEs from our calculations and ignore the 29 dropouts that begin or end within an ICME. Such periods may be an interesting topic for a future study.

Of the initial list of 315 candidate dropout events, 257 remained after filtering. These remaining dropouts all exhibit moderate-to-significant depletions of the heavy elements and we will constrain our subsequent statistics and discussion to only these events. First, in Section 2.3, we show an example of a particularly good dropout as a means to explain and illuminate our analysis method and primary conclusions. Then, in Section 2.4, we present statistics on fractionation patterns, occurrence rates, and average elemental abundances. Finally, we summarize our key observations and conclusions in Section 2.5.

2.3 EXAMPLE DROPOUT

2.3.1 Plasma Overview

Figure 2.1 shows an overview of solar wind conditions in a ∼10 day period of time centered on a dropout found in 2003. The plots are, from top to bottom, solar wind speed (V_{SW}), density (n_H), magnetic field magnitude $|\mathbf{B}|$, RTN longitude λ, O^{7+}/O^{6+} ratio (a good proxy for oxygen freeze-in temperature (Geiss et al 1995b)), and the two elemental ratios O/H and Fe/H. There is a strong depletion in Fe that occurs for ∼16 hr from 340.93 to 341.59 DOY (December 6th 22:13 to December 7th 14:17). Inside this period Fe/H drops more than an order of magnitude, from an average of 9.37×10^{-5} to 7.82×10^{-6} (a total factor of ∼12). A weaker depletion is also seen in the O/H ratio (9.53×10^{-4} to 1.34×10^{-4} or a factor of 7.1).

It has been established that one can differentiate between fast and slow solar wind using some combination of charge state ratios (Zhao et al. 2009; von Steiger et al. 2010). Using the O^{7+}/O^{6+} criteria of Zhao et al. (as shown by the solid horizontal line in Figure 2.1) we note that the dropout is embedded in slow solar wind between two fast wind streams. Due to the differences in average velocity, fast wind streams often overtake slow wind streams and form stream interaction regions (SIRs). The boundary between the two streams within an SIR is called a stream interface (SI). Typical plasma characteristics of a slow-to-fast wind SI include smoothly increasing solar wind velocity, a local maximum in tangential pressure, and a compression in both proton number density and magnitude of the interplanetary magnetic field (Jian et al. 2006). SIs, when mapped back to solar wind source regions on the Sun, lie near the separator of topologically open and closed magnetic fields in the corona (Wimmer-Schweingruber 1999). For the purposes of this study, we use a list of identified near-Earth SIRs, with SIs, produced by Jian et al. (2011) and available online at http://www.ssc.igpp.ucla.edu/∼jlan/ACE/Level3/SIR_List_from_Lan_Jian.pdf. Our example dropout in Figure 2.1 comes right before a slow-to-fast SI listed in the above Jian survey and visible in Figure 2.1 by the sharp jump in solar wind density at 341.59 DOY. Therefore, we deduce that our dropout originated from a closed, coronal loop similar to those that are thought to be the sources of the slow solar wind. We also note that a magnetic sector boundary is visible in Figure 1 on day 339 as an abrupt transition in λ. Such a transition normally indicates a crossing of the heliospheric current sheet (HCS).

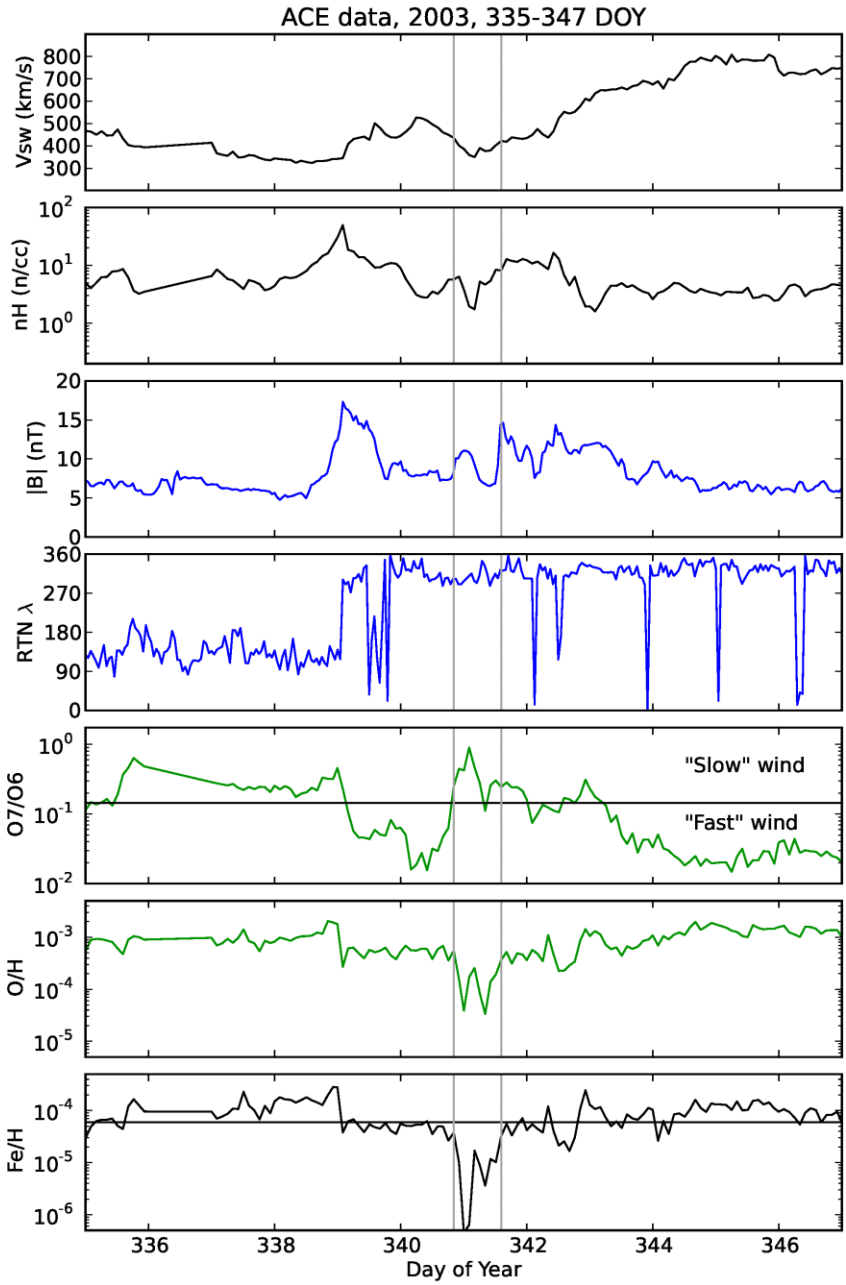

Figure 2.1: *ACE*/SWICS plasma overview for 335–347 DOY, 2003. The plots are, from top to bottom, solar wind speed, number density, magnetic field magnitude, RTN longitude, O^{7+}/O^{6+} ratio, and the two elemental ratios O/H and Fe/H. The solid horizontal line in the Fe/H subplot shows the average ratio value within CR 2010 which contains the days plotted here. Also, the solid horizontal line in the O^{7+}/O^{6+} subplot indicates the Zhao et al. (2009) solar wind type criteria of O^{7+}/O^{6+} = 0.145. A heavy ion dropout was observed from 340.93 to 341.59 DOY where Fe/H dropped by an order of magnitude. Two stream interfaces and their corresponding maxima of the magnetic field are visible at 339.2 and 341.59. The transition in λ on 339 DOY indicates a heliospheric current sheet crossing. All plasma data are taken from the SWICS database and the magnetic field data are from the MAG instrument.

2.3.2 *Elemental Fractionation*

We now define a "reduction factor" for each element by taking the average X/H ratios 5 days before and after the dropout and dividing them by their corresponding averages within the dropout period. These reduction factors represent the depletions of each element relative to their abundances in the immediately neighboring plasma. Elements with larger reduction factors are therefore more depleted relative to H than those with smaller factors. If another dropout occurred within the same ±5 day window, it was omitted from the calculations of the averages since we desired to only compare to the unperturbed, background solar wind abundances. The ±5 day window allows for enough statistical significance in our analysis and exceeds the typical correlation timescales of compositional data (Zurbuchen et al. 1999, 2000). However, our analysis does not strongly depend on the actual duration of this interval. Figure 2.2 is a plot of the reduction factors computed for all SWICS-measured elements over the same

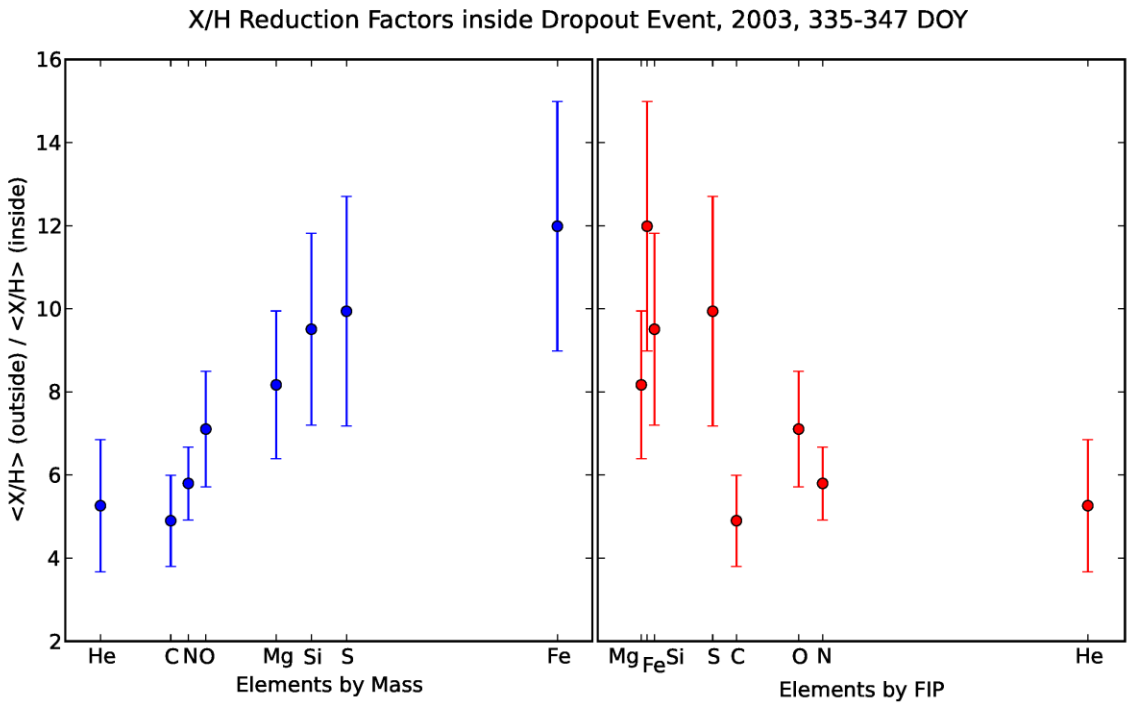

Figure 2.2: X/H reduction factors inside the 335–347 DOY, 2003 dropout event shown in Figure 2.1. Reduction factors are computed by taking the average ratio 5 days before and after the dropout and dividing them by the ratios inside. Error bars were determined using the standard error of the means. Elements with larger reduction factors are more significantly depleted. The rising trend in reduction factors is in qualitative agreement with gravitational settling.

time period as shown in Figure 2.1. The statistical uncertainty was determined using standard error propagation and from the standard error of the means (SEM) inside and outside the dropout. The left-hand side of the plot orders the elements by mass while the right-hand side orders them by ionization potential, FIP. We also include N data, despite the inherent measurement challenges previously mentioned. The inclusion of this less certain element, however, does not significantly alter either our calculations or conclusions.

Figure 2.2 shows a clear rising trend in reduction factors for the heavier mass elements. This is in qualitative agreement with the fractionation signature expected from gravitational settling. While the right-hand side of Figure 2.2 may at first seem reminiscent of the standard FIP effect plots, with the low FIP elements having the largest values (see Figure 1.6 which was taken from von Steiger et al. 1997), the values in our figure indicate depletions rather than enhancements and as such represent the opposite of what is expected in FIP-fractionated wind. There is no apparent ordering of the reduction factors according to FIP. The low FIP elements also happen to be heavier and will have large reduction factors anytime there is mass-dependent fractionation.

2.3.3 Comparison to UVCS

Figure 2.3 compares the X/H ratios inside our dropout to those Raymond et al. (1997a) remotely observed inside the center of an equatorial streamer. While it is important to note here that our example dropout and the streamer of Raymond et al. are separated by 7 years, there is still some use in making the comparison. The black circles in Figure 3 represent the ratios within our dropout while the red diamonds are the ratios computed from the elemental abundances reported in Table VII of the Raymond et al. paper. Also shown are the ratios outside the dropout (blue squares) along with typical photospheric (Grevesse & Sauval 1998) and coronal (Feldman et al. 1992) values (magenta and dashed, cyan lines respectively). We can see that the ratios within our dropout compare favorably, within the error bars, with those of the streamer center. Error bars are not shown for the UVCS measurements since uncertainty and error ranges were not published within the Raymond et al. paper. We also cannot say much about carbon since we lack a streamer abundance to compare with. As mentioned in Section

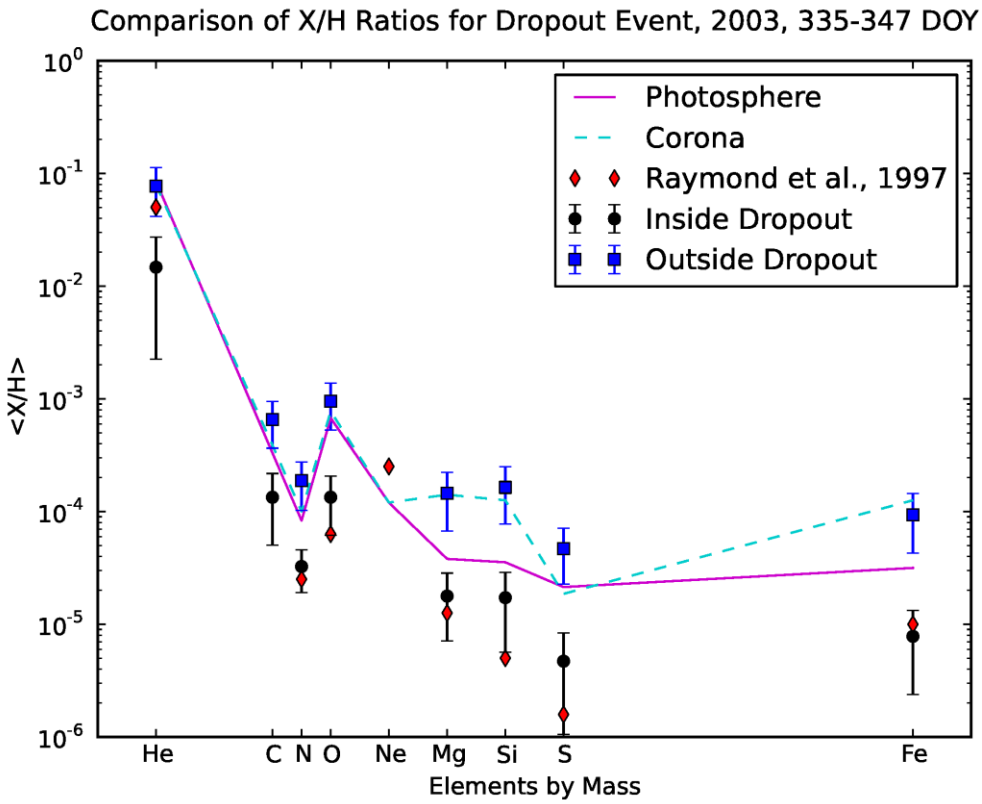

Figure 2.3: Comparison of X/H ratios inside the 335–347 DOY, 2003 dropout event (black circles) to ratios within the streamer core observed by Raymond et al. (1997a, red diamonds). Also shown are the ratios ±5 days outside the dropout (blue squares), in the photosphere (magenta line; Grevesse and Sauval 1998), and the corona (dashed, cyan line; Feldman et al. 1992). The observed dropout ratios are most similar to the streamer core.

2.1, Raymond et al. argue that the abundances in the streamer center are partially due to gravitational settling. This would seem to lend further credence to our analysis of the mass-dependent fractionation seen in Figure 2.2. However, we must be careful not to read too much into the apparent agreement in Figure 2.3 since, as stated earlier, our dropout and the streamer of Raymond et al. represent observations from two different parts of the solar cycle. The primary point of Figure 2.3 is to show that the plasma within our example dropout is entirely unlike typical coronal or photospheric plasmas which have been shown to be similar to slow and fast solar wind, respectively (von Steiger et al. 1997, 2000; Zurbuchen et al. 2002). Instead, the plasma within our dropout is most similar to that observed within a streamer

center which was thought to be magnetically closed, thereby suggesting that the plasma within our dropout originated from a similar structure.

2.4 SURVEY STATISTICS

2.4.1 Quantifying "Mass Fractionation"

In our analysis, we used a simple mathematical test to determine if a given dropout appears to be mass fractionated or not. We began by fitting a series of linear equations to the reduction factors of each dropout. In each iteration of the series, we omitted one of the elements from the fit (this is known as the "Jackknife" method) and thereby obtained a distribution of slopes reflecting the general trend in the reduction factors. In all of the fits, we ignored the reduction factor for He for two reasons: (1) given its considerably higher density compared to the minor ions, He is dynamically important and most properly considered as part of the main ion population (Bodmer & Bochsler 2000); and (2) He is known to be depleted near the HCS (Borrini et al. 1981; Suess et al. 2009). Both factors could lead to anomalously large reductions in He which could interfere with our process to determine the overall trend in reduction factors. Finally, we computed the correlation coefficient, r, for each average fitted slope. According to standard statistical tables (David 1938), the 95% significance level for 5 degrees of freedom (7 data points, one per element, minus 2 variables) is denoted by $|r| \geq 0.754$.

Of the 257 dropouts identified in the period 2001–2009, 195 (75.9%) have a general upward trend where the average minus one standard deviation of the fitted slopes is positive. However, only 91 (35.4% of all events) have a strong correlation ($|r| \geq 0.754$) between element mass and reduction factor. It is only this subset of 91 events that we define as "mass fractionated". As for the remaining 166 non-mass-fractionated events, 104 (40.5%) have positive trends with moderate or weak correlation, 23 (8.9%) have negative trends (4 with strong correlation, 19 with moderate or weak), and 39 (15.2%) have no clear trend up or down (note that percentages are relative to the entire set of 257 dropouts). Figure 2.4 shows the distribution of events into common confidence ranges. Higher confidence levels correspond to a stronger correlation between element mass and relative reduction factor.

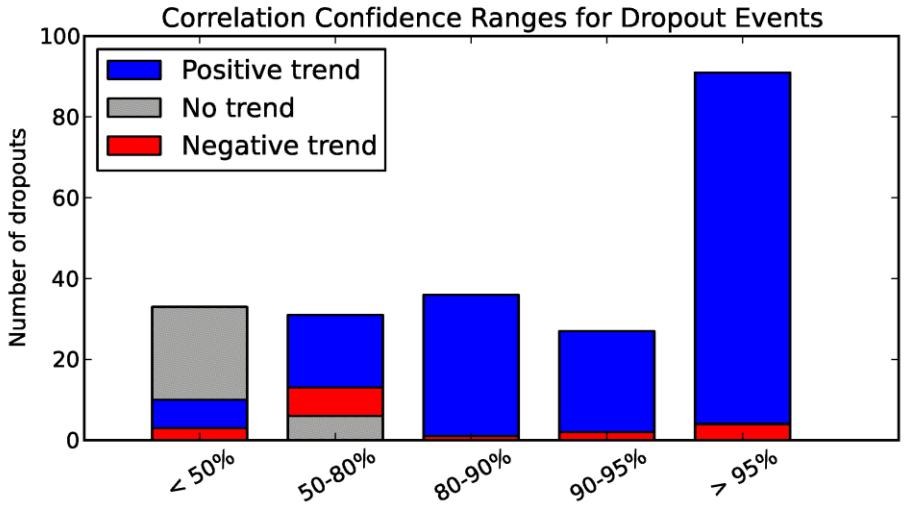

Figure 2.4: Distribution of dropout events into common confidence ranges. The higher the confidence levels, the stronger the correlation between element mass and relative reduction factor. We define only the 91 positive trend events in the ≥ 95% range as "mass fractionated."

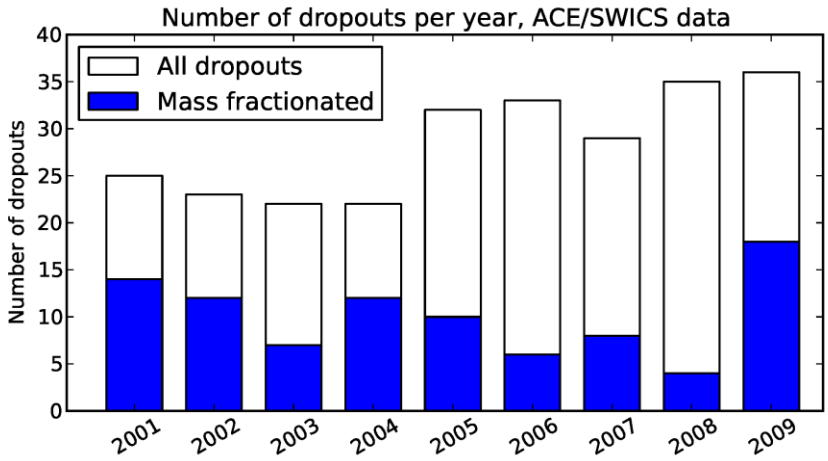

Figure 2.5: Number of potential dropouts per year. Shaded regions indicate mass-fractionated cases. There are more total dropouts near the 2008 solar minimum; however, the mass-fractionated cases do not seem to have any solar cycle dependence.

2.4.2 Occurrence Rate over Most of a Solar Cycle

Figure 2.5 is a bar graph depicting the yearly distribution of all possible dropouts with filled regions indicating the portion of them which are mass fractionated according to the method of Section 2.4.1. It is interesting to note that while there seem to be more dropouts during the recent anomalous minimum, which exhibited a 3% reduction in solar wind speed,

17% reduction in density, and 14% reduction in temperature when compared to previous minima (McComas et al. 2008). It is entirely possible that some, but not necessarily all, of the other dropouts originally had mass-fractionated plasma but the abundance signatures were later erased by other processes, such as those described by Schwadron et al. (1999).

2.4.3 Average Values

The average duration of all possible dropouts is 17.56 ± 12.75 hr and the mass-fractionated cases are similar with an average of 16.33 ± 10.17 hr. Within the mass-fractionated cases, iron is depleted by factors ranging from 2.12 to 27.69 with an average of 7.42 ± 5.04. Table 2.1 shows the average elemental ratios relative to hydrogen for the 91 mass-fractionated dropouts. For comparison, we have computed the average ratios within typical slow solar wind (von Steiger et al. 2000, 2010), the photosphere (Grevesse & Sauval 1998), and the solar corona (Feldman et al. 1992). The uncertainties listed for our results were computed using the standard error of the means. The values shown in parentheses represent the reduction factors of the mass-fractionated dropouts relative to the given reference ratios (i.e., $[X_{Ref}/H_{Ref}]$ / $[X_{MF}/H_{MF}]$).

Table 2.1 provides some qualitative details concerning the relative importance of fractionation processes in the dropout events without needing to resort to a complete theoretical or mathematical model. When compared to typical slow wind or coronal X/H ratios,

Table 2.1: Comparison of Average Ratios Relative to Hydrogen.

Ratio	Mass-Fractionated Dropouts	Typical Slow Solar Wind[a]	Photosphere[b]	Corona[c]
He/H	$1.14 \pm 0.15 \times 10^{-2}$	3.91×10^{-2} (3.43)	8.51×10^{-2} (7.46)	7.94×10^{-2} (6.96)
C/H	$9.76 \pm 0.97 \times 10^{-5}$	2.91×10^{-4} (2.98)	3.31×10^{-4} (3.39)	3.89×10^{-4} (3.99)
N/H	$2.41 \pm 0.20 \times 10^{-5}$	3.41×10^{-5} (1.41)	8.32×10^{-5} (3.45)	1.00×10^{-4} (4.15)
O/H	$1.10 \pm 0.12 \times 10^{-4}$	4.35×10^{-4} (3.95)	6.76×10^{-4} (6.15)	7.76×10^{-4} (7.05)
Mg/H	$1.81 \pm 0.19 \times 10^{-5}$	6.30×10^{-5} (3.48)	3.80×10^{-5} (2.09)	1.41×10^{-4} (7.79)
Si/H	$1.56 \pm 0.17 \times 10^{-5}$	6.50×10^{-5} (4.17)	3.55×10^{-5} (2.28)	1.26×10^{-4} (8.08)
S/H	$4.92 \pm 0.48 \times 10^{-6}$	2.17×10^{-5} (4.41)	2.14×10^{-5} (4.35)	1.86×10^{-5} (3.78)
Fe/H	$7.20 \pm 0.74 \times 10^{-6}$	4.91×10^{-5} (6.82)	3.16×10^{-5} (4.39)	1.26×10^{-4} (17.5)

Notes: (a) Calculated using *Ulysses* average slow wind X/O ratios of von Steiger et al. (2000) and the H/O ratio of von Steiger et al. (2010). (b) From Grevesse & Sauval (1998). (c) From Feldman et al. (1992).

the mass-fractionated dropouts show greater depletions for heavier elements, with Fe being the most depleted. This is as to be expected of a mass-dependent process such as gravitational settling and further confirms that the apparent ordering according to mass in the "mass-fractionated" dropouts is a statistically important effect and not some artifact caused by the averaging done in our analysis. The fractionation pattern when comparing the dropouts to the photosphere is more complicated. We can nevertheless still glean one useful conclusion from the comparison. Most fractionation processes, such as FIP-fractionation, are defined relative to photospheric abundances and are caused by processes that occur in the chromosphere or corona (Geiss 1982; Meyer 1991). If gravitational settling was considerably stronger than all other fractionation processes inside the mass-fractionated dropouts, we would expect to see a moderate or at least weak correlation with mass when compared to the photospheric abundances. However, as can be seen in the reduction factors of Column 3 of Table 2.1, this is clearly not the case. Therefore gravitational settling can, at most, only be moderately stronger than other fractionation processes rather than overwhelmingly dominant. The exact mixture of processes responsible for the mass-fractionated dropouts is, of course, beyond the limited insight afforded by our analysis of data trends and is a question that can perhaps be best answered within the framework of a full mathematical model (we attempt to construct such a model in Chapter V).

2.4.4 Comparison of Mass-Fractionated Dropouts in Other Plasmas

Similar to Figure 2.3, Figure 2.6 depicts the elemental ratios from Table 2.1 in graphical form. Of particular interest is the comparison between the average X/H ratios of all 91 mass-fractionated dropouts (black circles) and the X/H ratios inside the streamer center observed by Raymond et al. (red diamonds). We have also plotted the median dropout X/H ratios (black line). As can be seen in Figure 6, the average and median dropout X/H ratios tend to be a bit higher than the streamer center but are still much lower than the photospheric, coronal, and slow wind ratios (magenta, cyan, and blue lines, respectively). This suggests that plasmas with heavy ion dropouts are, as a whole, most similar to observations of the streamer center, which Raymond et al. argued must be a magnetically closed region that has been, at least partially,

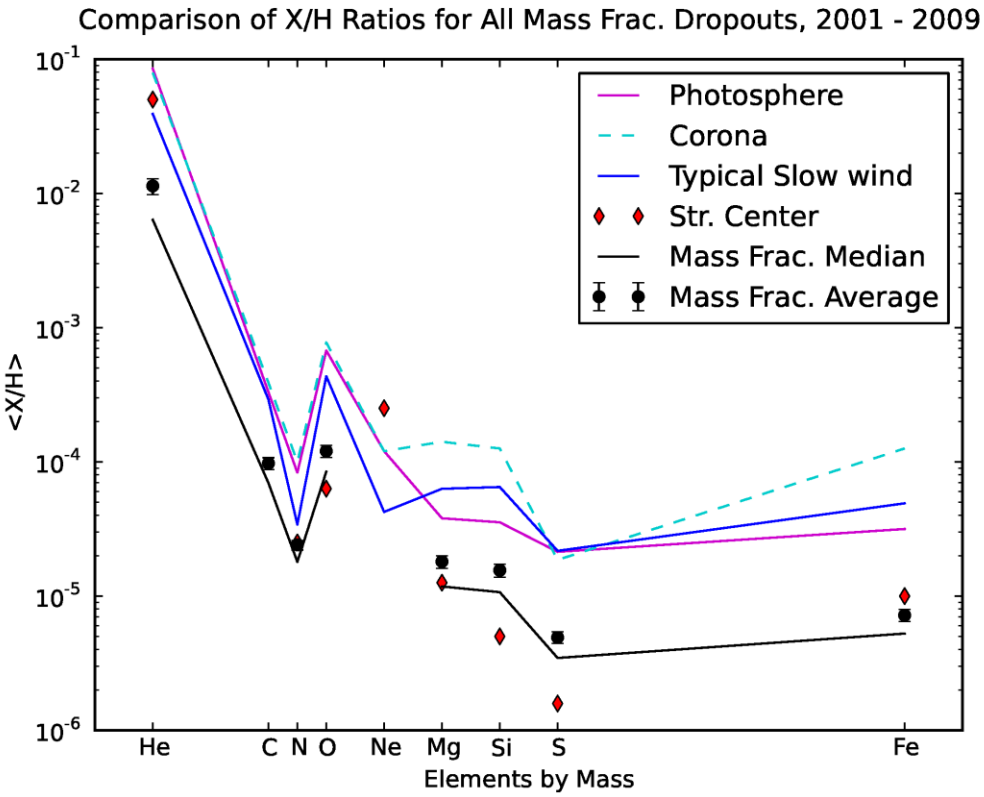

Figure 2.6: Average X/H ratios within all 91 mass-fractionated dropouts (black dots) compared to the X/H ratios inside the streamer center observed by Raymond et al. (1997a; red diamonds). Error bars on the dropout values represent the standard error of the means as found in the first column of Table 1. Also plotted are the median dropout values (black line) and typical photospheric (magenta line; Grevesse & Sauval 1998), coronal (cyan line; Feldman et al. 1992), and slow solar wind ratios (blue line; von Steiger et al. 2000, 2010). Like in Figure 3, the average dropout ratios are most similar to those in the streamer core.

depleted by gravitational settling. Note, however, that Figure 6 compares an ensemble of dropouts (spanning the years 2001–2009) with a single specific streamer observed in 1996 July and the quantitative details of this comparison should not be over interpreted.

2.4.5 Relation to Stream Interfaces

Among the 91 mass-fractionated dropouts, 44 (48.4%) occur either within stream interaction regions on the Jian et al. SIR list (23 cases) or just outside of an SIR within 2 days (21 cases). Such a low correlation is not entirely surprising because mass-fractionated dropouts observed in situ are expected to map to the edges of coronal holes. SIRs on Jian's list form

when a stream of slow-velocity wind is overtaken by a faster stream. Therefore, plasmas near these SIs represent only the preceding edges of coronal holes. Since gravitational settling may occur within closed loops on either side of a coronal hole, we should not expect much more than half of all mass-fractionated dropouts to occur near the preceding edge, stream interfaces. Additionally, we can rule out the possibility that these dropouts are caused by some kind of process or interaction inside the compressive region of slow-to-fast SIR since in those events we would expect to see a clear preference for the leading edge SI.

This lack of preference persists when we consider all of the dropouts and not just the mass-fractionated ones. Of the 257 possible dropouts, 158 (61.5%) are found near SIs. This amounts to ~44% of the 359 SIRs on the Jian list between the years 2001 and 2009. Again, as with the mass-fractionated cases, the distribution of dropouts is split almost evenly between events occurring inside SIRs (86 cases) and just outside SIRs within 2 days (72 cases). Figure 2.7 is a histogram of the time between all 158 correlated dropouts and the nearest SI. Negative numbers indicate dropouts that come before the SI and positive numbers denote those that come after. The peak of the distribution is less than a day before the SIs, a period most closely

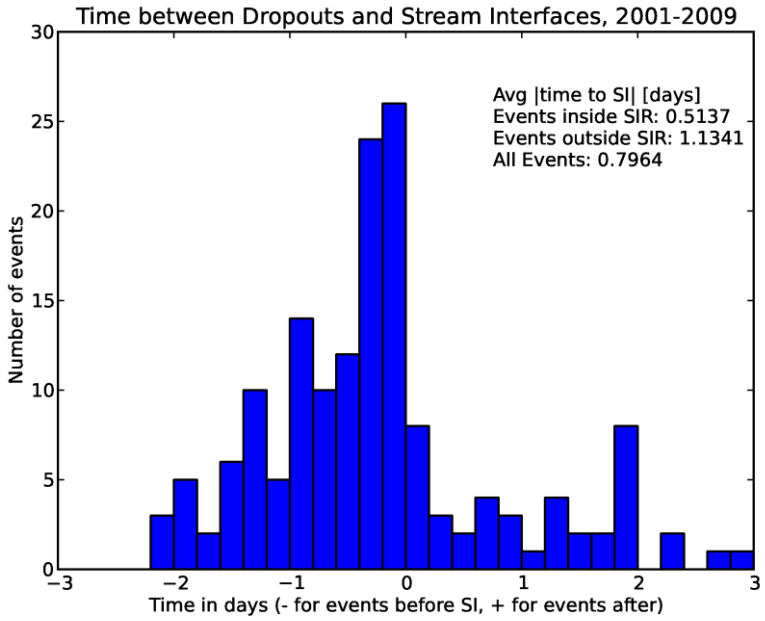

Figure 2.7: Time in days between dropout centers and nearby stream interfaces (SIs) for the 159 events, out of all 257 possible dropouts, which are reasonably close to SIs. Negative (positive) numbers indicate dropouts that come before (after) the SI. Most of the dropouts are found right before the SI, during periods of slow solar wind.

tied to slow solar wind. The average of the absolute time offsets is 0.5137 days for events occurring inside SIR, 1.1341 days for events occurring near but outside SIR, and 0.7964 for all events together. It is difficult to say whether the remaining 99 uncorrelated dropouts have any relation to the trailing edges of coronal holes. This is because the fast stream outruns the slow stream that follows and creates a sort of rarefaction with no clear boundaries and a fair bit of mixing. Further research, perhaps using the variability of charge state ratios to differentiate between streams, should hopefully yield some proper statistics. In particular, it will be interesting to see if the smaller peaks in Figure 2.7 between 1 and 2 days after the SI have any relation to the trailing edges of particularly narrow coronal holes.

2.5 SUMMARY AND CONCLUSIONS

We have shown here ACE/SWICS observations of heavy ion dropouts within the solar wind. These observations represent the first in situ measurements of mass-fractionated solar wind and as such lend further credence to models that associate slow, unsteady wind with plasma from coronal loops. Key observations include the following:

1. Most dropouts are found embedded within slow solar wind plasma with about half of them lying less than 1.5 days from interfaces between slow and fast streams. These SIs correspond to the boundaries between open and closed magnetic fields in the solar corona, where previous studies (Raymond et al. 1997; Feldman et al. 1999) found strong evidence for gravitational settling. The correspondence between SIs and dropout periods is important because it suggests that those dropouts found right before an SI originated from a coronal loop on the edge of a coronal hole. Additionally, the given occurrence rate does not indicate any preference for the leading or trailing edge of a coronal hole and rules out the possibility that the dropouts are caused by interactions within the SIs themselves.
2. Heavier ions generally exhibit larger depletions, with 35.4% of all possible dropouts demonstrating mass-dependent fractionation. This is consistent with what we should expect of gravitational settling. Within the mass-dependent cases, iron was found to be depleted by factors ranging from 2.12 to 27.69 with an average of 7.42. Some of these

cases compare favorably with the aforementioned remote observations, giving us added confidence that the fractionation in those events is, at least partially, due to gravitational settling.

3. The yearly number of mass-fractionated dropouts does not appear to have a strong solar cycle dependence. However, there are more total dropouts found near solar minimum. It is entirely possible, but not yet determined, that some of the non-mass-fractionated cases represent plasmas which were initially depleted by gravitational settling but the mass dependence was partially scrambled and hidden by other coronal fractionation processes.

One quite reasonable question to ask is why these dropouts have not been previously reported. There are two main reasons for this. First of all, the dropouts discussed in this paper are on the order of less than a day. Therefore any study looking at long-term variations using averages over more than a day, or in some cases even just half a day, would not have been able to find the depletions. Second, most previous studies of heavy ion abundances have used the X/O elemental ratios rather than the X/H ratios we used here. This was because properly cross-calibrated H densities were not available from the SWICS instrument until recent years. Since both O and Fe are depleted in the observed dropouts, the corresponding dips in the Fe/O would be smaller and more easily overlooked.

The in situ observations of solar wind elemental abundances are an important piece of solar and heliospheric research. Mass-fractionated plasmas linked to gravitational settling can provide unique insight into the subtle interplay between coronal processes. Additionally, mass fractionation can be used as a signature to connect in situ observations to elemental abundances determined by remote spectroscopy. Dropouts such as those presented here also yield clues about the source regions of solar wind and could be used as an additional test of slow wind origin theories.

CHAPTER III

CORONAL SOURCES, ELEMENTAL FRACTIONATION, AND RELEASE MECHANISMS OF HEAVY ION DROPOUTS IN THE SOLAR WIND

The text in this chapter was published in: Weberg, M. J., Lepri, S. T., & Zurbuchen, T. H. (2015), *The Astrophys. J.*, ***801***, 99. The abstract and introductory sections have been combined and edited for inclusion in this dissertation.

3.1 INTRODUCTION

In this chapter we consider and attempt to answer three fundamental questions concerning heavy ion dropouts: (1) "Where are the source loops located in the large scale corona?", (2) "How does the interplay between coronal processes influence the end elemental abundances?", and (3) "What are the most probable release mechanisms?" We begin by expanding upon our earlier research to provide more complete dropout statistics over a longer period of time. Next we investigate the ordering of the elements inside dropouts with respect to first ionization potential and mass. We also analyze the temporal and spatial variability of heavy ion dropouts and their correlation with heliospheric plasma and magnetic structures. Finally, we consider probable coronal source regions and discuss these results in the context of the prevailing solar wind theories and the processes they posit that may be responsible for the release of coronal plasma into interplanetary space.

3.2 HEAVY ION DROPOUTS

3.2.1 Occurrence Rates and General Statistics

In our previous chapter, we identified 257 heavy ion dropouts between the years 2001 – 2009. Dropouts were identified primarily as time periods longer than 4 hours of low Fe/H more than one standard deviation (STD) below the local Carrington Rotation (CR) average with some of the data points more than two STD below the CR average. This last criterion has no minimum time duration requirement (any number of very low data points is sufficient) and was imposed to exclude small events within normal solar wind variability. Special care was taken to exclude events with data gaps, sharp, small-scale enhancements in hydrogen density (which gives spurious low Fe/H ratios with nominally the same iron densities), and those which occurred during known ICMEs on the most up-to-date version of the Richardson and Cane list (2010). Using the same methodology, we now extend our study to include five more years of data: 1998 – 2000 and 2010 – 2011. The resulting 14 years of observations span more than a solar cycle, from early cycle 23 to early-mid cycle 24 (February 1998 to August 2011).

Figure 3.1 shows the annual number of dropouts. The red line corresponds to the smoothed monthly sunspot number available from the World Data Center (SILSO, http://sidc.be/silso/). For the sake of determining long-term trends, the bars for 1998 and 2011 have been normalized assuming the same observation rate for the missing months. The observed values are reported in Table 3.1. Altogether we have identified 379 total dropouts. The blue shaded regions in Figure 3.1 indicate the number of the dropouts which were found to be strongly mass fractionated (i.e. heavier ions more depleted that lighter ions) relative to the nearby slow type solar wind. The method used to determine and quantify mass fractionation is the same as described in section 2.4.1 with one notable difference: this time the X/H ratios inside the dropouts were only compared relative to the nearby (± 5 days) *slow* wind rather than just all nearby solar wind as before. This change is motivated by the fact that heavy ion dropouts appear to originate from similar regions of the Sun as slow solar wind. Comparing to nearby slow wind allows for cleaner, less ambiguous fractionation trends and minimizes the impact of other fractionation processes such as the FIP effect which is different in the fast wind (we explore this process more in section 3.2.2). Based on our analysis and classification

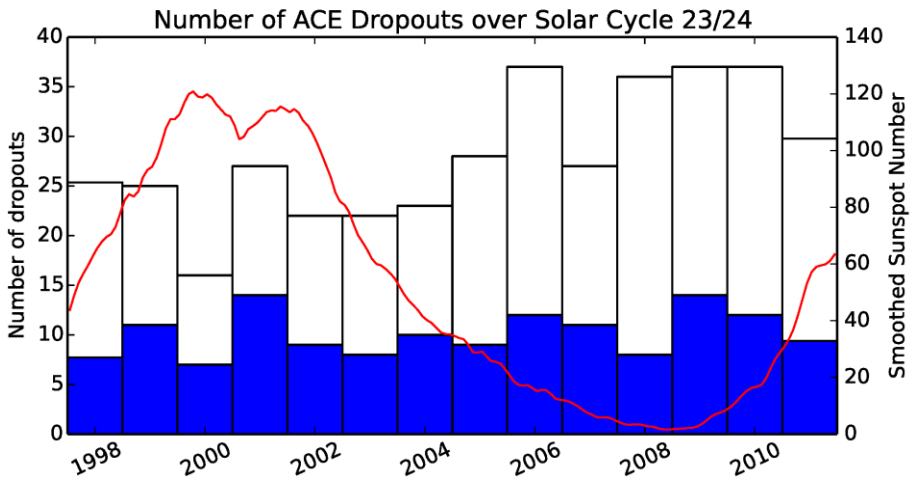

Figure 3.1: Annual number of heavy ion dropouts over solar cycle 23/24 (1998, DOY 35 to 2011 DOY 233). The red line corresponds to the smoothed monthly sunspot number from WDC-SILSO. The blue bars indicate the subset of events which are strongly mass fractionated. The bars for 1998 and 2011 have been normalized assuming the same observation rate for the missing months. The observed values are reported in Table 3.1.

scheme, 36.4% (138 events) of all dropouts exhibit mass dependent fractionation.

As we noted in our previous paper and can see in Figure 3.1, there does not appear to be an immediately obvious correlation between solar cycle and yearly dropout numbers. If we focus on five year intervals centered on solar maximum and minimum, we find that there are on average 12 fewer dropouts per year around solar maximum (1999 – 2003; 22.4 ± 3.72 per year) than there are around solar minimum (2006 – 2010; 34.8 ± 3.92 per year). However, the number of mass fractionated dropouts remains fairly constant with an average of 9.9 ± 2.5 per year. Therefore the relative fraction of mass fractionated dropouts is lower during solar minimum, dropping from 43.4 ± 5.1% to 33.1 ± 6.3%. While it is possible that ICMEs, by disrupting the coronal conditions required for gravitational settling, could be partially responsible for the fewer dropouts seen around solar min, the steady observation of strongly mass fractionated dropouts suggests that there exists some fraction of source regions that remain relatively unperturbed by ICMEs. In the future we plan to more closely investigate dropouts found near ICMEs and provide a quantitative analysis of their interactions (if any).

Dropouts have been observed to have durations ranging from 6 to ~82 hours. However these durations are not normally distributed with only 21.6% (82 events) having durations

Table 3.1: Yearly Dropout Numbers, Relative Fraction of Total Solar Wind, and Median Durations.

Year	Number of Dropouts	Number of Mass Frac.	% of all SW inside		Median Duration [hr]	MAD [hr]
			dropouts	*ICMEs*		
1998	23	7	4.7	13.2	10.01	3.74
1999	25	11	4.5	11.4	13.99	3.91
2000	16	7	3.6	16.8	17.00	7.91
2001	27	14	5.0	17.3	12.41	5.59
2002	22	9	4.7	9.6	15.90	6.00
2003	22	8	3.9	6.8	11.82	4.98
2004	23	10	5.0	7.5	14.02	4.01
2005	28	9	5.7	9.1	12.01	6.01
2006	37	12	7.7	3.5	14.02	7.99
2007	27	11	8.2	0.4	16.03	8.02
2008	36	8	6.4	0.7	11.02	5.00
2009	37	14	5.7	2.4	10.01	2.02
2010	37	12	6.8	3.6	10.01	2.02
2011	19	6	4.9	5.0	14.02	6.00
All	379	138	5.5	7.6	12.02	4.03

Note: The rows for 1998 and 2011 report the actual observed number of events rather than the normalized values shown in Figure 3.1.

longer than 24 hours. The presence of extreme outliers means we must turn to the median and the Median Absolute Deviation about the median (MAD) for a better quantification of typical duration and variability. We find that dropouts have a median duration of 12.02 hours and a MAD of 4.03 hours. Table 3.1 explores in further detail the yearly numbers and durations of dropouts. We find that the median duration is fairly uniform across the solar cycle. It is significant to note that, between February 1998 and August 2011, heavy ion dropouts comprise 5.5% of all solar wind observed by *ACE*. This is on the same order of magnitude as the 7.6% of solar wind contained within ICMEs on the Richardson and Cane list. We also note that the yearly fraction of ICME wind varies greatly from 17.3% at solar maximum to 0.4% at minimum. Dropouts, on the other hand, are much more consistent with only a small difference between maximum and minimum.

3.2.2 Elemental Composition

Figure 3.2 compares the relative X/O ratios inside dropouts to those of the fast and slow solar wind. Ratios are given relative to the photospheric values and are ordered according to

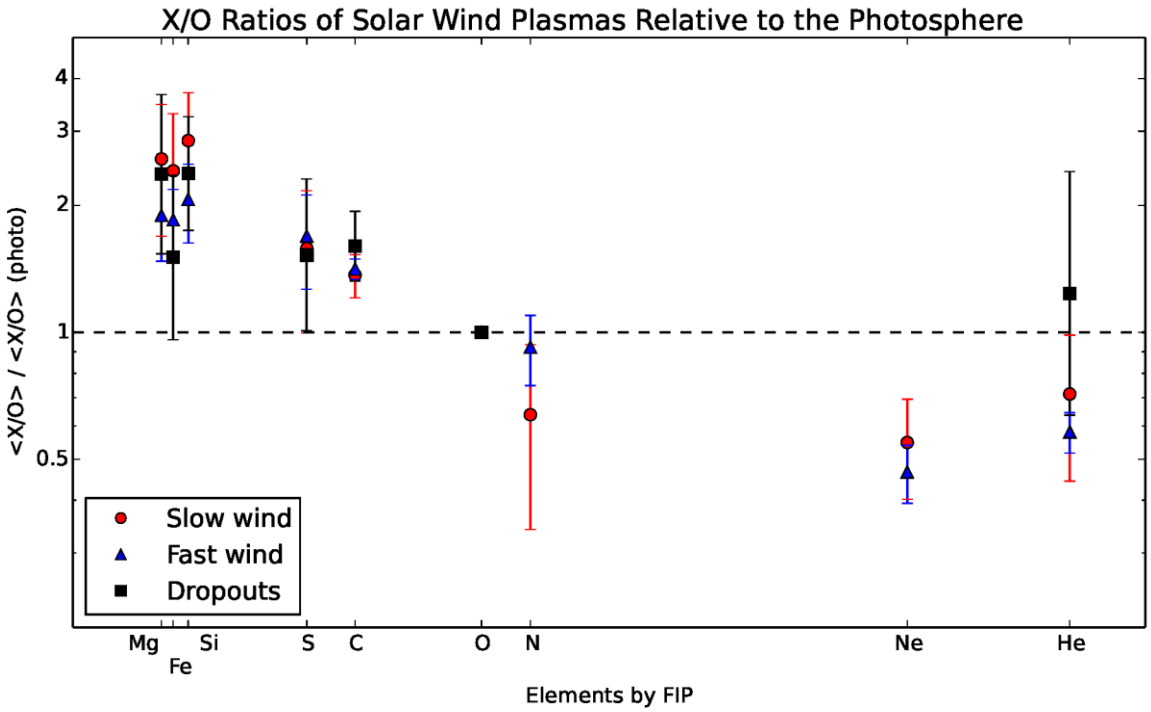

Figure 3.2: Relative X/O ratios inside all dropouts (black squares) normalized by their photospheric values. Typical slow (red circles) and fast (blue triangles) wind values are plotted for comparison and are taken from von Steiger et al. 2000.

FIP. This type of plot is the standard means of studying the FIP effect in solar plasmas. With the exception of iron, heavy ion dropouts appear to have X/O ratios similar to the slow solar wind and likewise exhibit a low-FIP enhancement. This result is not entirely unexpected; within a typical dropout, all of the elements are depleted to some extent, including O. Therefore the relative X/O ratios remain relatively unchanged even though the absolute abundances of the input elements are lower. The one exception to this is iron – which being the heaviest element observed by SWICS – is significantly more depleted than O such that the Fe/O ratio is noticeably lower inside the dropout. Furthermore, current theories of the FIP effect place the driving mechanism in the chromosphere (Laming 2004) while gravitational settling, although occurring over all heights, would be most evident higher up in the corona. This means that solar plasmas are already FIP fractionated by the time they reach the corona and we would expect to still see some evidence of this even after gravitational settling has taken place.

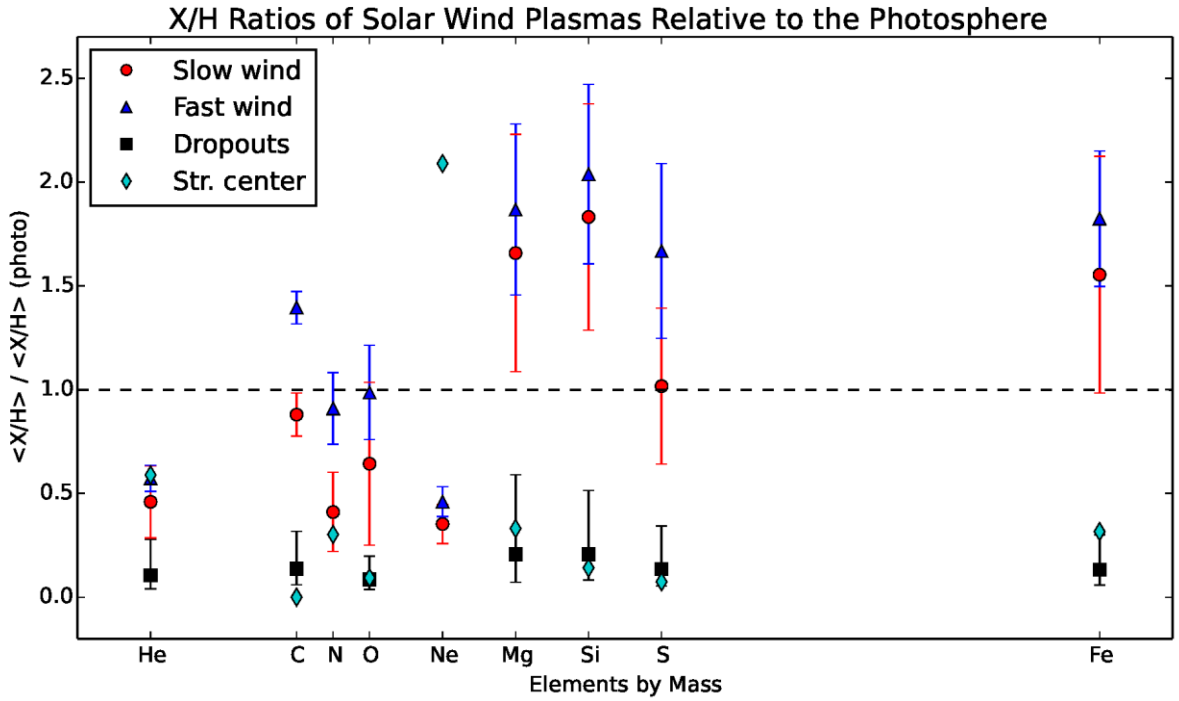

Figure 3.3: Relative X/H ratios inside all dropouts (black squares) normalized by their photospheric values. Along with typical slow (red circles) and fast (blue triangles) wind values from von Stieger et al. 2000 (using the O/H values of von Steiger et al. 2010), we also plot the elemental abundances remotely observed inside a large, streamer belt loop by Raymond et al., (1997a, cyan diamonds).

The effects of gravitational settling are more evident when looking at the X/H ratios. In Figure 3.3 we compare the [X/H] / $[X/H]_{photo}$ ratios of dropouts to typical fast and slow solar wind (computed using averages from von Steiger et al. 2000 and the O/H ratio of von Steiger et al. 2010). Elements are arranged in order of mass. We also show the composition of a single, large helmet streamer spectroscopically observed by Raymond et al. (1997a) which was found to be mass fractionated. As expected, the slow and fast wind values can be explained by FIP fractionation with the low FIP elements (Mg, Si, & Fe) being enhanced over those with high FIP (He, C, N, O, S). Additionally, it can now be seen that all the elements inside the dropouts are, in fact, depleted relative to the photosphere; a fact that was not apparent from just looking at the X/O ratios. There are also some clear mass dependent trends, particularly in the heaviest elements although they still exhibit increased ratios in accordance with FIP fractionation. It is worth noting here that the "error bars" shown in Figure 3.3 indicate the standard deviation in

the mean X/H ratios rather than the instrumental uncertainties in their values (which are much smaller).

In contrast to Figure 3.2, the fast wind values in Figure 3.3 are actually higher than the slow wind due to the fact that the relative O/H ratio is lower in the slow wind (as found in von Steiger et al. 2010). The result is increased slow wind X/O ratios despite slightly lower relative X/H. This observation underlines the usefulness and extra insight provided by analyzing both the X/O and X/H ratios in tandem. Certain data trends that may be hidden in one measurement space can become apparent in the other.

3.3 Relation to Solar Wind Plasma and Magnetic Structures

3.3.1 Structures and Methodology

Now that we have established a fairly complete list of dropouts between the years of 1998 – 2011, we investigate the probable source region locations and release mechanisms in the corona. We do this by correlating the dropouts with plasma and magnetic structures embedded within the underlying solar wind. For example, if a particular dropout originated from a coronal streamer we would expect it to be well correlated with a heliospheric current sheet (HCS) crossing and a stream interface since coronal streamers are known to lie below the HCS and emit slow velocity solar wind. In our analysis we focused on magnetic sector boundaries, true heliospheric current sheet crossings, local current sheets and stream interaction regions. Each structure was defined and identified as follows:

- *Magnetic Sector Boundary (SB)* – Since suprathermal electrons (energies > 70 eV) are always flowing away from the sun along local magnetic field lines, their bulk streaming direction (as measured by their pitch angle distribution) is thought to indicate the absolute polarity of the magnetic field line at its footpoint on the sun (Kahler et al. 1996). Parallel streaming electrons indicate outward (i.e. positive) magnetic polarity while antiparallel flows are evidence of inward (negative) directed fields. In our study, a SB was identified by a sudden shift in the 272 eV suprathermal electron pitch angle distribution from parallel to antiparallel (or vice versa). In order to filter out marginal or chaotic events, we require the pitch angles to be fairly steady 6 hours before and after

the shift. Electron pitch angle distributions were acquired using level 3 data from ACE/SWEPAM-E (McComas et al. 1998) available on the ACE science center website (www.srl.caltech.edu/ACE/ASC/DATA/level3/).

- *Heliospheric Current Sheet (HCS)* – We identified HCS crossings by sharp reversals of the magnetic field azimuthal angle (in RTN coordinates) between the nominal angles predicted at Earth by the Parker spiral (135^o and 315^o where 0^o is defined as pointing radially away from the Sun). Additionally we required that reversals were located within 12 hours of a SB and that the magnetic field direction was moderately steady (i.e. < 45^o variation) 12 hours before and after the reversal. In all of this we used the 1 hour data from ACE/MAG data (Smith et al. 1998)
- *Local Current Sheet (CS)* – We defined a local current sheet as a magnetic field reversal without the accompanying flip in suprathermal electron streaming as is found at the HCS. This may indicate either an incomplete crossing of the HCS or local folds and kinks in the IMF caused by interchange reconnection near the cusp of a helmet streamer (Crooker et al. 2004).
- *Stream Interaction Region (SIR)* – SIRs occur wherever a fast velocity solar wind stream overtakes a slow stream. SIRs are found using a variety of plasma criteria and their identification is a large topic of research. For simplicity and reliability, we use a list made by Jian et al. (2011). It should be noted that this list, by definition, does not include the rarefaction regions where fast streams outrun streams of slower wind.

3.3.2 Correlations and Superposed Epoch Analysis

Individual dropouts were required to start or end within 12 hours of the observation of a particular solar wind structure in order to be considered correlated with that structure. Unfortunately the Jian SIR list only goes up to the year 2009, thereby our statistics for 2010 and 2011 are incomplete. For the sake of accuracy, we give separate values for the years 1998 – 2009 (323 events) and 2010 – 2011 (56 events). Table 3.2 summarizes our findings and has a number of interesting features. First, there does not seem to be any significant difference in structure correlations between all dropouts and only those strongly mass fractionated. This

Table 3.2: Percentages of Dropouts Correlated with Certain Solar Wind Plasma and Magnetic Structures.

Structure	SB Only	HCS		Local CS		SIR Only	No Clear Association
		with SIR	*without*	*with SIR*	*without*		
All Dropouts *(1998 – 2009)*	3.1%	14.2%	12.1%	6.2%	9.9%	16.7%	37.7%
All Dropouts *(2010 & 2011)*	7.1%	30.4%		12.5%		50%	
Mass Frac. (All years)	3.3%	15.0%	13.7%	6.5%	10.5%	11.1%	39.9%

Note: SIR data is unavailable for 2010 on; therefore some categories have higher values due to the inability to differentiate between events with SIRs and those without.

suggests that all dropouts have similar distributions of source region types. Secondly, no single structure or combination thereof dominates in such a way as to indicate a very specific coronal source. For example, if a majority of dropouts were found well correlated with both the HCS and a SIR, we could reasonably conclude that dropouts mostly came from large helmet streamers at the base of the HCS and not pseudosteamers, which are often identified in-situ by a SIR without a current sheet of any kind (Wang et al. 2012). Finally, perhaps the most striking feature in Table 3.2 is the relatively large percentage of dropouts (37.7%) that do not appear to be correlated with any of the major solar wind structures.

Figure 3.4 shows a modified superposed epoch analysis plot of all 1998 – 2009 dropouts correlated with SIRs (37.1% of all events), regardless of whether or not HCS, CS, or SB correlated. The averaging for the period prior to the dropouts (left unshaded region) was performed with zero epoch centered on the start of the events. Likewise, the period after the dropouts (right unshaded region) was averaged centered on the event end times. Inside the shaded region we normalized and rescaled each dropout event to the median duration and then averaged the data at each time step. The result is a single plot that describes the average behavior of plasma properties before and after the dropouts while clearly separating the solar wind and dropout data.

As we would expect for events correlated with SIRs, the dropouts averaged in Figure 3.4 exhibit plasma signatures consistent with slow wind found ahead of slow-to-fast solar wind transitions which suggests source regions are outside coronal holes, but near their leading edges. Primary features are the smooth rise in solar wind velocity accompanied by a peak in magnetic field magnitude, an increase (i.e. compression region) of proton density, and a

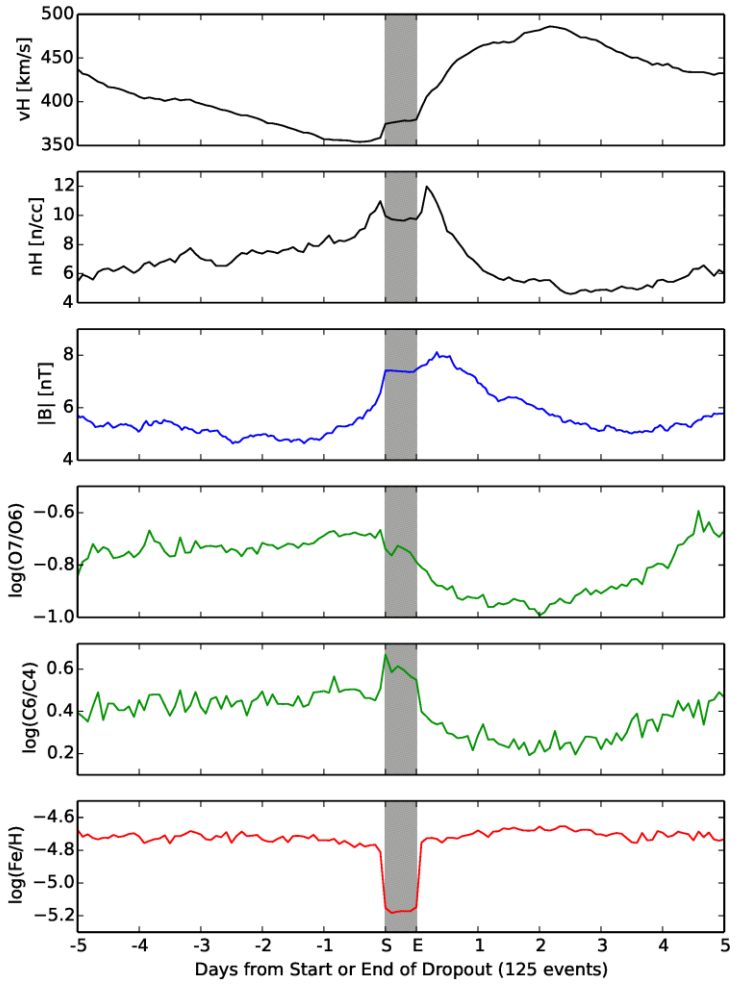

Figure 3.4: Modified superposed epoch analysis plot for all SIR correlated dropouts between 1998 – 2009. These events exhibit plasma characteristics consistent with slow-to-fast solar wind transitions (which are by definition SIRs).

transition from high O7/O6 signifying "slow" type wind) to low O7/O6 ("Fast" type solar wind). Figure 3.5 shows a similar superposed epoch plot for all 1998 – 2009 dropouts uncorrelated with well-defined solar wind structures (last column of Table 3.2). In contrast to Figure 3.4, the events averaged in Figure 3.5 appear to occur after fast-to-slow solar wind transitions, but again in the slow wind. However, the trends, while qualitatively opposite to those described above, are somewhat less distinct. It appears then that these "uncorrelated" events in fact have sources at the *trailing* edges of coronal holes and may potentially help shed light on rarefaction regions in the solar wind which are notoriously difficult to define. When combined with the 37.1% of dropouts correlated with SIRs, we find that 74.8% of all dropouts can be associated

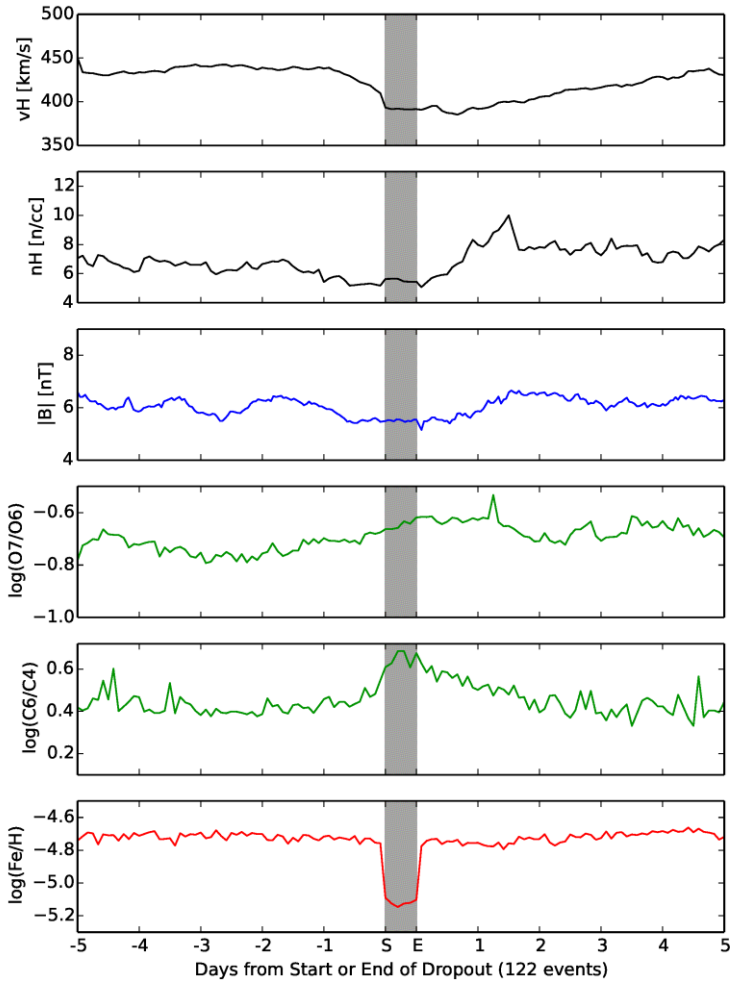

Figure 3.5: Modified superposed epoch analysis plot for all uncorrelated dropouts between 1998 – 2009. These events exhibit plasma characteristics similar to what is expected in fast-to-slow solar wind transitions.

with sources in the closed corona on either side of coronal holes. This is not surprising since it is at the boundary between open and closed fields that one would expect to find the reconnection processes able to transport closed-field plasma out into the heliosphere.

When considering the correlation of dropouts with solar wind structures, it is vitally important to keep in mind the limitations inherent in single spacecraft measurements. In certain three-dimensional geometries it is possible for *ACE*/SWICS to sample plasma from the near vicinity of a given structure without actually crossing and observing the structure itself. Therefore the values in Table 3.2 should be considered as only approximate lower bounds. While SIR correlations are unavailable for 2010 & 2011, we note that the relative fraction of

dropouts correlated with HCS crossings is almost the same as the sum of the "HCS with SIR" and "HCS without" fractions for the years 1998 – 2009. Similar comparisons hold for CS correlated events as well as the dropouts exhibiting no clear correlating structures. It is therefore reasonable to assume the actual correlations in 2010 & 2011 are nearly the same as 1998 - 2009.

3.4 REOCCURRING DROPOUTS

3.4.1 Locations of Dropouts within Carrington Rotations

We now return to a more sophisticated analysis of dropout occurrence rates to see what information we might extract concerning the temporal or spatial distribution of source regions in the corona. Figure 3.6 shows a plot of dropouts within their respective Carrington rotations (CR) across the entire observation interval. The figure can be thought of as one long time series that has been sliced up by CR and stacked on end. The left Y-axis gives the CR number while the X-axis corresponds to the day within the CR. Colored bars represent all heavy ion dropouts we have identified so far. The widths of the bars indicate the actual duration of the events and the colors correspond to the solar wind structure correlations. A careful examination of Figure 3.6 leads to the observation that a large number of dropouts seem to belong to series which reappear over multiple solar rotations (highlighted by red ellipses). Altogether there are 62 potential dropout series comprising 40.6% of all dropouts and lasting up to four Carrington rotations in a row. This systematic reoccurrence suggests that all dropouts within a given series may originate from the same long-lived source region in the corona that is continuously, or semi-continuously, emitting heavy ion depleted plasma.

Before we begin to analyze these "reoccurring dropouts", we calculate the time lag between dropouts to help determine whether or not reoccurrence could be simply explained by a random distribution of events. Figure 3.7 is a histogram of the time difference between each dropout and all subsequent dropouts that come after. The clear peaks centered on multiples of the Carrington rotation period (red vertical lines) confirm that dropout reoccurrence is in fact a reality. If the events were random, we would not expect to see such periodicity. As a further test, we simulated a simple Poisson distribution of random events but

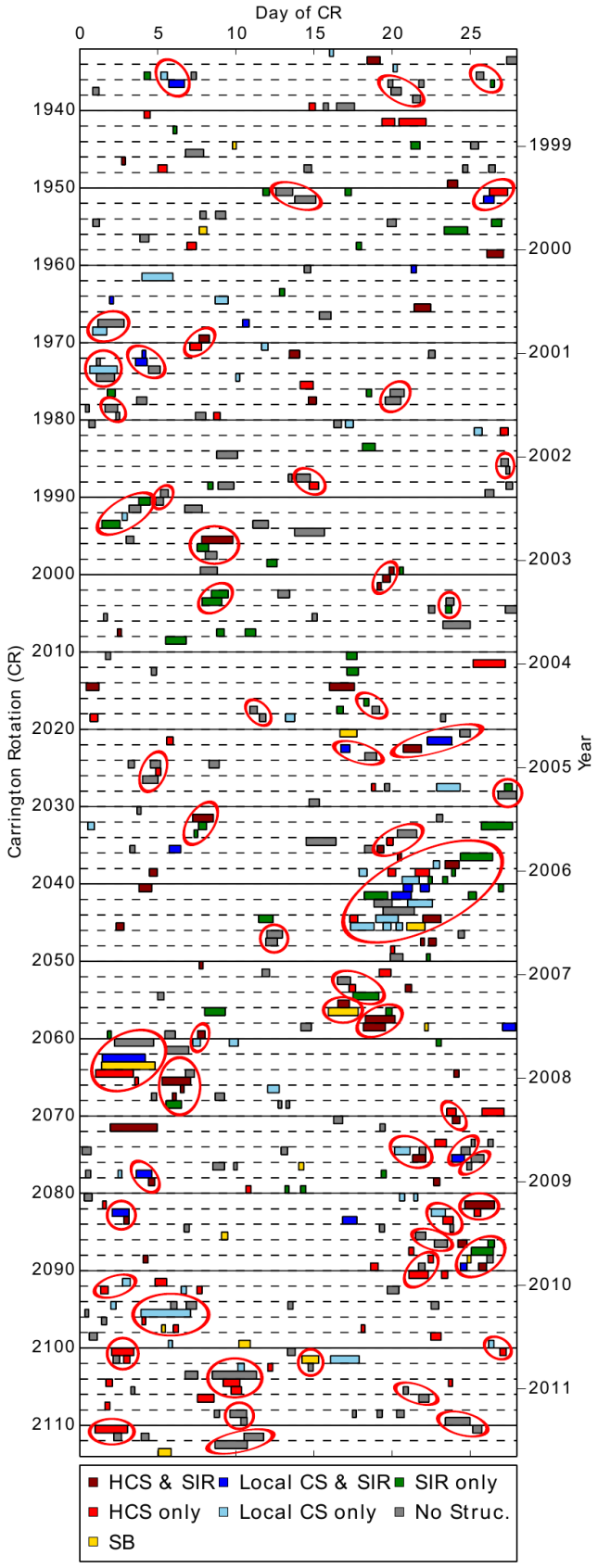

Figure 3.6: Location of dropouts within Carrington rotations. Color corresponds to the dominant structure correlation described in Section 3.3.2. Dropout series which appear to reoccur over multiple CR (red ellipses) suggest source regions which are long-lived structures in the corona.

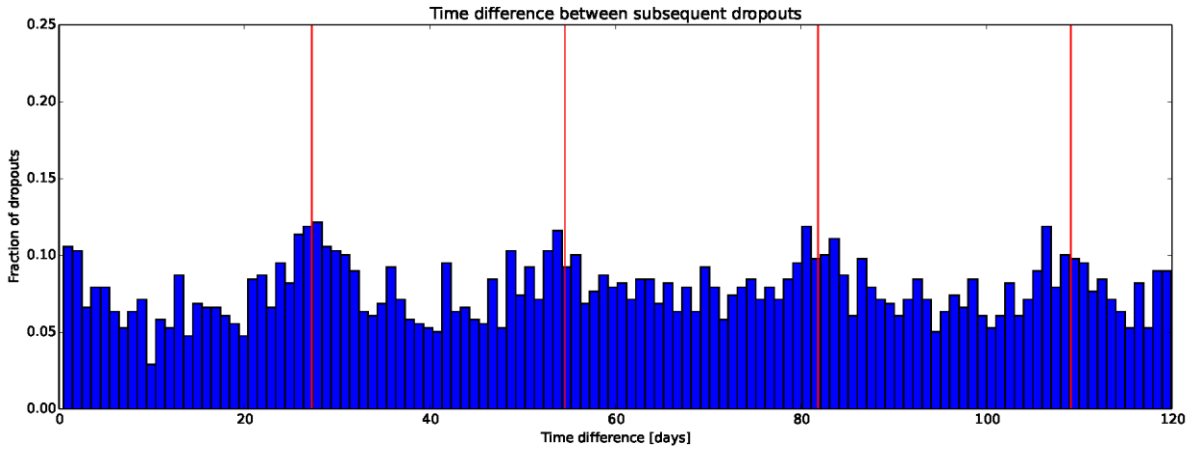

Figure 3.7: Histogram of time differences between each dropout and all subsequent dropouts at come after. The clear peaks centered on multiples of the 27.2753 day Carrington rotation period (red vertical lines) confirm that dropout reoccurrence in not a random process.

were unable to reproduce anything near the reoccurrence rates observed. This indicates that the probability of reoccurrence being the result of a random process is exceedingly low.

3.4.2 Approximate Latitude Calculations

Reoccurring dropouts provide a unique opportunity to study the long-term evolution of coronal processes within the same source region. Furthermore, the time difference between observations of dropouts within a series can be used to estimate the source latitude based on the rotation rate of the source region. Assuming constant solar wind velocity and mostly radial propagation, we first determine the approximate times, t_1 and t_2, that two sequential dropouts in a series left the corona:

$$t_i = t_{i,ACE} - \frac{distance\ to\ Sun}{< V_{SW} >} \qquad [3.1]$$

The angular velocity of the source region is then given by,

$$\omega = \frac{2\pi + \lambda}{t_2 - t_1} \qquad [3.2]$$

where λ is the angle the Earth rotated around the Sun between observations of the dropouts. The angle λ was obtained using the *PyEphem* package for the Python programming language (http://rhodesmill.org/pyephem/). *PyEphem* bases its ephemeris calculations on numerical routines from the scientific-grade *XEphem* astronomical software (Downey 2011). Due to

differential rotation, higher solar latitudes are observed to rotate more slowly than near the equator (Snodgrass & Ulrich 1990). This rotation is described by the equation:

$$\omega = A + Bsin^2(\varphi) + Csin^4(\varphi) \qquad [3.3]$$

where A, B & C are constants with the values 14.713, -2.396, & -1.787 deg/day and φ is the heliographic latitude. By comparing our calculated rotation rates to the standard model for the Sun's differential rotation, we are thereby able to determine the approximate latitude of the source region. It should be emphasized here that our method is only a simple 1st order approximation; nevertheless it is driven directly by data and is free from many of the assumptions made in more complicated mapping techniques using magnetic field line tracing. The most significant assumption we make is that the structure of the corona near our source regions remains relatively stable on the order of a Carrington rotation. While this is certainly true during most of solar minimum, the results at solar maximum should be viewed with a bit of caution since the corona is much more complex at that time.

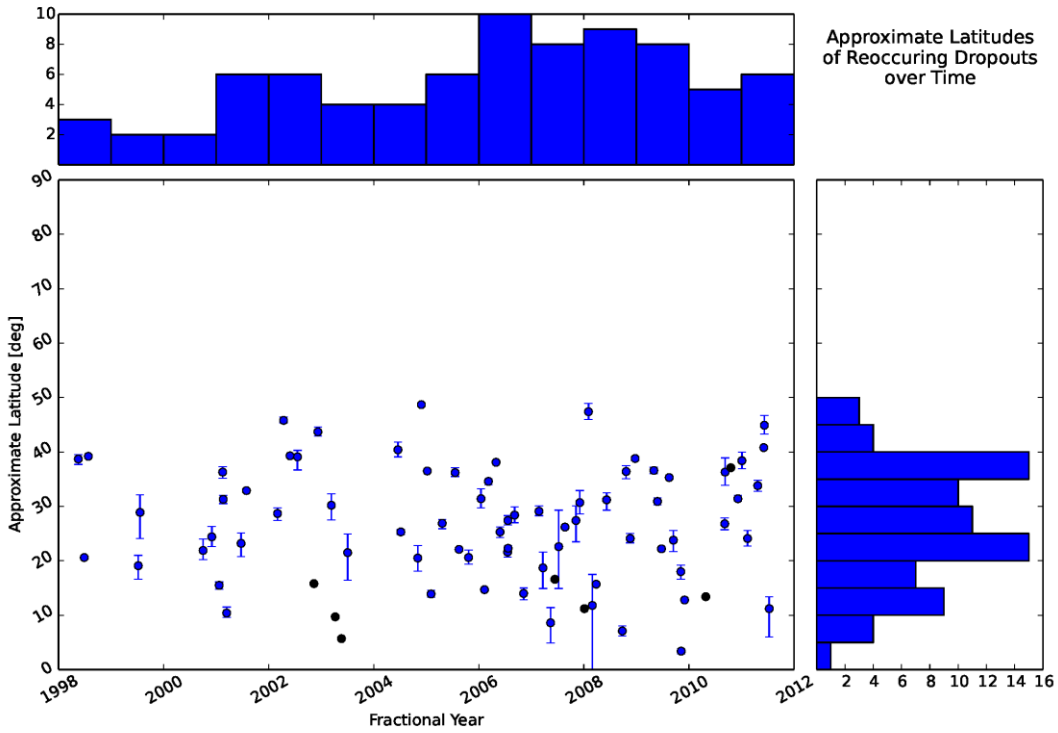

Figure 3.8: Approximate latitudes of reoccurring dropout source regions. The top and right panels are histograms of the data along the X- and Y- axes respectively. Reoccurring dropouts are preferentially located at mid-latitudes between 20^o - 40^o.

Figure 3.8 shows the approximate latitudes calculated for all reoccurring dropouts. In general the uncertainties in latitude are very small and directly linked to the variability of solar wind velocity within the dropouts (faster or slower velocities will result in shorter or longer calculated rotation periods and thereby different final latitudes). Although our method is unable to distinguish between north and south solar hemispheres, we find that most reoccurring dropouts seem to originate from a band between 20^{o} – 40^{o} latitude, around the same latitudes as low latitude coronal holes and helmet streamer loops (Belik et al. 2004). It is unclear, however, why very few dropouts are observed closer to the equator. This could be due to the limitations and approximate nature of our calculation method, an observational bias of *ACE* itself, or an actual effect worthy of more study. One possible explanation is that even when the top of a large loop or streamer lies in the ecliptic plane, the legs are rooted at higher latitudes and thereby rotate at a slower rate than the equatorial solar surface.

3.4.3 Correlations and Composition of Reoccurring Dropouts

Table 3.3 gives the solar wind structure correlations for reoccurring dropouts. When compared to the values in Table 3.2, we find that reoccurring dropouts are slightly (~3%) more strongly correlated with SIRs but the relative fractions are more or less the same and the difference could be due to uncertainty in structure identifications. The statistics for the later years (2010 & 2011) are too low to make definite conclusions (only 22 events total in those years) however they do show similar fractions as we found in Table 3.2. The overall similarity in structure correlations between all dropouts and only the reoccurring events suggest that some of the non-reoccurring dropouts may also have their origins in long-lived coronal loops. In such an event the specific three-dimensional geometry may be unfavorable for ACE to observe

Table 3.3: Percentages of Reoccurring Dropouts Correlated with Certain Solar Wind Plasma and Magnetic Structures.

Structure	SB Only	HCS		Local CS		SIR Only	No Clear Association
		with SIR	*without*	*with SIR*	*without*		
Reoccurring *(1998 – 2009)*	3.1%	17.6%	11.5%	9.2%	8.4%	13.7%	36.6%
Reoccurring *(2010 & 2011)*	4.5%	27.3%		13.6%		54.5%	

Note: For reference, there are 131 events from 1998 to 2009 and 22 events in 2010 & 2011.

another dropout in the following Carrington rotation. This would imply that the total amount of plasma coming from such structures may be significantly higher than the 5.5% we reported in section 3.2.1. As a side note, we looked at the composition of reoccurring dropouts but found no discernable difference from non-reoccurring dropouts.

3.5 DISCUSSION

3.5.1 Coronal Source Structures

As we demonstrated in section 3.2.2, heavy ion dropouts have composition most similar to plasma found in closed coronal structures such as coronal streamers. We also found that dropouts comprise 5.5% of all solar wind. However, it is unreasonable to assume that all plasma coming from large, closed coronal loops exhibit the same mass-fractionated signatures of heavy ion dropouts. Therefore our observations represent an absolute lower bound for the total amount of solar wind originating in those structures and being released into the heliosphere. The actual quantity is probably much higher than 5.5%. Nevertheless, the observations of heavy ion dropouts, reoccurring ones in particular, may indicate something about the occurrence rate of exceptionally large and quiet coronal loops.

3.5.2 Release Mechanisms

Our evidence so far indicates that heavy ion dropouts originate from large coronal loops that are relatively long-lived and located predominately near the edges of low latitude coronal holes. The next question to consider then is *how* the plasmas were released from the loops to become part of the solar wind. Wang et al. (2000) describe three means by which closed field plasmas may escape into the heliosphere (see Figure 3.9):

a) Stretching of the loop large distances out into the heliosphere while the footpoints remain rooted in the corona. This is often observed during ICMEs however it requires enormous plasma pressures to trigger the event.
b) Pinching off of the loop tip (i.e. the so-called “LASCO blobs”)
c) Complex, 3D reconnection with adjacent open field lines whereby plasma leaks out of the loop while leaving it relatively intact.

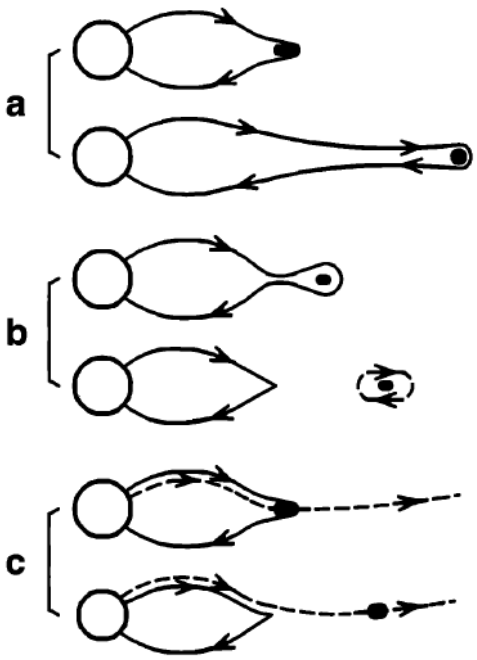

Figure 3.9: Illustration of the three main mechanisms by which closed field plasma may be released into the solar wind: (a) stretching of the loop large distances into the heliosphere, (b) pinching off of the loop tip, and (c) 3D reconnection. Adapted from Wang et al. (2000).

Given the reoccurrence rates observed, we conclude that (c) is most likely the primary release mechanism for heavy ion dropouts. While it is possible that some of our dropouts are in fact plasmoids or "LASCO blobs", the bursty nature of (b) makes the observation of reoccurring dropouts improbable over more than one or two Carrington rotations. Likewise, the extreme loop pressures required and careful filtering we did for ICMEs precludes significant contributions by mechanism (a). Furthermore, in the loop configuration caused by (a) we would expect to see counterstreaming suprathermal electrons which are not well correlated with the dropouts, although we do observe a few very short events in the data.

For the 3D reconnection case above, the height at which reconnection occurs may influence the elemental X/H ratios of a given dropout. Plasma escaping from lower down on the legs of a coronal loop would be expected to have smaller depletions of the heavy elements than plasma released from the top. However, smaller relative depletions could also be caused by the plasma being confined for a shorter time than required for gravitational settling. Additionally, the mechanism causing the FIP effect further complicates the picture. If the FIP effect is indeed caused by processes in the chromosphere as suggested by Laming (2004), then we would expect to see little to no difference in the FIP fractionation of the dropouts released from difference heights. If, on the other hand, the FIP effect occurs higher up the in the corona,

plasma from lower on a loop may be less or more FIP fractionated depending on the process invoked. Differentiating between spatial and temporal effects will require careful theoretical considerations coupled with the modeling of X/H ratios in a coronal loop. Such a comparison is outside the scope of our present work, although we will briefly address this topic in chapter 5.

3.6 SUMMARY AND CONCLUSIONS

In this chapter we have expanded upon our earlier work and presented more complete statistics of heavy ions dropouts spanning more than a solar cycle. We find that dropouts comprise at least 5.5% of all solar wind in the time period from February 1998 to August 2011. This is similar to the total amount of solar wind found in ICMEs for those years. Heavy ion dropouts exhibit X/O ratios similar to the slow solar wind however their X/H ratios are very different and most similar to those found spectroscopically in closed streamer belt loops. This result suggests dropouts must come from a subset of the same sources as the slow wind and illustrates the extra insight and fidelity of analyzing both the X/O and X/H ratios in tandem. We performed an extensive correlation with solar wind plasma and magnetic structures and found that most dropouts can be associated with the closed field region on either side of low latitude coronal holes. The observation of reoccurring dropouts allow for approximate source region latitudes to be calculated and open up a wealth of opportunities for direct comparisons of remote imaging of the solar surface and corona with in-situ plasma data. Further studies into potential release mechanisms and the exact mixing of coronal processes responsible for the dropouts may provide exciting new constraints for the development and refinement of solar wind origin theories.

CHAPTER IV

COMPARISONS WITH OBSERVATIONS MADE BY OTHER SPACECRAFT

All of our research up to this point has been based on data from the *ACE* / SWICS instrument. In this chapter we further expand our analysis with observations from other heliophysics missions – specifically the *Ulysses* and *SOHO* spacecraft. The purpose is twofold: (1) extend our dataset to include additional years, observational methods, and spacecraft vantage points and (2) test the conclusions and calculations we have made so far.

4.1 *ULYSSES* / SWICS OBSERVATIONS

4.1.1 Mission Overview

The *Ulysses* mission (Bame et al. 1992) was designed to study the properties of the heliosphere above the Sun's poles and collect the first set of solar wind observations from out of the ecliptic plane. A close fly-by of Jupiter was used to boost the spacecraft into a solar polar orbit with an inclination of 80.2^{o} relative to the Sun's equator. This type of maneuver is called a *gravity assist.* The final orbit was highly elliptical (ranging from 1.34 AU at perihelion to 5.4 AU at aphelion) and had an orbital period of 6.2 years. During the course of its ~19 year mission (6 Oct 1990 to 30 June 2009), *Ulysses* completed three polar orbits of the Sun. The time periods of perihelion were planned to coincide with solar minimum (first and third orbits) and solar maximum (second orbit). Figure 4.1 depicts the Jupiter fly-by and a portion of the first polar orbit. *Ulysses* carried a comprehensive instrument payload for the measurement of the solar wind, magnetic fields, and plasma waves. In particular, it carried a version of SWICS nearly identical to the one that later flew aboard *ACE*. In fact the *ACE* / SWICS instrument was a flight spare originally built for *Ulysses* (Gloeckler et al. 1998). The data processor and ground-based

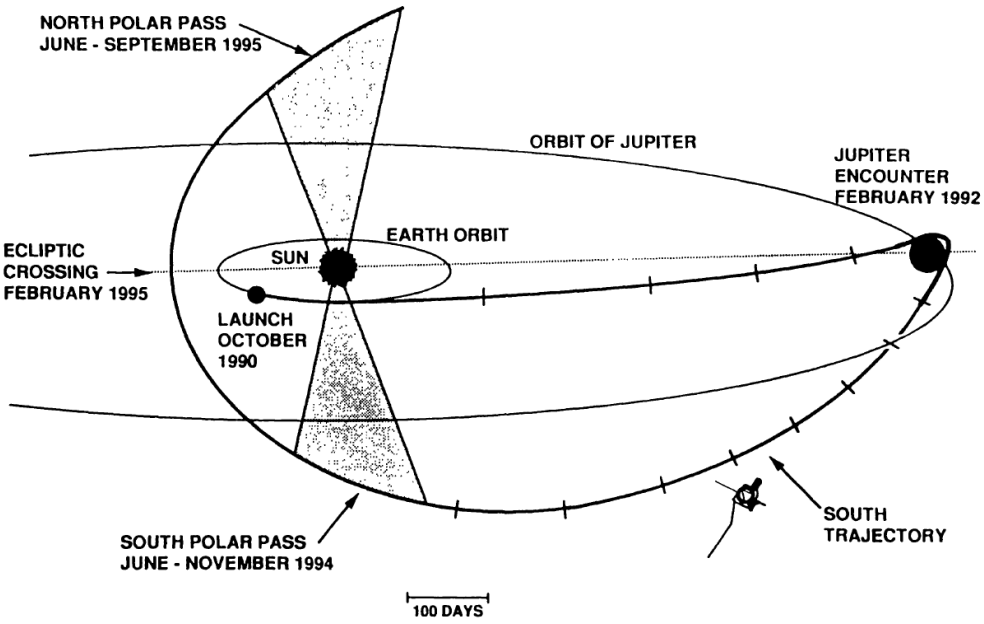

Figure 4.1: Diagram of the Ulysses trajectory from October 1990 to September 1995. The viewpoint is from 15^{o} above the ecliptic plane and tick marks are shown at 100-day intervals. For reference, Earth and Jupiter orbit at, respectively, average distances of 1 AU and 5.2 AU from the Sun. Adapted from Wenzel et al. (1992).

analysis methods were improved for the launch of *ACE* / SWICS; thus the publically available *Ulysses* / SWICS data reports fewer charge states at a longer time resolution than *ACE.* A reanalysis of the *Ulysses* / SWICS data is expected to be released in the coming months that will bring the two sets of data into closer alignment (von Steiger, personal communication). This new data, however, was unavailable at the time of our study.

4.1.2 Identification and Filtering of Heavy Ion Dropouts

In order to identify heavy ion dropouts at Ulysses, we used a combination of 3 hr heavy ion measurements from SWICS (Gloeckler et al. 1992) and 1 hr proton & alpha data from the Solar Wind Observations Over the Poles of the Sun instrument (SWOOPS; Bame et al. 1992). After rescaling SWOOPS to the same time resolution as SWICS, we then computed the He/H, C/H, O/H, and Fe/H ratios. Next we surveyed the Fe/H ratio to identify heavy ion dropouts using the same methodology as we did for *ACE* / SWICS data (as described in section 2.2.2) but with the minimum duration criteria set to 6 hrs rather than 4 hrs due to the lower temporal

resolution of *Ulysses* / SWICS. It is important to note that since we are using data from two different instruments it is possible that there may be some unknown scaling factor needed to properly cross-calibrate the data. Therefore the absolute X/H abundance ratios may be inaccurate by up to this same factor. Our dropout identification method, however, is still valid since it is based on the relative behavior of the data rather than the absolute values. Any scaling factor would shift the data values but leave the data trends intact.

Between the years of 1992 – 2007, we obtained an initial list of 286 possible dropout events which we then preceded to filter in the same way as before (see section 2.2.3 for more details). 8 events were discarded due to large (>33%) data gaps, 22 appeared to be false positives related to small scale spikes in hydrogen density events, and lastly 63 dropouts were set aside because they occurred during known ICMEs on a list published by Ebert et al. (2009).

After filtering, 193 heavy ion dropouts remained. We then analyzed the fractionation trends by comparing the relative dropout abundances to the nearby slow solar wind 5 days before and after the event. Our method was similar to the one we used for *ACE* dropouts (see sections 2.4.1 and 3.2.1), however we were unable to use the "jackknife" method when fitting the trends since we only had data for four elements, including He, which would have resulted in trivial, two-data-point fits with the Jackknife method (since He is omitted from fitting owing to its greater densities and additional dynamical processes). For clarity, it should be noted that in both the current analysis and that of section 3.2.1, we fitted trends to the $[X/H]_{dropout}$ / $[X/H]_{slow}$ relative ratio. This is the inverse of the relative ratio we initially used in section 2.4.1. The change, however, is superficial and does not ultimately affect our final conclusions. Instead it makes the resultant plots more intuitive to understand (smaller values indicate plasma that is more depleted). In this scheme, mass-fractionated dropouts are expected to have negative trends. We quantified mass fractionation as before by calculating the correlation coefficient, r, and using the standard significance levels from tables published by F. David (1938). For the case of 3 degrees of freedom (3 elements not counting He), the 95% significance level is denoted by $|r| \geq 0.8783$.

Of the 193 *Ulysses* dropouts, 63 (32.6%) exhibit strong mass-fractionation (negative trends with each heavier element more significantly fractionated), 79 (40.9%) have negative

trends with moderate to weak correlations (i.e. slightly mass-fractioned), 7 (3.6%) have positive correlations (1 with strong positive correlations, 6 with moderate to weak), and 44 (22.8%) have no clear trend. Figure 4.2 show the distribution of trend correlations categorized into confidence ranges of <50%, 50-80%, 80-90%, and ≥ 95%. Higher confidence levels suggest stronger correlations. For comparison, we have plotted the trend correlations for *ACE* dropouts in Figure 4.3. The Two spacecraft observed very similar trend distributions with roughly a third

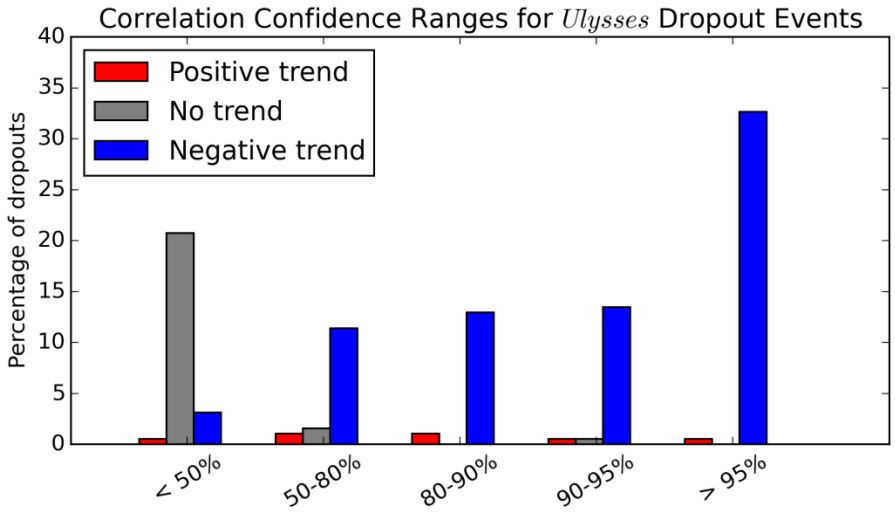

Figure 4.2: Correlation confidence ranges of all 193 *Ulysses* dropouts. Higher confidence ranges signify stronger correlations. The confidence level thresholds correspond to correlation coefficients, |r|, of 0.4040 (50%), 0.6870 (80%), 0.8054 (90%), and 0.8783 (95%). Only the negative trend dropouts in the > 95% range are classified as strongly mass fractionated in our analysis.

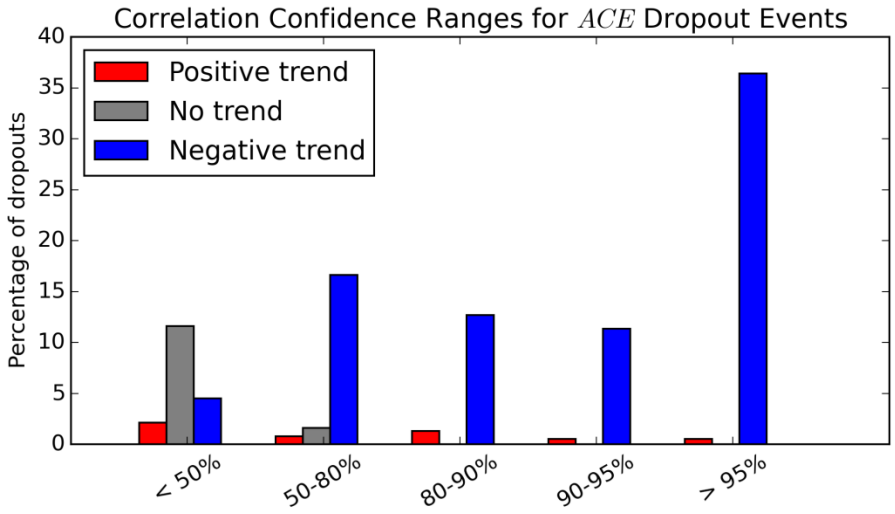

Figure 4.3: Correlation confidence ranges of all 379 *ACE* dropouts. Due to the fitting of more data points in *ACE* dropouts, the same confidence levels require lower values of |r| than in Figure 4.2.The thresholds are 0.3091 (50%), 0.5509 (80%), 0.6694 (90%), and 0.7545 (95%). Again, only the negative trend dropouts in the > 95% range are classified as strongly mass fractionated.

Table 4.1: Identification and Filtering of All Possible *Ulysses* and *ACE* dropouts.

Spacecraft	Possible Dropouts	High nH^+ (False events)	Data Gaps	Inside ICMEs	Total Dropouts	Mass-fractionated	No Clear Trend
Ulysses (1992-2007)	286	22	8	63	**193**	63 (32.6%)	44 (22.4%)
ACE (1998-2011)	473	23	21	50	**379**	138 (36.4%)	50 (13.2%)

of all dropouts exhibiting strong mass-fractionation. *Ulysses* has a larger fraction of dropouts with no clear trend. Table 4.1 compares the total number of possible *ACE* and *Ulysses* dropouts, event filtering, and relative number of mass fractionated events. Besides the greater number of events with clear trends, *Ulysses* dropouts are also proportionately more often observed inside ICMEs. Within the time period of our *ACE* observations, there are 304 ICMEs identified by Richardson & Cane (2010). Comparatively, Ebert et al. (2009) identified 178 ICMEs at *Ulysses* between the years of 1992 - 2007. Therefore a given ICME at Ulysses is 2.2 times more likely to contain a heavy ion dropout (35.4% of all ICMEs at *Ulysses* have an accompanying dropout versus 16.4% at *ACE*).

4.1.3 General Statistics and Elemental Composition

The annual number of Ulysses dropouts is plotted in Figure 4.4. The shaded regions of each bar signify the proportion of strongly mass-fractionated events in that year. Also shown are the smoothed sunspot number (red) and the heliographic latitude of *Ulysses* (blue). When compared to Figure 4.1, it would appear on the surface that *Ulysses* and *ACE* have opposite and contradictory annual trends over the solar cycle. For example, *Ulysses* observes considerably fewer dropouts at solar minimum while *ACE* observed slightly more. However this discrepancy can be at least partially explained by the difference in spacecraft orbits. At solar minimum *Ulysses* is near perihelion and performs what is called a "fast latitude scan" in which it quickly traverses from -79^o to $+79^o$ in a matter of months. During these scans *Ulysses* spends proportionately more time at high latitudes which are dominated by fast wind streams from the polar coronal holes. As we have established in the previous chapters, heavy ion dropouts are observed embedded in the *slow* solar wind, which at solar minimum is confined to a narrow $\sim 30^o$ band around the solar equator. Therefore the orbit of Ulysses is not conducive to

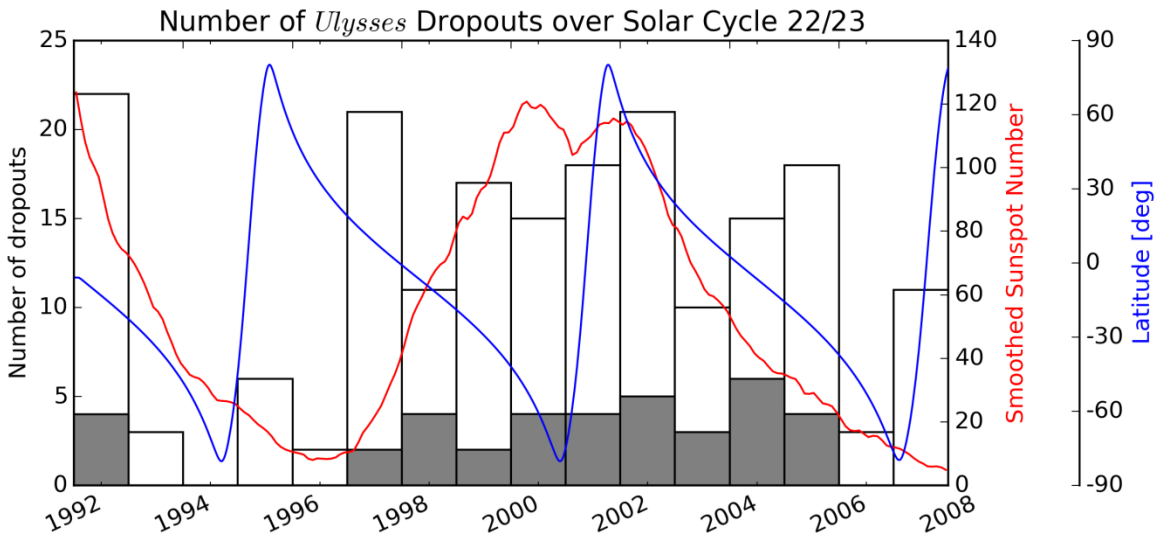

Figure 4.4: Annual number of heavy ion dropouts observed by *Ulysses* / SWICS over solar cycle 22/23 (1992, DOY 1 to 2007, DOY 365). The grey shaded regions indicate the portion of events that are strongly mass fractionated. Also shown is the smoothed sunspot number (red line) and heliographic latitude of *Ulysses* (blue line).

observations of heavy ion dropouts at solar minimum. If we consider just the five years around the solar maximum (1999 – 2003), we find that *Ulysses* observed 16.2 ± 2.6 dropouts per year which is actually lower than the number of dropouts observed by *ACE* for the same time period. Additionally, Ulysses observed a relatively high number of dropouts in 1997 when it was near the ecliptic plane after the first fast latitude scan. With these considerations in mind, we find Figure 4.3 to be in agreement with our previous analysis, including nearly steady number of mass-fractionated events each year. The median duration of *Ulysses* dropouts is 12.14 hours with a median absolute deviation (MAD) of 3.18 hours. This is similar to the median and MAD of 12.02 and 4.03 hours found at *ACE*. Lastly, we find that heavy ion dropouts comprise only 2.4% of all solar wind observed by *Ulysses*. This is still a sizable quantity given the aforementioned limitations of orbit and relative data quality. Furthermore, dropouts encompass 3.8% of all *slow* solar wind measured by *Ulysses*. This is on the same order of magnitude as ICMEs, which contain 7.9% of all *Ulysses* wind, but still lower than the 5.5% observed at *ACE*.

The elemental composition of Ulysses and ACE dropouts is explored in Figure 4.5, which shows the average X/H ratios for each element normalized by the appropriate photospheric ratio and arranged in order of increasing mass. Where available, we find that the average X/H

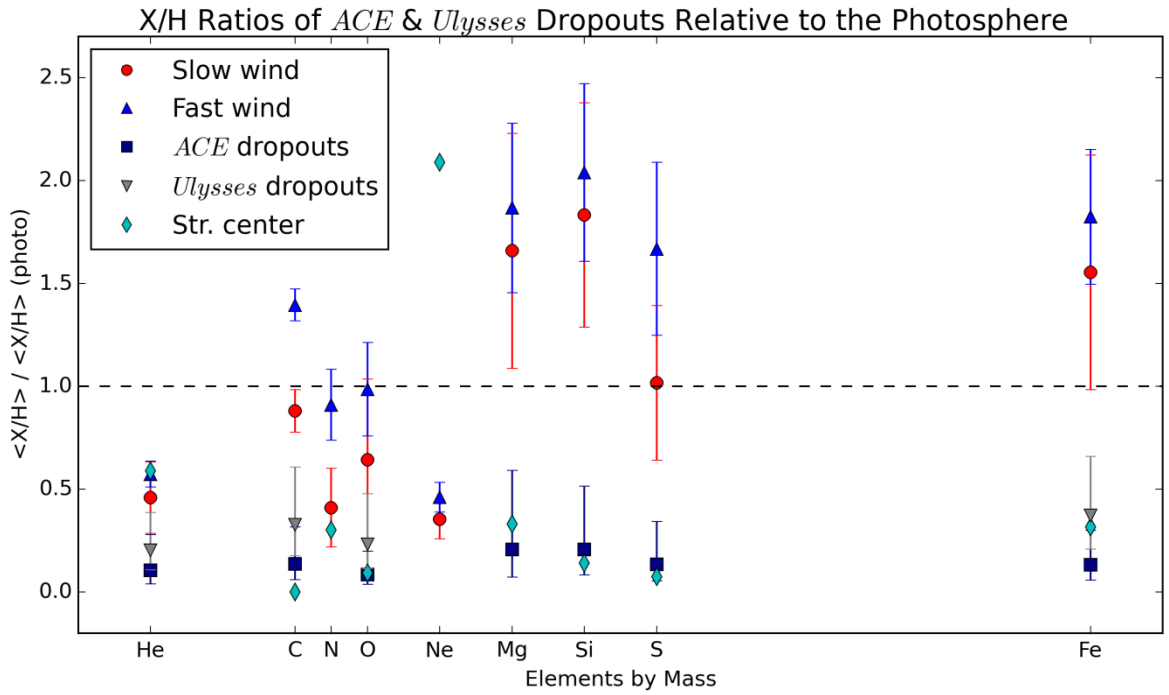

Figure 4.5: Elemental X/H ratios normalized by their photospheric values from Grevesse & Sauval (1998) and arranged in order of increasing mass. Where available, the average composition inside *Ulysses* dropouts (grey deltas) is similar to dropouts identified at *ACE* (navy squares).

ratios inside *Ulysses* (grey deltas) and *ACE* (navy squares) dropouts agree with one standard deviation of the values observed at either spacecraft. Furthermore, both are distinctly different from typical slow (red circles) and fast (blue triangles) solar wind as calculated from von Steiger et al. (2000) using the X/H ratio of von Steiger et al. (2010). As we found before, heavy ion dropouts have compositional signatures most similar to those observed spectroscopically inside a large, elementally depleted coronal streamer (Raymond et al. 1997). *Ulysses* dropouts tend to exhibit a larger range of values and are slightly less depleted in Fe than the events identified at *ACE*. Fe is depleted, on average, by a factor of 3.53 ± 2.15 at *Ulysses* with only 4 (2.1%) having depletions of over an order of magnitude (with a depletion of maximum of 12.24). Contrast this with ACE dropouts which have an average Fe depletion factor of 6.067 ± 4.816 and 48 (12.7%) with depletions greater than an order of magnitude (maximum of 44.77). The discrepancy in dropout magnitudes could be related to the aforementioned unknown calibration factor needed to determine the absolute X/H values with *Ulysses* / SWICS. It may also be indicative of additional expansion and mixing of dropout plasmas with nearby solar wind between 1 AU and

the location of Ulysses. In this latter scenario we would expect to see a dependence dropout magnitude or duration radial distance. However, despite our efforts to plot the base statistics in all possible combinations, we have yet to determine any kind of ordering of dropout duration or magnitude at either *Ulysses* or *ACE*.

4.1.4 Structure Correlations

Using 312 eV suprathermal electron pitch angle distributions from *Ulysses* / SWOOPS and magnetic field observations from the Vector Helium Magnetometer (VHM; Balogh et al. 1992), we next applied the methodology outlined in section 3.3.1 to identify solar wind magnetic structures at *Ulysses* and correlate them with heavy ion dropout. Unfortunately no list of SIRs has been published for *Ulysses*; therefore our dropout correlations are restricted to magnetic sector boundaries (SB), local current sheets (local CS), and heliospheric current sheet crossings (HCS). Table 4.2 gives the percentages of *Ulysses* dropouts correlated with solar wind magnetic structures. We also list the relative percentages of *ACE* dropouts reduced into the same subset of solar wind structures. We find almost no *Ulysses* dropouts correlated with HCS crossings (only 2 events total). However *Ulysses* dropouts are also more often correlated with isolated sector boundaries. It is possible that some of these SB events represent either incomplete HCS crossings (no flip in magnetic field direction observed) or crossings with rapidly varying magnetic field angle which thereby fails by our "moderately steady" identification criteria that requires the field angle varies less than 45^{o} for 12 hours before and after a reversal in direction. We also find that at a given satellite, mass fractionated dropouts do not have notably different structure correlations.

Table 4.2: Percentages of *Ulysses* and *ACE* Dropouts Correlated with Solar Wind Magnetic Structures.

Structure	SB Only	Local CS Only	HCS (SB with Local CS)	No Clear Association
All *Ulysses* Dropouts *(1992 – 2007)*	23.3%	2.1%	1.04%	73.6%
Ulysses Mass Frac. *(1992 – 2007)*	20.6%	3.2%	0.01%	76.2%
All *ACE* Dropouts *(1998 – 2011)*	3.7%	15.6%	26.9%	53.8%
ACE Mass Frac. *(1998 – 2011)*	5.1%	12.3%	23.9%	58.7%

4.1.5 Latitudes of Dropout Observations

The solar polar orbit of Ulysses makes it an ideal platform on which to test the approximate source region latitudes observations we calculated in section 3.4.2 using the reoccurring dropouts at *ACE*. By comparing the heliographic latitude of *Ulysses* dropout observations with the independently calculated latitudes from ACE, we can validate some of our base assumptions and determine if there is an observational bias towards certain latitudes. In the central panel of Figure 4.6 we have plotted the latitude of *Ulysses* (thin grey line) between the years of 1992 – 2007. Circle markers denote the times and latitudes heavy ion dropout observations. The top panel shows the bulk solar wind velocity from SWOOPS and the right panel is a histogram of the dropout latitudes. As can be seen, *Ulysses* observes dropouts at nearly all heliographic latitudes but only when also sampling slow type solar wind. No dropouts were observed embedded in fast wind from polar coronal holes. An example of this is clearly seen in the solar minimum pass of 1994/1995. Dropouts appear predominately within 45^{o} of

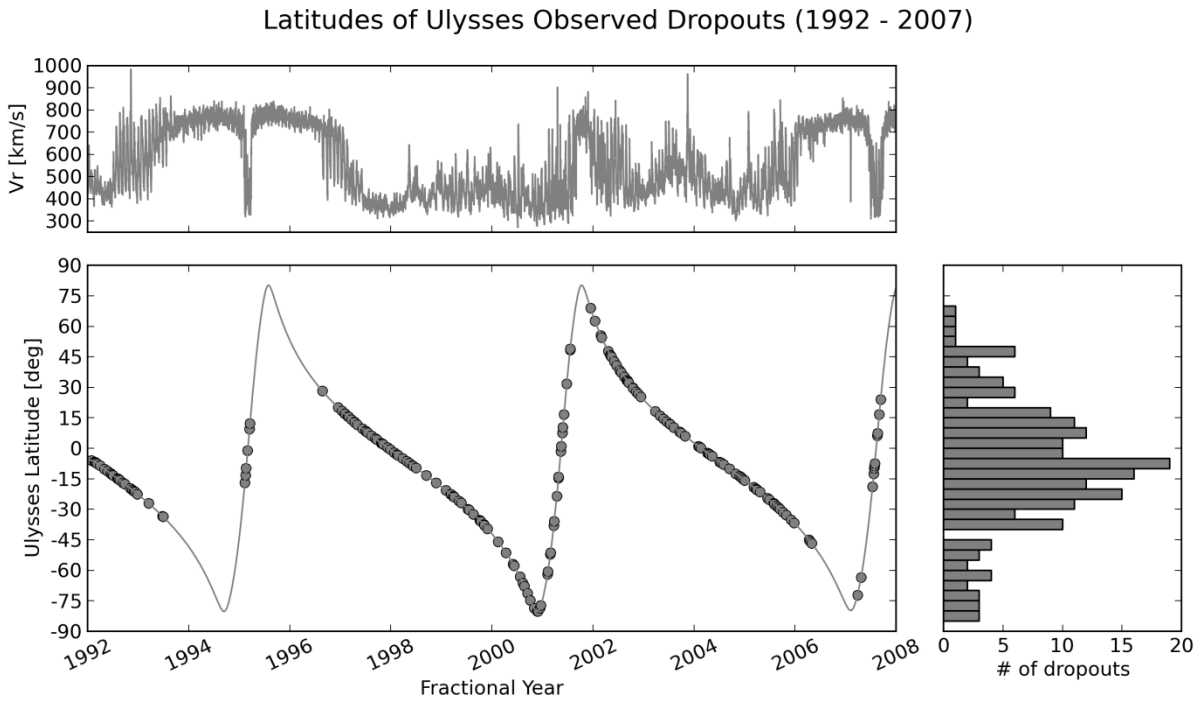

Figure 4.6: Heliographic latitude of *Ulysses* when it observed heavy ion dropouts (grey circles). The top panel shows the radial solar wind velocity from *Ulysses* / SWOOPS and the right panel is a histogram of the data along the Y-axis.

either side of the solar equator. This is in agreement with the band from 20^{o} – 40^{o} we calculated from *ACE* reoccurring dropouts and, furthermore, is at the same latitudes as most coronal streamers (Belik et al. 2004). When comparing Figure 4.6 to its counterpart from *ACE*, Figure 3.8, it is important to remember that the former is a simple plot of the heliographic latitude of *Ulysses* in space when- and wherever it observed dropouts while the latter figure shows the calculated latitudes of possible source regions *in the corona*. Despite being located in the ecliptic plane, *ACE* does not report any dropouts originating from the solar equator since none of the reoccurring dropouts resulted in a calculated source region with an equatorial angular velocity. Additionally, the calculations in section 3.4.2 did not differentiate between the northern or southern solar hemispheres. *Ulysses* does not observe any significant asymmetry between north and south dropout latitudes. Finally, we did not try to identify reoccurring dropout series at *Ulysses* since, unlike *ACE*, the spacecraft was not at a fixed location relative to the Sun, thereby reducing the likelihood of observing successive dropouts in a series.

4.2 *SOHO* / LASCO CORONAGRAPH IMAGES

4.2.1 Satellite and Instrument Overview

Another independent test of our latitude calculations can be made using remote observations. In this section we describe one possible comparison using data from the Solar and Heliospheric Observatory (*SOHO*; Domingo et al. 1995) which was launched in December of 1995 and currently orbits at the L1 point between Earth and the Sun. *SOHO* is outfitted with an array of instruments designed for the remote observation of the solar surface, interior (via helioseismological methods), and corona (with white light coronagraphs, UV & EUV spectrometers, and full-disk EUV imagers). *SOHO* also carried a modest suite of in-situ solar wind plasma instruments but lacked magnetic field measurements to accompany them; therefore the *SOHO* in-situ measurements were largely supplanted by the more complete set available form *ACE* upon its arrival at L1 in 1998.

In this study we used data from the Large Angle and Spectrometric Coronagraph (LASCO; Brueckner et al. 1995). LASCO is composed of three white light coronagraphs (C1, C2, and C3) with different sized internal occulting disks and fields of view. Together, they provide

partially overlapping images of the outer solar corona from 1.1 to 30 R_S. The radial distances observed by the three coronagraphs are 1.1 – 3 R_S (C1), 1.5 – 6 R_S (C2), and 3.7 – 30 R_S (C3). *SOHO* / LASCO data are available online at http://sohodata.nascom.nasa.gov/cgi-bin/data_query.

A faulty command during an orbital calibration maneuver in June of 1998, less than 5 months after *ACE*/SWICS began operations, resulted in the near catastrophic loss of *SOHO*. The spacecraft spun out of alignment with the Sun and all communications ceased. After six weeks of silence, communications were finally reestablished in August of 1998 and the spacecraft was slowly reoriented towards the Sun - restoring light to the solar panels and power to the instruments (Vandenbussche 1999). *SOHO* eventually resumed normal operations however the LASCO C1 telescope was irreparably damaged during the ordeal. Therefore our analysis will focus on images from the C2 telescope since it has the field-of-view reaching lowest into the inner corona during the time period of our *ACE* observations.

4.2.2 Comparison Method

For each reoccurring dropout observed at *ACE* we used a four step process. First we used the angular velocity of the postulated source region and the estimated time the dropout left the solar surface to determine when the source region would have been on the east limb of the Sun as viewed from LASCO. This east limb time, t_{EL}, can be estimated by the expression:

$$t_{EL} = t_2 - \frac{\pi}{2\omega} = t_2 - \frac{\pi}{2}\left(\frac{t_2 - t_1}{2\pi + \lambda}\right) \quad [4.1]$$

where t_1 and t_2 are the times two subsequent dropouts in a reoccurring series left the solar surface (calculated using equation 3.1) and $2\pi+\lambda$ is the total angle the Sun rotated between releasing the dropouts (the extra term of λ corrects for the orbital motion of Earth). It is important to note that this calculation does not define a time or latitude for the first dropout in a series. After estimating t_{EL}, we then queried the LASCO database and selected for comparison the C2 image closest in time. In most cases, the time difference between when the LASCO image was taken and t_{EL} was less than 30 minutes; however, due to LASCO data gaps, four events had time differences greater than 4 hours (up to a maximum allowed time difference of 12 hours). Next we overlaid the C2 image with a Sun-centered polar grid that extended out to

Table 4.2: Numerical Categories Used to Compare Approximate Dropout Latitudes with LASCO Images.

Value	Brightness of LASCO Feature	Location of Coincidence with *ACE* Dropout Latitude
5	Bright	Center of feature
4	Bright	Edge of feature
3	Dim	Center of feature
2	Dim	Edge of feature
1	Very faint	No clear boundary
0	None	None

the corona and plotted lines at the *ACE* calculated latitude both north and south of the solar equator.

Finally, we analyzed the output image by eye and classified it based on the coincidence of the calculated latitudes with features in the LASCO image. Specifically, we considered both the brightness of the feature, if any, and the location of coincidence with the calculated latitude to assign a numerical category from the list given in Table 4.2. The north and south possible latitudes were classified separately and the dropout event was assigned an overall category based on the highest value between the two. This process was then repeated for all reoccurring dropouts. Since qualitative metrics such as “bright” and “dim” are challenging to normalize and judge consistently across multiple images, we reduced our final statistics to the following set of categories: “center of feature” (highest value of 5 or 3), “edge of feature” (values of 4 or 2), “Ambiguous” (1s), and No structure (0s). Figure 4.7 is composite of plots from our analysis that exemplify these categories.

4.2.3 More Examples and Statistics

Of the 153 reoccurring dropouts, 76 had both a well-defined latitude and a LASCO C2 image available at the time when the source region was assumed to be on the east limb of the Sun. In these images, 20 (26.3%) of our calculated latitudes were well aligned with the centers of coronal streamers, 33 (43.4%) were found near streamer edges, 14 (18.4%) had ambiguous or unclear associations, and the remaining 9 (11.8%) had no discernable feature or coronal structure. All together we find that a majority (69.9%) of our calculated dropout latitudes correspond well to the latitudes of coronal streamers (either center or edge) as observed by the *SOHO* / LASCO C2 instrument. Given the uncertainties due to projection effects in the images

and the fact that our calculations are really only 1st order approximations, this correlation seems reasonably high and provides yet another link between solar wind heavy ion dropouts and large, closed coronal loops. Neither the location of coincidence (center vs edge) nor the dropout fractionation pattern (strongly mass-fractionated, flat trend, etc.) corresponded to any notable trends in latitude; all sub-sets of the data had the largest peaks between 20^{o} – 40^{o} as we observed in our *ACE* and *Ulysses* studies.

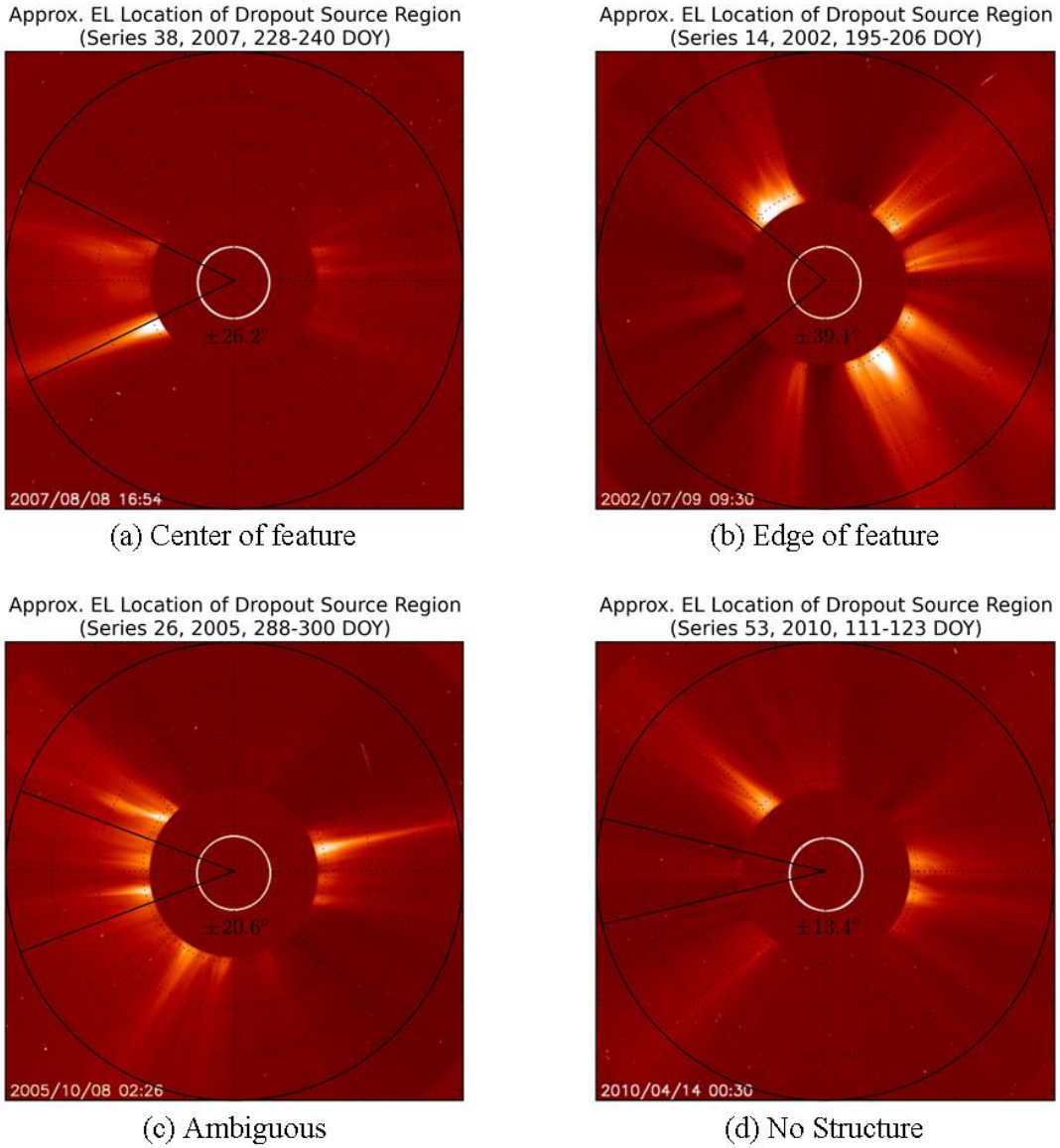

Figure 4.7: Example comparisons between ACE dropout latitudes and LASCO C2 images. Black lines indicate the latitude calculated using the method of section 3.4.2. The illustrated categories are (a) center of feature, (b) edge of feature, (c) ambiguous, and (d) no structure. See text for definitions and identification method.

4.3 SUMMARY OF RESULTS AND CONCLUSIONS

In this chapter we have tested and validated our *ACE* dropout observations through compassions to observations from the *Ulysses* and *SOHO* spacecraft. With the use of *Ulysses* / SWICS data, we extended our heavy ion dropout by an additional 6 years. We now have a combined list of 572 identified heavy ion dropouts spanning a time period of nearly 19 years (January 1992 – August 2011). Of these, ~35% exhibit strong, mass-dependent fractionation trends. Similar elemental composition and fractionation trends and are seen at both spacecraft. Ulysses also observed dropouts at nearly all heliographic latitudes but only embedded in slow solar wind streams. Ulysses dropouts were found predominately within 40^{o} of the solar equator which is the same range of latitudes observed for the majority of slow solar wind, particularly at solar minimum. These latitudes also agree well with the source region latitudes we calculated from reoccurring dropout series at *ACE.* Additional confirmation of our calculations came from comparisons with *SOHO* / LASCO coronagraph images.

CHAPTER V

MODELING GRAVITATIONAL SETTLING

In the previous chapters we described the identification of heavy ion dropouts, investigated their spatial and temporal variability, and demonstrated that dropouts originate from long lived structures in the solar corona. In this chapter we develop a theoretical model which provides a qualitative explanation of the main characteristic of dropouts: the strong mass-dependent elemental fractionation. The goal is *not* to build a detailed simulation capable of reproducing the large scale solar wind features as there are already a number of advanced codes designed specifically for this task, including the WSA-ENLIL model (Odstrcil 2003) which is used by the NOAA / Space Weather Prediction Center (SWPC; www.swpc.noaa.gov) and the Alfven Wave Solar Model (AWSoM; van der Holst et al. 2014) which is part of the Space Weather Modeling Framework (SWMF; Toth et al. 2005). Instead our objective is to perform a few illustrative calculations that can be directly compared with our heavy ion dropouts and may, in the future, serve as an interpretive aid for analyzing unusually fractionated solar wind.

5.1 CONCEPTUAL MODEL

5.1.1 Sketch of the Dropout Cycle

We begin by building a conceptual model of how mass-fractionated plasma is produced in the corona and then released into the heliosphere. Our base assumption is the occurrence of gravitational settling in large, quiet coronal loops. Gravitational settling is the simplest process which can produce mass-fractionation and has been observed remotely inside large, streamer belt loops (Raymond et al. 1997a; Feldman et al. 1998; 1999). The existence of reoccurring dropout series provides two key observational constraints we must take into account:

1. Dropouts originate from long-lived structures in the solar corona

2. The fractionation process must be repeatable and result in near continuous escape of plasma from the corona over time periods of at least 26 – 52 days (~1 – 2 Carrington rotations).

Therefore our modeled source region must consist of either (a) a singular loop which remains intact after reconnection and is constantly being refilled and/or growing in size until it reconnects again or (b) a series of adjacent loops with similar initial conditions and elemental composition. In the latter case, as soon as the outermost loop reconnects and releases its plasma, the next lower loop is free to expand until it reaches a height at which it too reconnects. These two scenarios, while mechanically different, would result in effectively the same rates and distribution of dropouts observed at Earth.

Figure 5.1 is a sketch of one dropout cycle including elemental fractionation, plasma release, and subsequent reset of the system. In the initial state (1), we model the structure of an elongated, streamer-like loop as consisting of cylindrical legs of length, *l*, topped by a half-torus with a major radius of *r*. The total height of the loop will then be, $z_{max} = l + r$. For simplicity we assume the cross-sectional area of the loop, *A*, remains constant with height. The total volume of the loop is given by:

$$V = 2Al + \pi Ar \quad [5.1]$$

The total mass within the loop can be obtained by summing the mass density of each element, ρ_s, and integrating over the entire volume:

$$M = \iiint \sum_s \rho_s dV = 2A \int_0^{z_{max}} \sum_s \rho_s dz \quad [5.2]$$

In the corona, the mass densities of the minor ions are very small compared to protons. As a consequence, we can obtain a good approximation of the total mass by omitting the sum and integrating only the proton density. (2) If given quiet conditions and enough time, gravity will separate the elements and cause vertical stratification proportional to mass, with the densities of heavier elements becoming more rarified with height than the densities of lighter elements. The gravitational settling time, t_{GS}, has been estimated to be on the order of a day to ~83 hours (Raymond et al. 1997b). We will try to calculate t_{GS} in section 5.3. (Figure 5.1: 3a) Interchange reconnection with adjacent open field line occurs at some rate, v_R, and will result in the loss of mass and magnetic flux from the loop. (3b) The mass-fractionated plasma previously trapped in

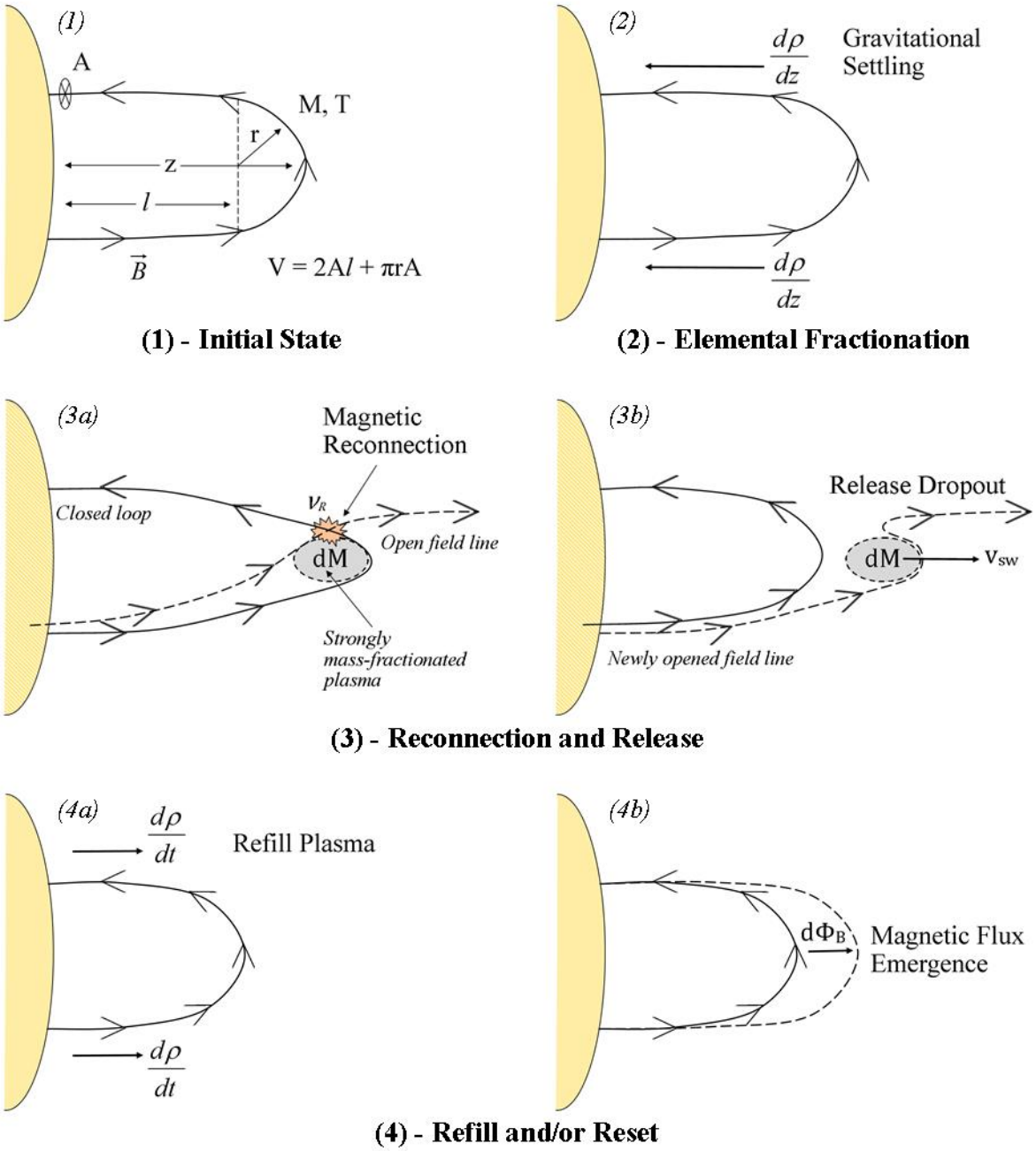

Figure 5.1: A conceptual sketch of one dropout cycle. An extended coronal loop in some initial state (1) is left relatively undisturbed by turbulence, mixing, or large scale plasma flows. (2) After some time, t_{GS}, the loop will become gravitationally settled. (3a & 3b) The loop then reconnects with an adjacent open field line and releases plasma from the top of the loop into the solar wind where it is later identified as a heavy ion dropout. Finally, the loop is reset to a similar state as (1) through upflows that refill the lost plasma (4a) and/or the emergence of magnetic flux (4b). The cycle then begins again at step (2).

the top on the loop is now free to flow out into the solar wind. Please note, we have illustrated in Figure 5.1 (3a & 3b) three-dimensional reconnection in which an adjacent open field line from outside the plane of the loop exchanges foot points with the loops leg containing oppositely directed magnetic fields. The pinching off of the top of the loop to form a closed-loop "plasmoid" is another possible release process (although from the structure correlations in chapter 3 we determined it cannot be the dominant form of plasma release). This alterative process is illustrated in Figure 5.2. After releasing the dropout, the loop is reset to a state similar to the beginning through upflows from the chromosphere that replenish the lost plasma (Figure 5.1: 4a) and/or the emergence of magnetic flux which replaces the volume lost by reconnection (4b). Plasma flows and flux emergence are likely concurrent processes. The dropout cycle then begins again at step (2). In the case of a stack of similar loops in the source region, no refill process is necessary and no part of the original loop needs to remain after reconnection. The next lower loop becomes the new boundary between open and closed fields and only needs to expand outwards until it reaches a similar maximum height as the first loop at which point it too reconnects and releases a dropout.

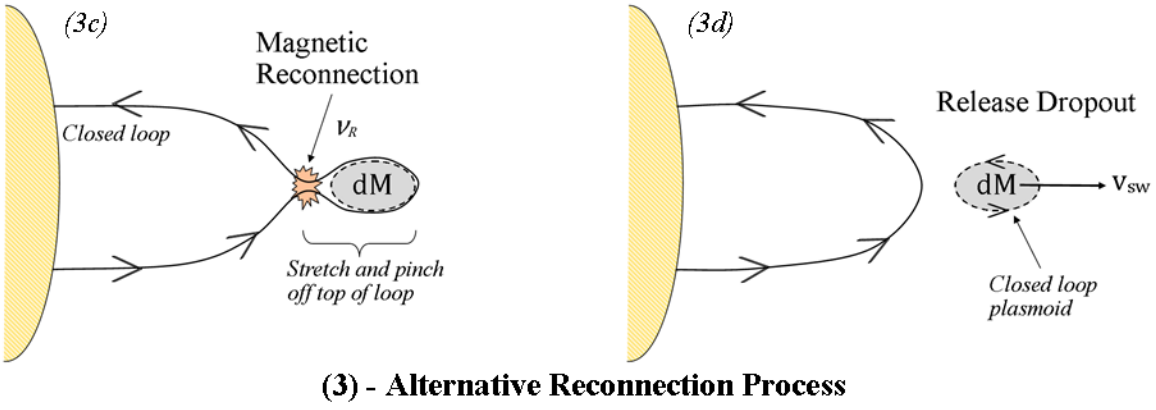

Figure 5.2: Alternative reconnection process. If the magnetic field line at the top of the loop is stretched out and then pinched together, the field line will reconnect with itself and release a closed loop plasmoid into the solar wind.

5.1.2 Time Scale Considerations

Assuming reoccurring events like those we have observed, we can make a few predictions based on the relative rates and time scales. Every time the loop reconnects, there will be a subsequent release of plasma and energy from the loop. In the case of reoccurring dropouts, the plasma must be given enough time to become mass-fractionated prior to release. Therefore the total time, t_c, of one cycle (fractionation, release, and reset) will ultimately be determined by the reconnection rate, v_R.

$$t_c = \frac{1}{v_R} \approx t_{GS} + t_{reset}$$

which gives,
$$t_{GS} = \frac{1}{v_R} - t_{reset} \quad [5.3]$$

We define t_{reset} as the additional time required for the loop to refill and expand back to the height at which it may reconnect again. The net change in mass within the loop can be expressed by,

$$\frac{dM_{loop}}{dt} = \frac{d\rho}{dt} dV - v_R dM_{dropout} \quad [5.4]$$

where *dM* and *dV* are the dropout mass and volume respectively. Assuming no net gain or loss of mass, this then yields,

$$\frac{1}{v_R} = \frac{dM_{dropout}/dV}{d\rho/dt} \quad [5.5]$$

If $\frac{1}{v_R} < t_{GS}$, additional dropouts in a series are expected to exhibit less mass fractionation than the first since the plasma will not have been given enough time to reach an equilibrium state. Likewise, if $\frac{1}{v_R} > t_{GS}$, then all dropouts in a series are expected to have similar fractionation. Another important consideration is the rate at which the loop refills. If the loop refills too quickly (i.e. $\frac{d\rho}{dt}$ is large), then mass fractionation will be erased. This is the same result as $\frac{1}{v_R} \ll t_{GS}$. Schawdron et al. (1999) predict that flow speeds in the range of 10 – 100 m/s would be sufficient to prevent mass-fractionation. If no upflows or refilling processes occur, the loop will begin the next cycle depleted in mass and already partially fractionated. Over time, the

loop would completely empty out, thereby setting a hard bound on the total number of dropouts it can release.

5.1.3 Constraints Derived from Observations

We now perform a few, back-of-the-envelope type calculations derived from dropout observations. First we estimate the total mass within each dropout by calculating the mass flux, Φ_m. Since the density of hydrogen in the solar wind is orders of magnitude larger than the other elements, we can approximate the total mass flux using the proton flux, Φ_p, which can be expressed by:

$$\Phi_p = n_p v_d \qquad [5.6]$$

where n_p is the number density of protons and v_d is the mean solar wind velocity inside the dropout. Figure 5.3 shows the distribution of proton fluxes observed within heavy ion dropouts. Vertical lines indicate the mean flux within dropouts (dashed black), slow (red), and fast (blue) solar wind. We find a mean proton flux of 2.22 x 10^8 n/(s $*$ cm^2) inside dropouts which is nearly identical to the slow solar wind value of 2.18 x 10^8 and very close to the fast wind value of 1.96 x 10^8. This translates to an average mass flux of $\Phi_m = \Phi_p \; x \; m_p =$ 3.71 x 10^{-19} kg/(s $*$ cm^2). If we assume dropouts can be approximated by a spherically symmetric parcel of plasma with a

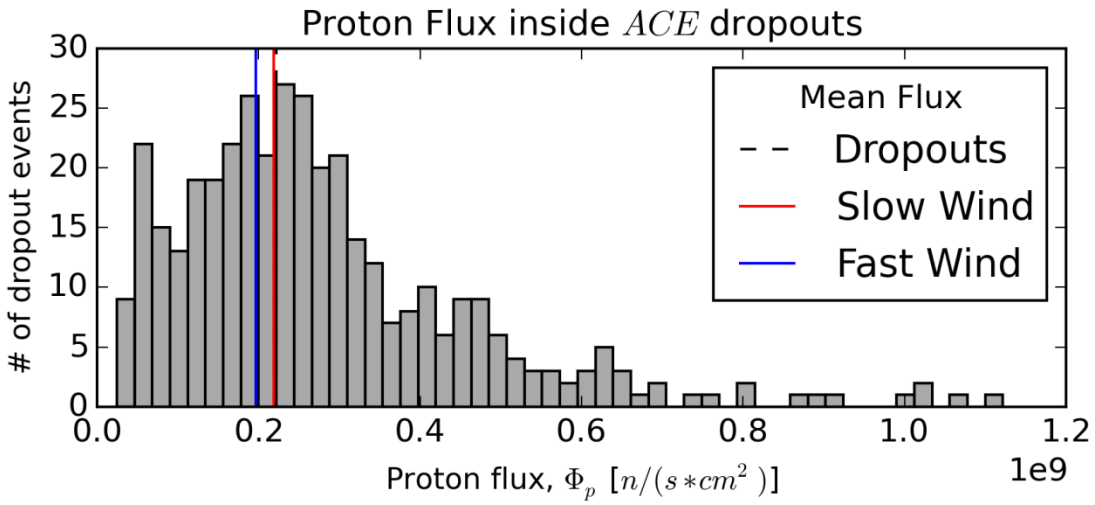

Figure 5.3: Distribution of proton flux observed inside *ACE* identified dropouts. Vertical lines indicate the mean flux within dropouts (black dashed), slow (solid red), and fast (solid blue) solar wind.

radius of r = (t_d x v_d) / 2, we can then describe the total mass of a given dropout by the expression:

$$dM = \rho_p V = m_p n_p \frac{4}{3}\pi r^3 = \Phi_m \frac{\pi}{6} {t_d}^3 {v_d}^2 \quad [5.7]$$

This equation yields and average dropout mass of 1.73 x 10^8 kg which is much smaller than the average CME mass of 1.6 x 10^{12} kg (Webb & Howard 2012).

Next we estimate the energy required to accelerate a dropout to the velocities observed in-situ. Assuming the dropout is stationary right before release for the loop (which is a fairly reasonable assumption for plasma sitting at the top of a quiet coronal streamer), the energy required is simply the total kinetic energy of the dropout in-situ which is given by the almost trivial equation,

$$KE = \frac{1}{2} dM {v_d}^2 \quad [5.8]$$

Using the equations we just derived in the previous paragraph, we determine an average energy of 1.18 x 10^{19} J is required to accelerate the dropouts. Some of this energy must come from the magnetic field during reconnection. If we knew the magnetic permeability of the solar corona, we could determine the corresponding amount of magnetic energy and field strengths available in the corona. Unfortunately such parameters cannot be directly measured as are unavailable without the aid of advanced modeling. It should be noted that the energy estimated here is orders of magnitude less than the 1.5 x $10^{23\text{-}26}$ J observed to be released during solar flares (Aschwanden et al. 2015).

Lastly we consider typical elemental composition. Table 5.1 lists the average X/H ratios observed inside heavy ion dropouts and the corona (from Feldman 1992). The last row gives the number of scale heights (distance over which an elements density decreases by a factor of 1/e) required for each element to become depleted from the coronal to the dropout value. The

Table 5.1: Average X/H ratios inside Heavy Ion Dropouts and the Corona.

	He/H	C/H	O/H	Mg/H	Fe/H
Coronal Value	7.94 x 10^{-2}	3.89 x 10^{-4}	7.76 x 10^{-4}	1.41 x 10^{-4}	1.26 x 10^{-4}
Average inside Dropouts	2.97 x 10^{-3}	3.2 x 10^{-5}	4.66 x 10^{-5}	1.02 x 10^{-5}	5.67 x 10^{-6}
Number of scale heights required	3.287	2.4931	2.8131	2.623	3.1007

elemental composition described in Table 5.1 constitute important boundary conditions and constraints on our efforts to simulate gravitational settling in the following sections.

5.2 MAGNETOHYDRODYNAMICS (MHD)

5.2.1 Ideal MHD Equations

The behavior of plasmas can be described by magnetohydrodynamic (MHD) theory which merges the mathematics of fluids and electrodynamics and treats plasmas as electrically conducting fluids. The basic MHD equations are a set of partial differential equations that can be used to completely describe the motion and time-evolution of a plasma. In space plasma physics we often use "ideal MHD" which assumes charge quasi-neutrality (no net charge), time-constant electric fields ($\partial \boldsymbol{E}/\partial t=0$), scalar pressure, and negligible heat flux. For a monatomic ion species s, with mass m_s, charge q_s, number density n_s, velocity $\boldsymbol{u}_s$, pressure P_s, and temperature T_s, the three fundamental MHD equations are as follows:

Continuity
$$m_s \frac{\partial n_s}{\partial t} + \nabla \cdot (m_s n_s \boldsymbol{u}_s) = 0 \quad [5.9]$$

Momentum
$$m_s n_s \frac{\partial \boldsymbol{u}_s}{\partial t} + m_s n_s (\boldsymbol{u}_s \cdot \nabla)\boldsymbol{u}_s + \nabla P_s - m_s n_s \boldsymbol{g} - q_s(\boldsymbol{E} + \boldsymbol{u}_s \times \boldsymbol{B}) = \sum_t m_s n_s \nu_{st}(\boldsymbol{u}_s - \boldsymbol{u}_t) \quad [5.10]$$

Energy
$$\frac{3}{2}\frac{\partial P_s}{\partial t} + \frac{3}{2}(\boldsymbol{u}_s \cdot \nabla)P_s + \frac{5}{2}P_s(\nabla \cdot \boldsymbol{u}_s) = \sum_t \frac{m_s n_s \nu_s}{m_s + m_t}[3k(T_t - T_s) + m_t(\boldsymbol{u}_t - \boldsymbol{u}_s)^2] \quad [5.11]$$

where $\boldsymbol{g}$ is the acceleration due to gravity, $\boldsymbol{E}$ is the external electric field, $\boldsymbol{B}$ is the external magnetic field, k is the Stefan-Boltzmann constant, and ν_{st} is the collision frequency between ion species s and t. From left to right, the terms of the momentum equation are: net acceleration, convection, pressure gradient, acceleration due to gravity, Lorentz force, and momentum exchange due to collisions (right hand side). Equations 5.9 – 5.11 govern, respectively, the conservation of mass, momentum, and energy in the plasma. Solving these equations for a multi-species plasma in a complete, self-consistent manner is not a trivial task. Many of the advanced MHD models (like the aforementioned ENLIL or AWSoM models) are the products of entire research groups and still mostly focus only H and He. In the sections that

follow, we make some simplifying assumptions that reduce the MHD equations to more tractable forms that suit our purposes.

5.2.2 Bounding Case: Simple Hydrostatic Equilibrium

We consider now the simple 1D case of a column of plasma with radial magnetic fields, no large scale flows, and changes only in the vertical direction, z. The continuity and energy equations are automatically satisfied and the momentum equation reduces to the time-independent form:

$$\frac{\partial P}{\partial z} = -m_s n_s g(z) \qquad [5.12]$$

where,
$$g(z) = \frac{GM_{Sun}}{z^2} \qquad [5.13]$$

Next we assume an isothermal coronal loop filled with a plasma that is satisfied by the ideal gas relation, *P=nkT*. Solving for the variation of n_s with height, we get the standard *hydrostatic equilibrium* solution:

$$n_s(z) = n_{s,o} exp\left[-\frac{GM_{Sun} m_s (z - z_o)}{kT_s (R_{Sun} + z)(R_{Sun} + z_o)}\right] \qquad [5.14]$$

Large coronal loops have typical maximum heights of 50 – 300 Mm and temperatures in the range of 1 – 3 MK. Coronal streamers, such as mass-fractionated ones observed by Raymond et al. (1997a) and Feldman et al. (1999) can have heights greater than 1.5 R_{Sun} above the solar surface (~1044.5 Mm). The streamers studied by Raymond et al. and Feldman et al. were both found to be well represented by isothermal temperature profiles of, respectively, 1.6 and 1.3 MK. Starting with average coronal X/H ratios derived from Feldman (1992), we calculate the abundance variations of He, C, O, Mg, and Fe in a loop with a maximum height of z_{max} = 50 Mm and temperature of 2 MK. The results are presented in Figure 5.4. The bottom of our simulation box was set at 2.1 Mm (approximately the top of the chromosphere and base of the corona). The dashed vertical lines indicate the average X/H ratios observed inside heavy ion dropouts. As can be seen in Figure 5.4, simple hydrostatic equilibrium predicts X/H ratios between 3 (for C & O) and 16 (Fe) orders of magnitude lower than those observed in-situ inside the dropouts. This result is not entirely surprising since hydrostatic equilibrium is a very simple

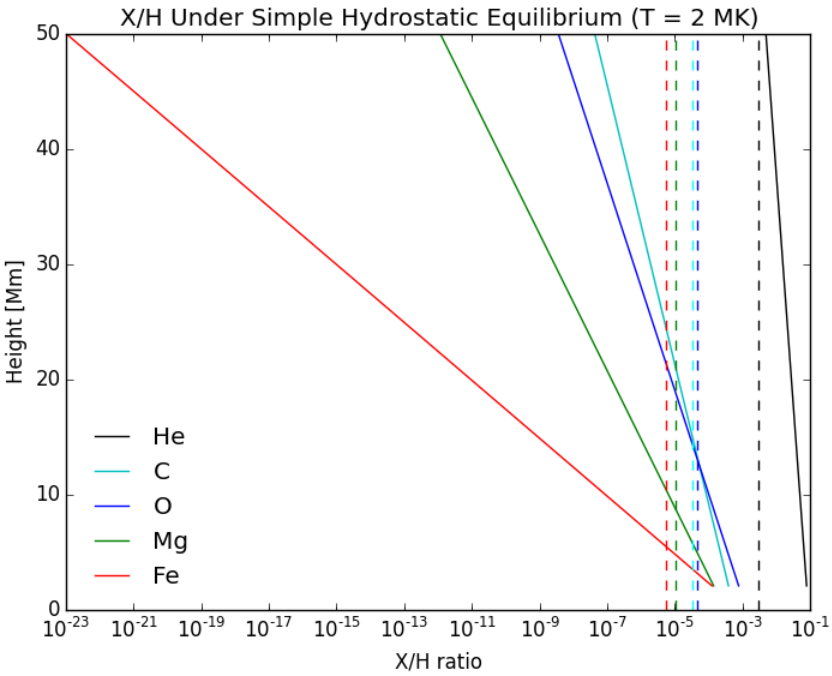

Figure 5.4: Simulated X/H ratios under simple hydrostatic equilibrium for a loop with a maximum height of 50 Mm and T = 2 MK. Vertical dashed lines indicate the X/H values observed inside heavy ion dropouts in the solar wind.

case that neglects terms from the momentum equation that may be significant in a more realistic loop. However, we have now established that, in the extreme case, it is possible to obtained coronal X/H ratios as low or lower than those we have observed. We are now tasked with adding terms and physics back into the MHD equations that may bring our calculations into agreement with our observations.

Along with an isothermal temperature profile, another assumption we made was that all ion species had the same temperature (i.e. $T_e = T_p = T_s$). This is a valid assumption for when the ions are in collisional thermodynamic equilibrium. If we allow the heavy ions to have different temperatures than the bulk plasma, their scale heights (and densities at the top of the column) will change accordingly. This can be thought of as a simple proxy for including an ion specific heating term. Ions with temperatures different than bulk plasma have been observed remotely. For example, Kohl et al. (1997) observed O^{5+} with T_O/T_H ratios of 10 to 100 within a polar coronal hole. In Figure 5.5 we show the T_X/T_H ratios required to reproduce the observed dropout X/H values under hydrostatic equilibrium for three different loop heights (150, 300, &

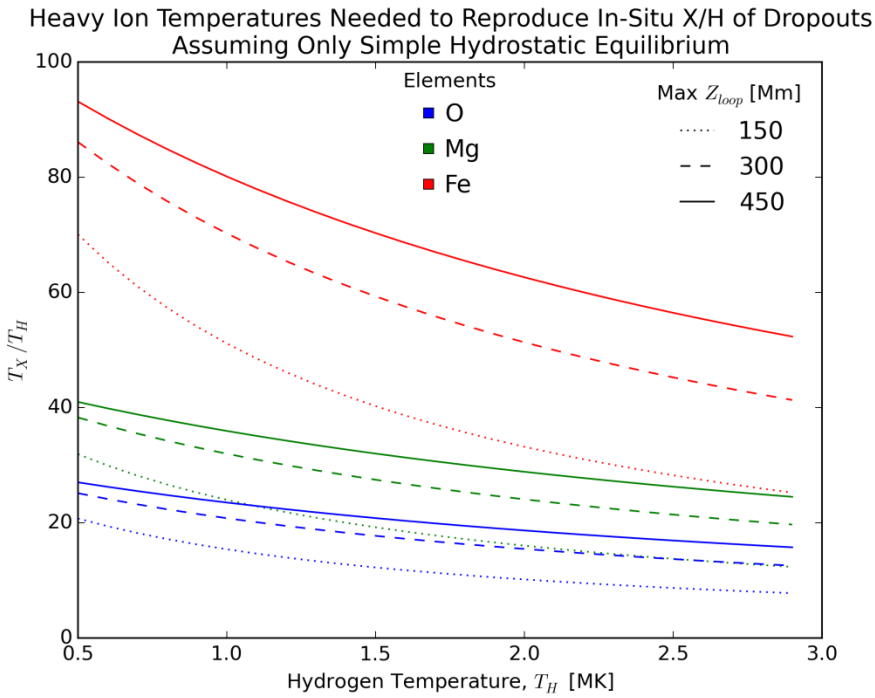

Figure 5.5: Heavy ion temperature ratios relative to hydrogen required to reproduce the observed X/H values inside heavy ion dropouts assuming hydrostatic equilibrium. Each line style corresponds to a different run with maximum loop heights of 150 (dotted line), 300 (dashed) and 450 (solid) Mm.

450 Mm) and hydrogen temperatures ranging from 0.5 to 3 MK. In each set of runs we fixed the X/H ratio at the top of the loop to match those observed inside dropouts and then calculated required temperature ratio. We find that for 1 MK < T_H < 3 MK we need T_X/T_H ratios of ~9 – 80. This is within the range observed by Kohl et al. and, for each ion considered, spans the mass propositional temperatures of 16, 24, & 56 T_H for, respectively, O, Mg, and Fe. While these results are interesting, it remains to be seen if such ion-dependent temperatures can exist within coronal streamers which may have strong collisional coupling that would tend to equilibrate the elemental temperatures. Within the solar wind dropouts, we observe average T_X/T_H ratios of 26 (for O), 36 (Mg), and 78 (Fe). In Figure 5.5, this set of values corresponds to a T_H of 0.7 – 1 MK at a height of 300 – 450 Mm. However, it is important to note that the in-situ temperature ratios may be elevated due to heating that occurs during the release and acceleration of the solar wind. For reference, T_O/T_H ratios of ~10-30 have been observed in the slow solar wind (Tracy et al. 2015).

5.3 TIME DEPENDENT HYDRODYNAMICS WITH COULOMB COLLISIONS

5.3.1 Derivation

Perhaps the most significant oversimplification in our hydrostatic equilibrium simulation was neglecting the effects of Coulomb collisions between heavy ions and the bulk plasma composed of protons. Collisions will retard the fall of heavy ions and help support them against gravity. Using a method similar to Raymond et al. (1997b) we now consider time *dependent* forms of the MHD equations and attempt to directly calculate the gravitational settling time, t_{GS}, required to obtain the observed dropout Fe/H. When we include Coulomb collisions and non-zero (but still constant) ion velocities, $\boldsymbol{u}_s$, within a stationary background plasma ($\boldsymbol{u}_H = 0$), the continuity and momentum equations become (again assuming radial magnetic fields):

Continuity
$$\frac{\partial n_s}{\partial t} + \frac{\partial}{\partial z}(n_s \boldsymbol{u}_s) = 0 \qquad [5.15]$$

Momentum
$$m_s n_s \boldsymbol{g} + \frac{\partial}{\partial z}(n_s k T_s) - \nu_{sp} m_s n_s \boldsymbol{u}_s = 0 \qquad [5.16]$$

where ν_{sp} is the Coulomb collision frequency between an individual ion species, *s*, and protons. Note, even though we allow for non-zero ion velocities, the Lorentz force term in the momentum equation still disappears since $\boldsymbol{u}_s$ is parallel to $\boldsymbol{B}$. Equations 5.15 and 5.16 are hydrodynamic equations that do not depend on the strength of the magnetic or electric fields as long as $\boldsymbol{u}_s \,||\, \boldsymbol{B}$.

For $\nu_{sp,}$ we use the equation used by Byhring et al. (2011) for their model of Fe abundances within coronal holes. This is given as:

$$\nu_{sp} = \frac{1}{3}\frac{n_p m_p}{m_s + m_p}\left(\frac{2\pi k T_{sp}}{\mu_{sp}}\right)^{-3/2}\frac{Z^2 e^2}{\epsilon_0^2 \mu_{sp}^2} ln\lambda \qquad [5.17]$$

where *Ze* is the charge state of the ion species, *e* is the elementary charge of an electron, ϵ_0 is the permittivity of free space, and *ln* λ is the Coulomb logarithm. T_{sp} is the reduced temperature given by,

$$T_{sp} = \frac{T_s m_p + T_p m_s}{m_s + m_p} \qquad [5.18]$$

Similarly μ_{sp} is the reduced mass,

$$\mu_{sp} = \frac{m_s m_p}{m_s + m_p} \quad [5.19]$$

For mixed ion-ion collisions, the 2013 NRL Plasma Formulary (Huba 2013) gives the Coulomb logarithm ($ln\,\lambda$) as having the following form:

$$ln\lambda_{ii'} = 23 - ln\left[\frac{ZZ'(\mu+\mu')}{\mu T_{i'} + \mu' T_i}\left(\frac{n_i Z^2}{T_i} + \frac{n_{i'} Z'^2}{T_{i'}}\right)^{1/2}\right] \quad [5.20]$$

where *i* and *i'* indicate the different ions, μ & μ' are the ion masses relative to protons (e.g. $\mu = m_i/m_p$), Z & Z' are the ion charge states, and the temperatures, T_i & $T_{i'}$, are given in units of eV. For Fe^{10+} (the most common charge state of Fe observed in the solar wind), the Coulomb collision frequency in on the order of ν_{sp} = 0.96 Hz in the lower corona. From equation 5.17 it is clear that higher charge states will have larger collisions frequencies. For example, Fe16+ (often observed inside ICMEs) has ν_{sp} = 2.4 Hz. We predict then that higher charge state ions will take longer to become gravitationally settled.

5.3.2 Solution and Results

As in the hydrostatic case, we assume an isothermal loop with $T = T_s = T_p$. Combining equations 5.15 and 5.16, we obtain a partial differential equation for the time evolution of ion density:

$$\frac{\partial n_s}{\partial t} = -\frac{\partial}{\partial z}\left\{\frac{1}{\nu_{sp} m_s}\left[m_s n_s g + \frac{\partial}{\partial z}(n_s k T)\right]\right\} \quad [5.21]$$

We now solve Equation 5.21 over time for Fe^{10+}. Our general solution method for an arbitrary column of plasma with maximum height, z_{max}, and temperature, *T,* is as follows:

1. Compute the background n_p profile using hydrostatic equilibrium
2. Initialize n_{Fe} by setting the n_{Fe}/n_p ratio at all heights to the base coronal value. This height independent n_{Fe}/n_p profile simulates a well-mixed initial state.
3. Run the simulation for time increments of *dt*. In each time step we calculate the Coulomb collision rate using equation 5.17, and then solve equation 5.21 numerically.

In Figure 5.6 we show our initial results for simulating a column of plasma with a base hydrogen density of $n_p = 10^9$ cm^{-3}, z_{max} = 500 Mm, *T* = 2 MK, grid spacing of *dz* = 1 km and time steps of *dt* = 6 minute. Each color corresponds to the Fe/H ratio at different heights within the column. The

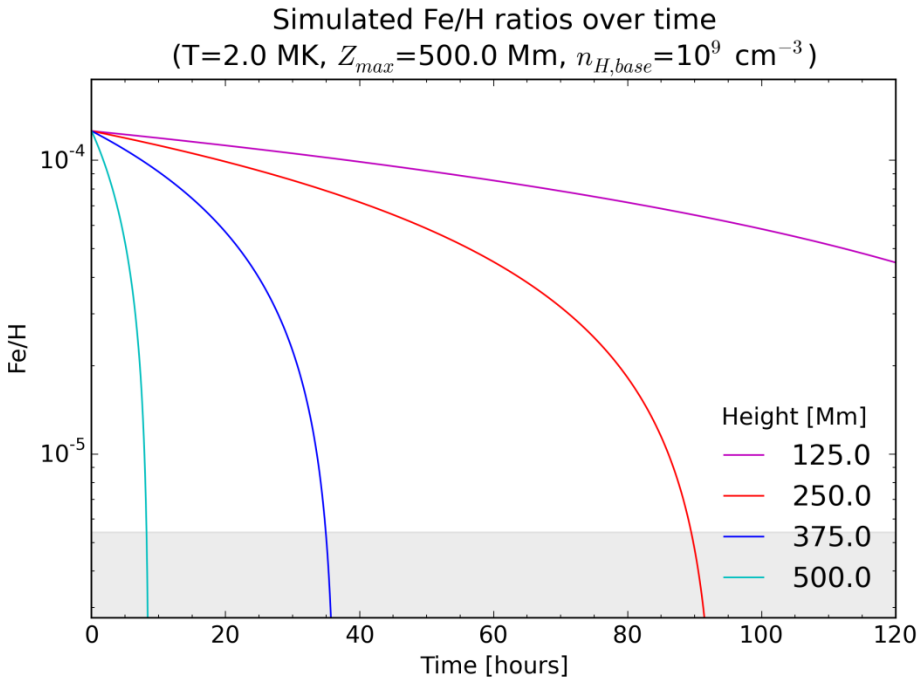

Figure 5.6: Simulated Fe/H ratios over time in a column of plasma with a temperature of 2 MK, maximum height of 500 Mm, and base proton density of 10^9 cm^{-3}. Each color corresponds to the Fe/H ratio a different height within the column. The grey shaded region indicates the average values of Fe/H observed within heavy ion dropouts.

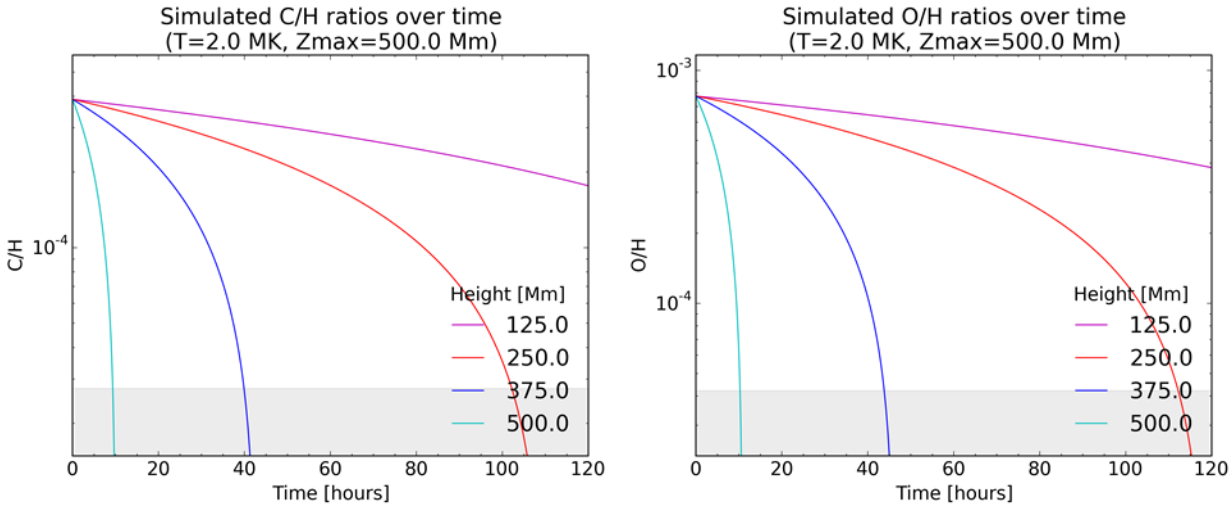

Figure 5.7: Simulated C/H (left) and O/H (right) ratios over time in a column of plasma with a temperature of 2 MK, maximum height of 500 Mm, and base proton density of 10^9 cm^{-3}. The times at which the simulated ratios are within the range of values observed inside heavy ion dropouts (grey shaded regions) agree favorably with the times indicated by Figure 5.5 for Fe/H.

grey shaded region indicates the average range of Fe/H observed within dropouts. We find that the higher sections of the column become depleted more rapidly; possibly owing to their lower initial Fe densities (requires less Fe loss to become strongly depleted in Fe/H). From our calculations the heights of 500, 375, & 250 Mm require settling times of ~10, 36, & 92 hours to become depleted to the same Fe/H values as seen inside heavy ion dropouts. These times agree well with the time scale ~83 hours estimated by Raymond et al. (1997b). In Figure 5.7 we show the results for C/H (left) and O/H (right) for the initial conditions as Figure 5.6. When calculating the Coulomb collision frequencies we assume the average solar wind charge states of C^{5+} and O^{6+}. The settling times required for C/H and O/H agree well with the times calculated for Fe/H. For heights of 500, 375, & 250 Mm we find times of ~10, 41, & 110 hours for C/H and ~10, 45, & 115 hours for O/H. The largest difference is at 250 Mm where there is a ~23 hour difference between the times calculated for Fe and O. Although since the times scales at that height are on the order of 100 hours, this translates to a difference of only 20 – 25%.

We now explore the sensitivity of our results to different initial conditions. On the left side of Figure 5.8 we show the results for Fe/H with $n_p = 10^{10}$ cm^{-3} at the base of the column. On the right side we show the results for T = 1 MK. In both the higher density and lower temperature runs, the plasma to takes longer to become gravitationally settled. This is what we would expect from the form of Equation 5.21. Higher proton densities will increase the

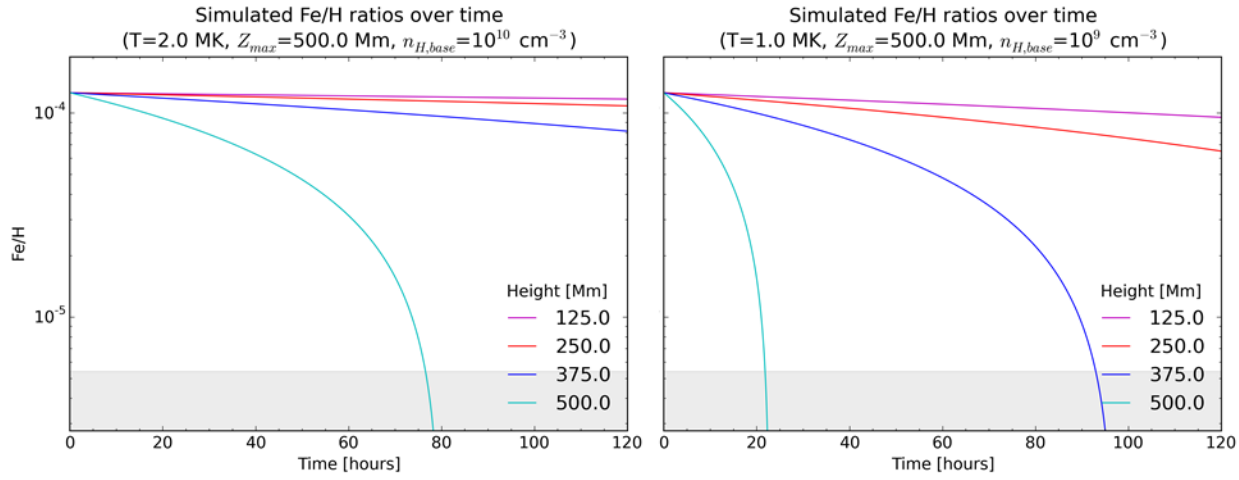

Figure 5.8: Simulated Fe/H over time with a higher base proton density of $n_p = 10^{10}$ cm^{-3} (left) or lower temperature of T = 1MK (right) when compared with Figure 5.5. Both cases predict longer settling times.

Coulomb collision frequency which, due it its location in the denominator, will decrease the rate plasma depletion. Similarly, the linear dependence on T in the second term on the right hand side means that a decrease in T will also result in smaller $\partial n_s/\partial t$.

As a final test, we calculate the gravitational settling times required when we allow the heavy ions to have higher temperatures than the background protons, as suggested by our earlier calculations in Figure 5.5. Our results for Fe/H are given in Figure 5.9 for a proton temperature of 1 MK and mass-proportional heating (T_{Fe}/T_p = 56). This temperature ratio is lower than that observed inside heavy ion dropouts however the in-situ value is likely elevated due to heating that occurs during solar wind acceleration and does not directly represent the source loop ratio. We find nearly identical settling times with differences of less than 2 hours when compared with the T_{Fe} = T_p case shown in Figure 5.6. Therefore we conclude that preferential heating of heavy ions may occur with the source regions of heavy ions dropouts but the additional heating is by no means required to explain the observed elemental abundances.

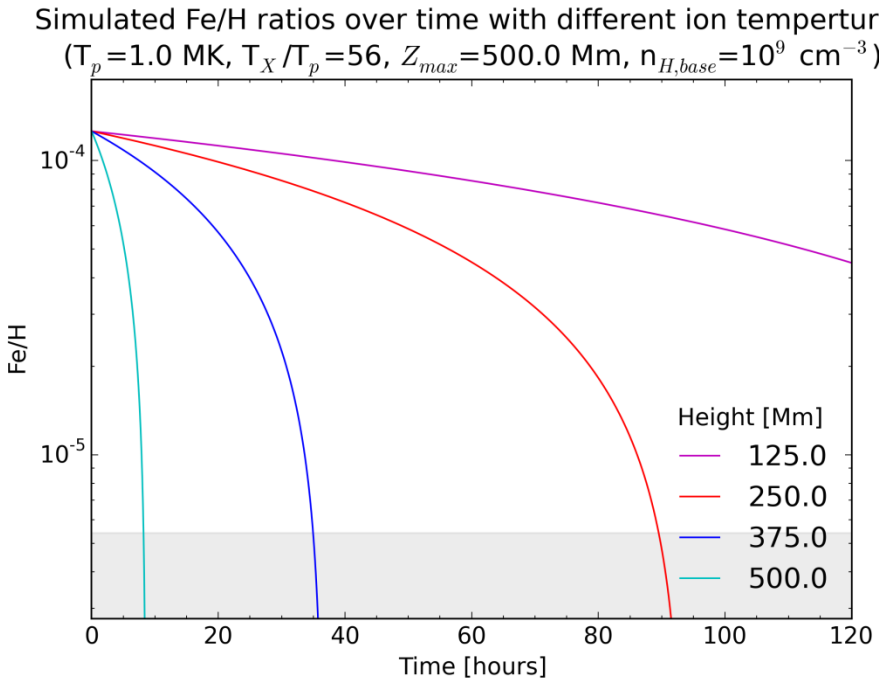

Figure 5.9: Simulated Fe/H ratios over time with mass-proportional heating. The parameters used in this run are T_p = 1 MK, T_{Fe}/T_p = 56, z_{max} = 500 Mm, and $n_{H,base}$ = 10^9 cm^{-3}. We find nearly identical settling times when compared with the T_{Fe} = T_p case shown in Figure 5.5.

5.4 CONCLUSIONS AND CONSTRAINTS ON SOLAR WIND THEORIES

In this chapter we have constructed a conceptual model of the heavy ion dropout cycle and performed a few calculations concerning the elemental abundances and gravitational settling times required to reproduce the X/H ratios observed inside heavy ion dropouts. In Section 5.2.2 we found that simple hydrostatic equilibrium in a moderately size coronal loop predicts X/H ratios at the top of the loop that are much lower than those observed in-situ. This suggests three scenarios: (a) plasma is escaping from low in the corona (below ~10 Mm) where the X/H ratios are higher, (b) the heavy ion temperatures are enhanced relative to hydrogen, indicative of ion specific heating, which would increase the elemental scale heights, or (c) there is some force or mixing process that significantly reduces how much mass-fractionation is able to occur.

A notable omission from our initial calculation was the effects of Coulomb collisions between heavy ions and the background plasma composed mostly of protons. When we include Coulomb collisions in a time-dependent calculation, we determined that a column of plasma will become gravitationally settled on a time scale of ~10 – 90 hours for heights greater than 250 Mm (shorter times are needed for higher heights). Below 250 Mm the time required for gravitational settling is greater than a week. In this case, a long-lived source region would only have time to release 3 – 4 heavy ion dropouts per solar rotation. This would make the probability of observing reoccurring dropout series very low. Therefore we conclude that scenario (a), which would necessitate plasma release from even lower in the corona, is unlikely even if the effects of collisions are minor.

We conclude that heavy ion dropouts must originate from above 250 Mm within a coronal loop. From our earlier investigations in Chapter III we determined that the existence of reoccurring dropouts and the correlations with solar wind magnetic structures strongly supported plasma release via interchange reconnection rather than loop top pinching. If this is the case, then the occurrence of interchange reconnection at large heights in the corona provides a new challenge to slow wind origin theories that must be explained. In the absence of large loop reset times (see Equation 5.3), the simulated settling times of 10 – 90 hours translates to a reconnection rate of 2.78×10^{-5} to 3.09×10^{-6} Hz (2.4 – 0.27 reconnection events

per day that result in the release of a dropout). This rate is slower that the ~4 reconnections per day inferred from remote observations of the so called "LASCO blobs" (Wang et al. 1998). Using the average dropout mass (1.73 x 10^8 kg) we derived in section 5.1.3, we calculate the total mass of dropouts released from a source region located between 20^o – 40^o latitude (angular velocity, ω = 14.7^o – 13.4^o per day) over the period of one solar rotation:

$$M = dM \frac{360}{\omega} \cdot \frac{\#\ dropouts}{day} = 1.14 \times 10^9 - 1.11 \times 10^{10}\ kg \qquad [5.22]$$

Assuming a constant loop cross-sectional diameter of 5.4 Mm (Klimchuk 2000), a simple summation over the 500 Mm tall loop simulations in section 5.3 yields a total mass of 8.7 x 10^9 kg (for a base n_p of 10^9 cm^{-3}). Therefore we conclude that a single, large coronal streamer contains only enough mass for one solar rotation's worth of heavy ion dropouts. The observation of reoccurring series persisting for more than a single CR requires either significant plasma refilling or a stack of similarly sized loops in close proximity. Given the fact that the former case would tend to mix the loop plasma and erase the compositional signatures of gravitational settling, we believe the latter scenario to the most sensible case.

CHAPTER VI

SUMMARY AND CONCLUSIONS

In this dissertation we attempted to answer the long-standing question of "what is the source of the slow solar wind" by comparing the elemental composition of heavy ions in the solar wind to remote observations of the corona. In particular, we discovered the existence of a new class of solar wind events called heavy ion dropouts which have distinctive mass-fractionation patterns similar to spectroscopic observations of large, coronal streamer loops. These dropouts provide unique insight into the physics of the solar corona.

6.1 REVISITING THE GUIDING SCIENCE QUESTIONS

We considered three guiding science questions that address the origin, release mechanisms and acceleration processes, and elemental fractionation of the solar wind. These questions are reiterated below with short summaries of the new perspective provided by our research.

6.1.1 How much plasma, if any, do the largest coronal loops contribute to the solar wind?

The mass-fractionated elemental abundances of heavy ion dropouts is best explained by gravitational settling which can only occur within extremely large and quiet coronal loops. Therefore the identification of dropouts in the solar wind provides strong evidence for solar wind escaping from such structures. Altogether heavy ion dropouts comprise 5% of all solar wind observed by *ACE* / SWICS in the ecliptic plane. This places a lower bound on the total amount of solar wind contributed by the largest coronal loops since not all plasma leaving the loops may have the fractionation patterns we used for identification of dropouts.

6.1.2 Where and how does closed field plasma escape into the solar wind and become accelerated?

Reoccurring dropouts indicate source regions that are rooted between 20^{o} – 40^{o} heliographic latitude. This is the same latitudes at which most coronal streamers are observed. Both comparisons with the latitudes of heavy ion dropouts identified at *Ulysses* and bright, coronal streamers seen in SOHO coronagraph images confirm our calculation using *ACE* data.

From our simulation in chapter V we concluded that heavy ion dropouts must be released from > 300 Mm above the solar surface. Below this height the plasma densities are too high and require settling times much longer than the release rates indicated by reoccurring dropouts. The temporal and spatial variability of dropouts is most consistent with interchange reconnection between open and closed magnetic field lines rather than a simple pinching off of the loop tip. Reconnection at such heights provides a challenge to theories that predict that all interchange reconnection occurs low in the corona near the foot points of loops. Additionally, if dropouts are released via interchange reconnection, then they are most likely also accelerated by direct energization during the reconnection processes rather than the wave-acceleration process predicted for the fast solar wind (although at this time we are not able to be entirely certain).

6.1.3 What are the physical conditions and time scales required for gravitational settling?

Through a combination of simulations and comparisons to the compositional signatures of heavy ion dropouts, we determined that gravitational settling requires ~10 - 90 hours in order to occur. During this time the coronal plasma must be left undisturbed by flows, mixing, or extra heating. Plasmas with a higher proton density or lower temperature require longer times to become settled. The heavy elements may be preferentially heated relative to hydrogen however the presence of such heating is not necessary for explain the observed elemental ratios. The simulated settling times of 10 – 90 hours translates to a rate of ~2.4 – 0.27 reconnections per day which is reasonable and consistent with other measurements.

6.2 RAMIFICATIONS FOR SLOW WIND THEORIES

The observations of heavy ion dropouts may be used to constrain the theories for the source of the slow solar wind that we described in section 1.4.3. From our results we conclude that gravitational settling cannot occur within open field regions as the plasma will not reside in the corona long enough to become mass-fractionated. Instead, we surmise that dropouts must originate in closed, coronal loops. Therefore the existence of heavy ion dropouts cannot be explained by the expansion factor model which predicts that all slow wind come from open field regions. This theory, however, cannot be completely dismissed as it may still explain the velocity ranges observed within different streams of *fast* solar wind.

In the streamer Top model, one of the components of the slow solar wind is thought to come from plasmoids released from the very top of coronal loops. This would result in plasma escape at the same heights as we inferred from our calculations. However, there are two aspects of heavy ion dropouts which are difficult to explain with the streamer top model. (1) In the heliosphere, plasmoids from coronal streamers are expected to be found very close to the HCS (within ~3^{o} according to Wang et al. 2000). However, less than 1/3 of all *ACE* dropouts are well associated with the HCS (see section 4.1.4). (2) The intermittent release of plasmoids from streamers would make the observation of reoccurring dropout series improbably for more than one or two solar rotations. While a majority (64.5%) of reoccurring dropout series exist for only 2 CR, the remaining 35.5% are observed over 3 to 5 CR (~82 – 136 days). Considering these two points we conclude that the streamer top model is a possible but not particularly probable source of heavy ion dropouts. Some dropouts may be embedded within slow wind plasmoids, they cannot be the dominant source.

The theories that best fit the observations are the interchange reconnection and S-web models. Each theory is constrained differently by our results. The key question for the interchange reconnection model is whether reconnection occurs high in the corona where the coronal loops are most significantly mass-fractionated. The challenge for the S-web model is determining if the closed loops adjacent to their open field corridors are tall enough for gravitationally settling to occur. Another test for both of the models is rate of reconnection and how it compares to the 2.4 – 0.27 events per day inferred from our dropout observations.

6.3 FUTURE WORK

Heavy ion dropouts are an exciting new class of solar wind events that are well poised to provide fresh and potentially key constraints on solar wind origin theories. We have presented here a number of conclusions concerning the elemental fractionation and release of the slow solar wind. However, in many ways, we are just beginning to explore the rich, new studies enabled by heavy ion dropouts. Future avenues of research include:

6.3.1 Investigation of dropouts found inside ICMEs.

Between ACE and Ulysses we have identified 113 dropouts embedded inside interplanetary coronal mass ejections. In this study we set the ICME events aside since we were most interested in the quiet, quasi-steady coronal conditions and ICMEs are, by nature, highly dynamic. The observation of dropouts inside ICMEs implies mass-fractionation within active region loops prior to CME initiation. It would be interesting to determine if there are any systematic differences imposed on heavy ion dropouts by the subsequent extra heating and explosive acceleration or weather there are any notable differences between ICMEs that contain dropouts and those that don't.

6.3.2 Direct comparison with concurrent spectroscopic observations.

The X/H ratios inside heavy ion dropouts compare favorably with the remote observations of an elementally depleted coronal streamer (Raymond et al. 1997). However this streamer preceded the earliest *ACE* dropout by almost 2 years. The identification of other spectroscopic observations concurrent with the time periods of heavy ion dropouts would allow for direct comparisons between coronal and solar wind plasmas. This would facilitate precise identification of dropout source regions and help quantify how much heating must occur during solar wind release and acceleration (by comparing and contrasting the velocities and charge states observed by the different methods).

6.3.3 Improved simulations.

In Chapter V we made a number of simplifications which allowed us to solve the fluid equations in a simple and relatively straightforward manner. In the future we hope to include the non-radial magnetic field geometries such as those found at the very tops of loops. Additionally, in our time-dependent calculations we assumed that all ions of a given element had the same charge state. This permitted us to quickly calculate the Coulomb collision frequency between the ions and the ground protons. In reality there is a distribution of charge states. Including multiple ion species of the same element should improve our determination of settling times and enable another set of comparisons between our observations and simulations. However, this extension is not a trivial task and will require the addition of ionization and recombination processes within the loop. At some point we may need to work with modelers to determine the feasibility of including heavy elements such as Fe in their advanced MHD models of the global corona. Such a simulation, if possible, would allow us to better examine the rates and locations of heavy ion dropouts in the future. Lastly, by connecting our measurements with simulations and models for the leading slow wind theories (such as the S-web model) we may be able to provide simple and well-defined observational tests.

REFERENCES

Antichos, S. K., DeVore, C. R., Karpen, J. T., & Mikic Z. (2007), Structure and Dynamics of the Sun's Open Magnetic Field, *The Astrophys. J.*, **671**, 936-946

Antiochos, S. K., Mikic, Z., Titov, V. S., Lionello, R., & Linker, J. A. (2011), A Model for the Sources of the Slow Solar Wind, *The Astrophys. J.,* **731**, 112-123

Aschwanden, M. J., Boerner, P., Ryan, D. et al. (2015), Global Energetics of Solar Flares. II., Thermal Energies, *The Astrophys. J.*, **802**, 53-72

Asplund, M., Grevesse, N., Sauval, A. J. & Scott, P. (2009), The Chemical Composition of the Sun, *Annu. Rev. Astron. Astrophys.,* **47**, 481-522

Bahcall, J. N., Pinsonneault, M. H., & Basu, S. (2001), Solar Models: Current Epoch and Time Dependences, Neutrinos, and Helioseismological Properties, *The Astrophys. J.,* **555**, 990-1012

Balogh, A., Beck, T. J., Forsyth, R. J., et al. (1992), The Magnetic Field Investigations on the Ulysses Mission: Instrumentation and Preliminary Scientific Results, *Astron. Astrophys. Suppl. Ser.,* **92**, 221-236

Bame, S. J., Goldstein, B. E., Gosling, J. T., et al. (1993), Ulysses Observations of the Recurrent High Speed Solar Wind Stream and the Heliomagnetic Streamer Belt, *Geophys. Res. Lett.*, **20**, 2323-2326

Bame, S. J., Hundhausen, A. J., Asbridge, J. R, & Strong, I. B. (1968), Solar Wind Ion Composition, *Phys. Rev. Lett.*, **20**, 393-395

Bame, S. J., McComas, D. J., Barraclough, B. L., et al. (1992), The Ulysses Solar Wind Plasma Experiment, *Astron. Astrophys. Suppl. Ser.,* **92**, 237-265

Belik, M., Markova, E., Rusin, V., & Minarovjech, M. (2004), Time-Latitudinal Development of the White Light Coronal Structures over a Solar Cycle, *Sol. Phys.,* **224**, 269-275

Biermann, L. (1951), Komentenschweife und solar Korpuskularstrahlung, *Zeitschrift für Astrophysik*, **29**, 274-286

Birkeland, K. R. (1905), Recherches sur les Taches du Soleil et Leur Origine, *Memorie della Societa Degli Spettroscopisti Italiani*, **34**, 14-18

Bodmer, R. & Bochsler, P. (2000), Influence of Coulomb Collisions on Isotropic and Elemental Fractionation in the Solar Wind Acceleration Process, *J. Geophys. Res.,* **105**, 47-60

Bonanno, A., Schlattl, H., Paterno, L. (2002), The Age of the Sun and the Relativistic Correction in the EOS, *Astron. & Astrophys.*, **390**, 1115-1118

Bonetti, A. Bridge, H. S., Lazarus, A. J., Rossi, B., Scherb, F. (1963), Explorer 10 Plasma Measurements, *J. Geophys. Res.*, **68**, 4017-4063

Boothroyd, A. I. & Sackmann I. (2003), Our Sun. IV. The Standard Model and Helioseismology: Consequences of Uncertainties in Input Physics and in Observed Solar Parameters, *The Astrophys. J.,* **583**, 1004-1023

Borrini, G., Gosling, J. T., Bame, S. J., Feldman, W. C., & Wilcox, J. M. (1981), Solar Wind Helium and Hydrogen Structure Near the Heliospheric Current Sheet: A Signal of Coronal Streamers at 1 AU, *J. Geophys. Res.*, **86**, 4565-4573

Bridge, H.S., Egidi, A., Lazarus, A. J., Lyon, E., & Jacobson, L. (1965), Preliminary Results of Plasma Measurements on IMP-A, *Space Research*, **5**, 969

Brueckner, G. E., Howard, R. A., Koomen, M. J. et al. (1995), The Large Angle Spectroscopic Coronagraph (LASCO), *Solar Phys.*, **162**, 357-402

Carlowicz, M. J. & Lopez, R. E. (2002), Storms from the Sun: The Emerging Science of Space Weather, (Washington, DC: Joseph Henry Press)

Carrington, R. C. (1859), Description of a Singular Appearance seen in the Sun on September 1, 1859, *Mon. Not. R. Astron. Soc.*, **20**, 13-15

Chapman, S. (1957), Notes on the Solar Corona and the Terrestrial Ionosphere, *Smithsonian Contrib. to Astrophys.*, **2**, 1-11

Charbonneau, P. (2014), Solar Dynamo Theory, *Annu. Rev. Astron. Astrophys.*¸ **52**, 251-290

Collins, G. W. (1989), The Fundamentals of Stellar Astrophysics, (W.H. Freeman and Company: New York, NY)

Crooker, N. U., Huang, C.-L., Lamassa, S. M., et al. (2004), Heliospheric Plasma Sheets, *J. Geophys. Res.*, **109**, A03107

David, F. N. (1938), Tables of the Correlation Coefficient, (London: Biometrika)

de Jong, T. & van Soldt, W. H. (1989), The Earliest Know Solar Eclipse Record Redated, *Nature*, **338**, 238-240

Dere, K. P., Landi, E., Mason, H. E., Monsignori Fossi, B. C., & Young, P. R. (1997), CHIANTI – An Atomic Database for Emission Lines, *Astron. Astrophys. Suppl. Ser.,* **125**, 149-173

Domingo, V., Fleck, B., & Poland, A. I. (1995), The SOHO Mission: An Overview, *Sol. Phys.,* **162**, 1-37

Downey, E. 2011, XEphem: Interactive Astronomical Ephemeris, *Astrophysics Source Code Library*, record ascl:1112.013

Ebert, R. W., McComas, D. J., Elliott, H. A., Forsyth, R. J., & Gosling, J. T. (2009), Bulk Properties of the Slow and Fast Solar Wind and Interplanetary Coronal Mass Ejections Measured by Ulysses: Three Polar Orbits of Observations, *J. Geophys. Res.,* **114**, A01109

Emilio, M., Kuhn, J. R., Bush, R. I., & Scholl, I. F. (2012), Measuring the Solar Radius from Space During the 2003 and 2006 Mercury Transits, *The Astrophys. J.,* **750**, 135-142Holzer, T. E., & Leer, E. (2004), Helmet Streamers Gone Unstable: Two-fluid Magnetohydrodynamic Models of the Solar Corona, *The Astrophys. J.,* **603**, 307-321

Feldman, U. (1992), Elemental Abundances in the Upper Solar Atmosphere, *Physica Scripta,* **46**, 202-220

Feldman, U. (1998), FIP Effect in the Solar Upper Atmosphere: Spectroscopic Results, *Space Sci. Rev.*¸ **85**, 227-240

Feldman, U., Doschek, G. A., Schuhle, U., & Wilhelm, K. (1999), Properties of Quiet-Sun Coronal Plasmas at Distances of 1.03 ≤ RS ≤ 1.50 Along the Solar Equatorial Plane, *The Astrophys. J.*, **518**, 500-507

Feldman, U., Mandelbaum, P., Seely, J. F., Doschek, G. A., & Gursky, H. (1992), The Potential for Plasma Diagnostics from Stellar Extreme-Ultraviolet Observations, *The Astrophys. J. Suppl. Ser.,* **81**, 387-408

Fisk, L. A. (2003), Acceleration of the Solar Wind as a Result of the Reconnection of Open Magnetic flux with Coronal Loops, *J. Geophys. Res.,* **108**, 1157-1164

Fisk, L. A. (2005), The Open Magnetic Flux of the Sun. I. Transport by Reconnections with Coronal Loops, *The Astrophys. J.,* **626**, 563-573

Fisk, L. A., Schwadron, A., & Zurbuchen, T. H. (1998), On the Slow Solar Wind, *Space Sci. Rev.*, **86**, 51-60

Geiss, J. (1982), Processes Affection Abundances in the Solar Wind, *Space Sci. Rev.*, **33**, 201-217

Geiss, J., Gloeckler, G., & von Steiger, R. (1995a), Origin of the Solar Wind from Composition Data, *Space Sci. Rev.*, **72**, 49-60

Geiss, J., Gloeckler, G., von Steiger, R. et al. (1995b), The Southern High-Speed Stream: Results from the SWICS Instrument on Ulysses, *Science*, **268**, 1033-1036

Gloeckler, G., Cain, J., Ipavich, F. M., et al. (1998), Investigation of the Composition of Solar and Interstellar Matter Using Solar Wind and Pickup Ion Measurements With SWICS and SWIMS on the ACE Spacecraft, *Space Sci. Rev.,* **86**, 497-539

Gloeckler, G., Geiss, J., Balsiger, H. et al. (1992), The Solar Wind Ion Composition Spectrometer, *Astron. Astrophys. Suppl. Ser.*, **92**, 267-289

Gombosi, T. I. (1998), Physics of the Space Environment, (Cambridge University Press)

Gonzalez, W. D., Joselyn, J. A., Kamide, Y., et al. (1994), What is a Geomagnetic Storm?, *j. Geophys. Res.*, **99**, 5771-5792

Gough, D. (1985), Inverting Helioseismic Data, *Sol. Phys.*, **100**, 65-99

Green, J. L., Boardsen, S., Odenwald, S., Humble, J, & Pazamickas, K. A. (2006), Eyewitness Reports of the Great Auroral Storm of 1859, *Adv. Space. Res.,* **38**, 145-154

Grevesse, N. & Sauval, A. J. (1998), Standard Solar Composition, *Space Sci. Rev.,* **85**, 161-174

Gringauz, K. I., Kurt, V. G., Moroz, V. I., Shklovskii, I. S. (1960), Results of Observations of Charged Particles Observed out to R = 100,000 km, with the aid of Charged-Particle Traps on Soviet Space Rockets, *Astronomicheskii Zhurnal*, **37**, 716-735

Hammer, R. (1982), Energy Balance of Stellar Coronae. I. Methods and Examples, *The Astrophys. J.*, **259**, 767-778

Hovestadt, D. (1974), in *Solar Wind Three* ed. C. T. Russell (Los Angeles: University of California)

Huba, J. D. (2013), NRL Plasma Formulary, (Naval Research Laboratory: Washington, D. C.)

Hundhausen, A. J. (1972), Coronal Expansion and Solar Wind, (Belin: Springer-Verlag)

Jian, L. K., Russell, C. T., & Luhmann, J. G. (2011), Comparing Solar Minimum 23/24 with Historical Solar Wind Records at 1 AU, *Sol. Phys.*, **274**, 321-344

Jian, L., Russell, C. T., Luhmann, J. G., & Skoug, R. M. (2006), Properties of Stream Interactions at One AU During 1995-2004, *Sol. Phys.,* **239**, 337-392

Klimchuk, J. A. (2000), Cross-Sectional Properties of Coronal Loops, *Sol. Phys.*, **193**, 53-75

Ko, Y-K., Fisk, L. A., Geiss, J., Gloeckler, G., & Guhathakurta, M. (1997), An Empirical Study of the Electron Temperature and Heavy Ion Velocities in the South Polar Coronal Hole, *Sol. Phys.*, **171**, 345-361

Kohl, J. L., Noci, G., Antonucci, E., et al. (1997), First Results from the SOHO Ultraviolet Coronagraph Spectrometer, *Sol. Phys.,* **175**, 613-644

Kopp, G. & Lean J. L. (2011), A New, Lower Values of Total Solar Irradiance: Evidence and Climate Significance, *Geophys. Res. Lett.*, **38**, L01706

Krieger, A. S., Timothy, A. F., & Roelof, E. C. (1973), A Coronal Hole and Its Identification as the Source of a High Velocity Solar Wind Stream, *Sol. Phys.,* **29**, 505-525

Laming, J. M. (2004), A Unified Picture of the First Ionization Potential and Inverse First Ionization Potential Effects, *The Astrophys. J.,* **614**, 1063-1072

Laming, J. M. (2012), Non-WKB Models of the First Ionization Potential Effect: the Role of Slow Mode Waves, *The Astophys. J.*, **744**, 115-128

Landi, E., Alexander, R. L., Gruesbeck, J. A., et al. (2012), Carbon Ionization Stateges as a Diagnostic of the Solar Wind, *The Astrophys. J.,* **744**, 100-110

Landi, E., Young, P. R., Dere, K. P., Del Zanna, G, & Mason, H. E. (2013), CHIANTI – An Atomic Database for Emission Lines. XIII. Soft X-ray Improvements and Other Changes, *The Asptrophys. J.*, **763**, 86-94

Lang, K. R. (2006), Sun, Earth and Sky, (New York: Springer Science)

Lemen, J. R., Sylwester, J., & Bentley, R. D. (1986), Dertermination of the Calcium Elemental Abundance for 43 Flares from SMM-XRP Solar X-Ray Spectra, *Adv. Space Res.,* **6**, 245-248

Luzum, B., Capitaine, N., Fienga, A. et al. (2011), The IAU 2009 System of Astronomical Constants: the Report of the IAU Working Group on Numerical Standards of Fundamental Astronomy, *Celest. Mech. Dyn. Astr.*, **110**, 293-304

Marocchi, D. Antonucci, E., & Giordano, S. (2001), Oxygen Abundance in Coronal Streamers During Solar Minimum, *Annales Geophysicae,* **19**, 135-145

McComas, D. J., Bame, S. J., Barker, P., et al. (1998), Solar Wind Electron Proton Alpha Monitor (SWEPAM) for the Advanced Composition Explorer, *Space Sci. Rev.*, **86**, 563-612

McComas, D. J., Ebert, R. W., Elliott, H. A., et al. (2008), Weaker Solar Wind from the Polar Coronal Holes and the Whole Sun, *Geophys. Res. Lett.,* **35**, L18103

McComas, D. J., Elliott, H. A., Schwadron, N. A., et al. (2003), The Three-Dimensional Solar Wind Around Solar Maximum, *Geophys. Res. Lett.,* **30**, 1517-1520

McIntosh, S. W., Leamon, R. J., Krista, L. D. et al. (2015), The Solar Magnetic Activity Band Interaction and Instabilities that Shape Quasi-Periodic Variability, *Nature Communications*, **6**, 6491

Meyer, J. P. (1981), A Tentative Ordering of All Available Solar Energetic Particles Abundance Observations: II- Discussion and Comparison with Coronal Abundances, *Proceedings of the 17th International Cosmic Ray Conference, held in Paris, France*, **3**, 149-152

Meyer, J. P. (1991), Diagnostic Methods for Coronal Abundances, *Adv. Space Res.,* **11**, (1)269-(1)280

Meyer-Vernet, N. (2007), Basics of the Solar Wind, (Cambridge University Press)

National Research Council (2009), Severe Space Weather Events--Understanding Societal and Economic Impacts: A Workshop Report - Extended Summary, (Washington, D.C.: National Academies Press)

Noci, G., Kohl, J. L., Antonucci, E., et al. (1997), The Quiescent Corona and Slow Solar Wind, *Proceedings of the Fifth SOHO Workshop, "The Corona and Solar Wind near Minimum Activity", Olso, Norway, 17-20 June 1997*, ESA SP – **404**, 75-84

Nolte, J. T., Krieger, A. S., Timothy, A. F., et al. (1976), Coronal Holes as Sources of Solar Wind, *Sol. Phys.,* **46**, 303-322

Odstrcil, D. (2003), Modeling #-D Solar Wind Structure, *Adv. Space Res.,* **33**, 497-506

Ofman, L. (2000), Source Regions of the Slow Solar Wind in Coronal Streamers, *Geophys. Res. Lett.,* **27**, 2885-2888

Oran, R., Landi, E., van der Holst, B., et al. (2015), A Steady-state Picture of Solar Wind Acceleration and Charge State Composition Derived from Global Wave-Driven MHD Model, *The Astrophys. J.,* Submitted, arXiv:1412.8288

Owocki, S. P., Holzer, T. E., & Hundhausen, A. J. (1983), The Solar Wind Ionization States as a Coronal Temperature Diagnostic, *The Astrophys. J.*, **275**, 354-366

Parker, E. N. (1958), Dynamics of the Interplanetary Gas and Magnetic Fields, *The Astrophys. J.*, **128**, 664-676

Parker, E. N. (1988), Nanoflares and the Solar X-Ray Corona, *The Asptrophys. J.,* **330**, 474-479

Pitjeva, E. V. & Standish, E. M. (2009), Proposals for the Masses of the Three Largest Asteroids, the Moon-Earth Mass Ratio and the Astronomical Unit, *Celest. Mech. Dyn. Astr.*, **103**, 365-372

Pneuman, G. W. (1976), Latitude Dependence of the Solar Wind Speed: Influence of the Coronal Magnetic Field Geometry, *J. Geophys. Res.,* **81**, 5049-5053

Pottasch, S. R. (1963), The Lower Solar Corona: Interpretation of the Ultraviolet Spectrum, *The Astrophys. J.,* **137**, 945-966

Priest, E. R., Foley, C. R., Heyvaerts, J., et al. (2000), A Method to Determine the Heating Mechanisms of the Solar Corona, *The Astrophys. J*., **539**, 1002-1022

Raymond, J. C., Kohl, J. L., Noci, G. et al. (1997a), Composition of Coronal Streamers from the SOHO Ultraviolet Coronagraph Spectrometer, *Sol. Phys.,* **175**, 645-665

Raymond, J., Suleiman, R., van Ballegooijen, A., & Kohl, J. (1997b), Absolute Abundances in Streamers from UVCS, *Proc. 31st ESLAB Symp., "Correlated Phenomena at the Sun, in the Heliosphere and in Geospace", Noordwijk, The Netherlands, 22-25 Sept. 1997,* ESA SP- **415**, 383-386

Richardson, I. G. & Cane, H. V. (2010), Near-Earth Interplanetary Coronal Mass Ejections During Solar Cycle 23 (1996-2009): Catalog and Summary of Properties, *Sol. Phys.*, **264**, 189-237

Scherrer, P. H., Bogart, R. S., Bush, R. I., et al. (1995), The Solar Oscillations Investigation – Michelson Doppler Imager, *Sol. Phys.*, **162**, 129-188

Schmelz, J. T., Reames, D. V., von Steiger,, R., & Basue, S. (2012), Composition of the Solar Corona, Solar Wind, and Solar Energetic Particles, *The Astrophys. J.,* **755**, 33-37

Schwadron, N. A., Fisk, L. A., & Zurbuchen, T. H. (1999), Elemental Fractionation in the Slow Solar Wind, *The Astrophys. J.,* **521**, 859-867

Sheeley, N. R., Wang, Y.-M., Hawley, S. H., et al. (1997), Measurements of Flow Speeds in the Corona Between 2 and 30 R_{Sun}, *The Asptrophys. J.,* **484**, 472-478

Smith, C. W., L'Heureux, J., Ness, N. F., et al. (1998), The ACE Magnetic Fields Experiment, *Space Sci. Rev.,* **86**, 613-632

Snodgrass, H. B. & Ulrich, R. K. (1990), Rotation of Doppler Features in the Solar Photosphere, *The Asptrophys. J.*, **351**, 309-316

Stahiv, M., Landi, E., Lepri, S. T., Oran, R., & Zurbuchen, T. H. (2015), On the Origin of Mid-Latitude Fast Wind: Challenging the Two-State Solar Wind Paradigm, *The Astrophys. J.,* **801**, 100-107

Sterling, A. C., Doschek, G. A., & Feldman, U. (1993), On the Absolute Abundance of Calcium in Solar Flares, *The Asptrophys. J.,* **404**, 394-402

Stone, E. C., Frandsen, A. M., Mewaldt, R. A., et al. (1998), The Advanced Composition Explorer, *Space Sci. Rev.*, **86**, 1-22

Strachan, L., Suleiman, R., Panasyuk, A. V., Biesecker, D. A., & Kohl, J. L. (2002), Empirical Densities, Kinetic Tempertures, and Outflow Velocities in the Equatorial Streamer Belt at Solar Minimum, *The Astrophys. J.,* **571**, 1008-1014

Suess, S. T., Ko, Y.-K., von Steiger, R., & Moore, R. L. (2009), Quiescent Current Sheets in the Solar Wind and Origins of Slow Wind, *J. Geophys. Res.*, **114**, A04103

Suess, S. T., Wang, A.-H., & Wu, S. T. (1996), Volumetric Heating in Coronal Streamers, *J. Geophys. Res.,* **101**, 19,957-19,966

Suess, S. T., Wang, A.-H., Wu, S. T., & Nerney, S. F. (1999), Streamer Evaporation, *Space Sci. Rev.,* **87**, 323-326

Sylwester, J., Lemen, J. R., Mewe, R. (1984), Variations in Observed Coronal Calcium Abundance of X-ray Flare Plasmas, *Nature,* **310**, 665-666

Szabo, A., Ogilvie, K. W., Viñas, A. F., & Summerlin, E. J. (2010), Solar Wind Kinetic Physics - High Time Resolution Solar Wind Measurements from the DSCOVR Mission, *White Paper for the National Academy of Science's 2013 Decadal Strategy for Solar and Space Physics*, http://www8.nationalacademies.org/SSBSurvey/DetailFileDisplay.aspx?id=750&parm_type=HDS

Tagger, M., Falgarone, E., & Shukurov, A. (1995), Ambipolar Filamentation of Turbulent Magnetic Fields, *Astron. Astrophys.*, **299**, 940-946

Toth, G., Sokolov, I. V., Gombosi, T. I., et al. (2005), Space Weather Modeling Framework: A New Tool for the Space Science Community, *J. Geophys. Res.*, **110**, A12226

Tracy, P., Zurbuchen, T. H., Kasper, J. C., et al. (2015), Thermalization of Heavy Ions in the Solar Wind by Coulomb Collisions, *in preparation for submission to The Astrophys. J.*

Uzzo, M., Ko, Y.-K., & Raymond, J. C. (2004), Active Region Streamer Diagnostics 2001 September 14-16, *The Astrophys. J.,* **603**, 760-775

Uzzo, M., Ko, Y.-K., Raymond, J. C., Wurz, P., Ipavich, F. M. (2003), Elemental Abundances for the 1996 Streamer Belt, *The Astrophys. J.,* **585**, 1062-1072

van der Holst, B., Sokolov, I. V., Meng, X., et al. (2014), Alfven Wave Solar Model (AWSoM): Coronal Heating, *The Astrophys. J.,* **782**, 81

Vandenbussche, F. C. (1999), SOHO's Recovery – An Unprecedented Success Story, *ESA Bulletin,* **97**, 39-47

Vauclair, S. & Meyer, J. P. (1985), Diffusion in the Chromosphere, and the Composition of the Solar Corona and Energetic Particles, *19th Intern. Comic Ray Conf.*, **4**, 233-236

Veck, N. J. & Parkinson, J. H. (1981), Solar Abundances of X-ray Flare Observations, *Mon. Not. R. Astron. Soc.*, **197**, 41-55

Vidotto, A. A., Gregory, S. G., Jardine, M, et al. (2014), Stellar Magnetism: Empirical Trends with Age and Rotation, *Mon. Not. R. Astron. Soc.,* **441**, 2361-2374

von Steiger, R. & Geiss, J. (1989), Supply of Fractionated Gases to the Corona, *Astron. Astrophys.*, **225**, 222-238

von Steiger, R. & Zurbuchen, T. H. (2011), Polar Coronal Holes During the Past Solar Cycle: Ulysses Observations, *Geophys. Res. Lett.,* **116**, A01105

von Steiger, R., Geiss, J., & Gloeckler, G. (1997), Composition of the Solar Wind, in *Cosmic Winds and the Heliosphere,* ed. J. R. Jokipii, C. P. Sonett, & M. S. Giampapa (Tucson, AZ: Univ. Ariz. Press), 581-616

von Steiger, R., Schwadron, N. A., Fisk, L. A., et al. (2000), Composition of Quasi-Stationary Solar Wind Flows from Ulysses/Solar Wind Ion Composition Spectrometer, *J. Geophys. Res.*, **105**, 27,217-27,238

von Steiger, R., Zurbuchen, T. H., & McComas, D. J. (2010), Oxygen Flux in the Solar Wind: Ulysses Observations, *Geophys. Res. Lett.,* **37**, L22101

Vsekhsvjatsky, S. K. 1963, *Proceeding of IAU Symposium no. 16* ed. J. T. Evans (New York: Academic Press)

Wang, Y.-M. & Sheeley, N. R. (1991), Why Fast Solar Wind Originates from Slowly Expanding Coronal Flux Tubes, *The Astrophys. J.,* **372**, L45-L48

Wang, Y.-M., Gappin, R., Robbrecht, E., & Sheeley, N. R. (2012), On the Nature of the Solar Wind from Coronal Pseudostreamers, *The Astrophys. J.*, **749**, 182-195

Wang, Y.-M., Sheeley, N. R., Socker, D. G., Howard, R. A., & Rich, N. B. (2000), The Dynamical Nature of Coronal Streamers, *J. Geophys. Res.*, **105**, 25,133-25,142

Wang, Y.-M., Sheeley, N. R., Walters, J. H., et al. (1998), Origin of Streamer Material in the Outer Corona, *The Astrophys. J.,* **498**, L165-L168

Webb, D. F. & Howard, T. A. (2012), Coronal Mass Ejections: Observations, *Living Rev. Solar Phys.,* **9**, 3

Weberg, M. J., Lepri, S. T., & Zurbuchen, T. H. (2015), Coronal Sources, Elemental Fractionation, and Release Mechanisms of Heavy Ion Dropouts in the Solar Wind, *The Astrophys. J.,* **801**, 99-107

Weberg, M. J., Zurbuchen, T. H., & Lepri, S. T. (2012), ACE/SWICS Observations of Heavy Ion Dropouts within the Solar Wind, *The Astrophys. J.*, **760**, 30-37

Wenzel, K.-P., Marsden, R. G., Page, D. E., & Smith, E. J. (1992), The Ulysses Mission, *Astron. Astrophys. Suppl. Ser.,* **92**, 207-219

Wimmer-Schweingruber, R. F., von Steiger, R., & Paerli, R. (1999), Solar Wind Stream Interfaces in Corotating Interaction Regions: New SWICS/Ulysses Results, *J. Geophys. Res.*, **104**, 9933-9945

Zhao, L., Zurbuchen, T. H., & Fisk, L. A. (2009), Global Distribution of the Solar Wind During Solar Cycle 23: ACE Observations, *Geophys. Res. Lett.,* **36**, L14104

Zurbuchen, T. H. & Richardson, I. G. (2006), In-Situ Solar Wind and Magnetic Field Signatures of Interplanetary Coronal Mass Ejections, *Space Sci. Rev.*, **123**, 31-43

Zurbuchen, T. H., Fisk, L. A., Gloeckler, G., & von Steiger, R. (2002), The Solar Wind Composition throughout the Solar Cycle, *Geophys. Res. Lett.,* **29**, 1352-1355

Zurbuchen, T. H., Hefti, S., Fisk, L. A., Gloeckler, G., & Schwadron, N. A. (2000), Magnetic Structure of the Slow Solar Wind: Constraints from Compositional Data, *J. Geophys. Res.,* **105**, 18,327-18,336

Zurbuchen, T. H., Hefti, S., Fisk, L. A., Gloeckler, G., & von Steiger, R. (1999), The Transition Between Fast and Slow Solar Wind from Composition Data, *Space Sci. Rev.,* **87**, 353-356